Agricultural Remote Sensing by Multiple Sensors Mounted on an Unmanned Aerial Vehicle

(無人飛行機に搭載した複数センサによる農業リモートセンシング)

BY

杜　蒙蒙

DISSERTATION

Submitted to Division of Environmental Resources in
Graduate school of Agriculture, Hokkaido University, Sapporo, Japan,
in partial fulfillment of the requirements for the degree of

Doctor of Philosophy

March 2018

Table of Contents

Acknowledgement

Firstly, I would like to express my sincere gratitude to my supervisor Prof. Noboru Noguchi with Research Faculty of Agriculture, Hokkaido Univ. for his valuable instruction and advices during my study on agricultural remote sensing in Robotics and Vehicle Laboratory. Civilian applications of unmanned aerial vehicle in recent year gained increasing interests all over the world, and based on Prof. Noguchi's insightful vision we opened a new way of acquiring field information in a simple and autonomous fashion by using an unmanned aerial vehicle as a platform. Using Prof. Noguchi's knowledge in the domain of precision agriculture for reference, we developed and studied on agricultural remote sensing by integration of multiple sensors on board low-altitude unmanned aerial system. However, the most difficult thing is to get started: we encountered tremendous hardships and obstacles to operate the drone at first. It is the understanding, encouragement, and guidance from Prof. Noguchi that pulled me through frustration and struggles in the first year of my study. I also benefitted enormously from the discussion with Prof. Noguchi when we designed brand new experiments using our hexa-copter, and the skills I learned from Prof. Noguchi will accompany me throughout my lifetime.

I would also like to thank Prof. Kazunobu Ishii and Prof. Hiroshi Okamoto with Research Faculty of Agriculture, Hokkaido Univ., for their assistance in conducting the experiments. Without their help it would be impossible for me to acquire enough data and to finish my dissertation. Days of experiments in Mackey of Australia, Memuro and Iwamiza of Japan have witnessed our sweats and laughter, which will never fade in my memory. Prof. Ishii appears to be informed, experienced, and sophisticated all the time. Anything went wrong during experiments with electronic hardware, telemetry signal, and network configuration and accessing, Prof. Ishii fixed it in no time. Prof. Okamoto's preciseness and strictness during the preparation of experiments before each field travel impressed me a lot, and I will live by his example in my upcoming careers.

My appreciation also goes to Ms. Aoki and Ms. Namikawa, secretaries of Vehicle and Robotics Laboratory, for taking good care of my research life over these three years so that I could concentrate on my study without worrying about procedural regulations and official businesses. I also would like to take this opportunity to thank Mr. Hiroyuki Sato and Mr. Shinji Ichikawa with Field Science Center for Northern Biosphere, Experiment Farm, Hokkaido Univ., as well as Mr. Tomonori Wada with Research Faculty of Agriculture,

Hokkaido Univ., for shuttling between campus and farmlands with me. My UAV team members, Miss Noriko Kobayashi, and Mr. Erdenebat Batzorig, together with other members of Vehicle Robotics Lab., contributed a lot to collect field data, and I highly appreciate their cooperation.

My Ph.D. study was supported by a joint scholarship program of CSC (China Scholarship Council) and MEXT (Ministry of Education, Culture, Sports, Science and Technology), Japan. I am forever grateful to CSC and MEXT for granting me this opportunity of studying in Japan. Our experiments were funded by the R&D program of fundamental technology and utilization of social big data by the National Institute of Information and Communications Technology (NICT), Japan. Special acknowledgment also goes to Hokkaido Agricultural Research Center and Hitachi Solutions Ltd. for assistance in preparing and conducting the experiments.

My devotion to our beloved family is incomparable. The moment when I got injured and frustrated during the experiment I found my fiancée Ms. Iwei Lu was there caring for me; the moment when I remorse over the passing away of my grandmother and my uncle thousands of miles away I found my parents were there consoling me; the moment when I rejoiced at the acceptance of my research paper I found my sisters and my brother were there encouraging me. This dissertation is dedicated to my dear nephew Yixuan, niece Zhiqin and Zhiqian, who accompanied me to get over hard times and shared with me their innocent laughter.

****Work out a flight path down-to-earth, and enjoy flying up high into the sky. ****

List of Figures

List of Tables

Notations

a	parameter of plane equation
b	parameter of plane equation
c	parameter of plane equation
C_e	constant variable of motor
cm	centimeter
d	raw LiDAR distance measurement
d_{corr}	corrected LiDAR distance measurement
d_i	distance of each measured point to the interpolation point
e	ground elevation of surveying point
e_{RTKi}	ground elevation of and the RTK-GPS data
e_{UAVi}	ground elevation of the UAV-LiDAR system data
g	gram
g_x	acceleration components in x axial from the accelerometer
g_y	acceleration components in y axial from the accelerometer
g_z	acceleration components in z axial from the accelerometer
h_{fix}	height difference between PPK-GPS rover antenna and LiDAR device
h_{ppkgps}	altitude of PPK-GPS
Hz	Hertz
I	DC current through each motor
kg	kilogram
K_o	modified Bessel function
m	meter
m_x	magnetic intensity components in x axial
m_y	magnetic intensity components in y axial
m_z	magnetic intensity components in z axial
mrad	milliradians
n	rotational speed of each motor
N_t	the total number of pixels within a unit area
N_v	the number of pixels that are classified as vegetation
n_{idw}	the number of measured points included in the IDW model
n_{spl}	The number of measured points included in the spline model
nm	nanometer
p	power parameter of IDW model
R	equivalent resistance of each motor's coil
$R(d_i)$	regularized algorithm's coefficient
$T(x, y)$	regularized algorithm's coefficient
U	voltage imposed upon each motor
V	voltage
W	watt
w_i	weighting factor of each measured point

ω_x	raw rotation rates of x axial from the gyroscope
ω_y	raw rotation rates of y axial from the gyroscope
ω_z	raw rotation rates of z axial from the gyroscope
x	easting coordinate of each interpolation point
y	northing coordinate of each interpolation point
z	elevation coordinate of each interpolation point
$\hat{z}(x, y)$	estimated ground elevation of the interpolation point
$z(x_i, y_i)$	measured point's ground elevation
x_i	easting coordinate of each measured point
y_i	northing coordinate of each measured point
z_i	elevation coordinate of each measured point
Θ	magnetic flux of each motor's coil
θ	pitch
θ_{acce}	calculated pitch from accelerometer
θ_{gyro}	calculated pitch from gyroscope
ϕ	roll
ϕ_{acce}	calculated roll from accelerometer
ϕ_{gyro}	calculated roll from gyroscope
ψ	yaw
ψ_{gyro}	calculated yaw of UAV platform from gyroscope
ψ_{magn}	calculated yaw from magnetometer,
ρ_{NIR}	spectral reflectance of NIR waveband of the remote sensing data
ρ_{red}	spectral reflectance of red waveband of the remote sensing data

Acronyms and Abbreviations

ADC	Agricultural Digital Camera
BC	Before Christ
CMOS	Complementary Metal-Oxide-Semiconductor
DC	Direct Current
Dr.	Doctor
DGPS	Differential Global Positioning System
DSM	Digital Surface Model
ExG	Excessive Greenness
FGV	Fractional Green Vegetation
GCP	Ground Control Point
GCS	Ground Control Station
GIS	Geographic Information System
GLONASS	GLObalnaya NAvigatsionnaya Sputnikovaya Sistema
GNSS	Global Navigation Satellite System
GPS	Global Positioning System
GRRI	Green-Red Ratio Index
GS	Growth Stage
HALE	High-Altitude Long-Endurance
HTOL	Horizontal Take-Off and Landing
IDW	Inverse Distance Weighting
IMU	Inertial Measurement Unit
IoT	Internet of Things
IRNSS	Indian Regional Navigation Satellite System
K	Potassium
LiDAR	Light Detection and Ranging
LiPo	Lithium-Polymer
LOOCV	Leave-One-Out Cross -Validation
MALE	Medium-Altitude Long-Endurance
MAV	Micro Aerial Vehicle
MEMS	Micro-Electronic Magnetic System
N	Nitrogen
NDVI	Normalized Differential Vegetation Index
NGBDI	Normalized Green-Blue Difference Index
NGRDI	Normalized Green-Red Difference Index
NIR	Near Infrared
P	Phosphorus
PAs	Pilotless Aircrafts
pH	potential of Hydrogen
PIF	Pseudo-Invariant Feature
PPK-GPS	Post Processing Kinematic Global Positioning System

QZSS	Quasi-Zenith Satellite System
RGB	Red-Green-Blue
RMSE	Root Mean Square Error
RPAs	Remotely Piloted Aircrafts
RPVs	Remotely Piloted Vehicles
RS	Remote Sensing
RTK-GPS	Real Time Kinematic Global Positioning System
SfM	Structure from Motion
SSCM	Site-Specific Crop Management
SVM	Support Vector Machine
TIN	Triangulated Irregular Network
VTOL	Vertical Take-off and Landing
VRS	Virtual Reference Station
UAS	Unmanned Aircraft System
UAV	Unmanned Aerial Vehicle
USAF	United State Air Force
USB	Universal Serial Bus
UTM	Universal Transverse Mercator
VCC	Vertical Canopy Coverage
VDVI	Visible-Band Difference Vegetation Index
WGS	World Geodetic System
3D	Three Dimensional

Chapter 1 Introduction

1.1 Research Background

1.1.1 Evolution of Agriculture

As the rapidly changing world keeps gaining momentum in respect of almost every aspect of human life towards the direction of automation and intellectualization, agriculture, which has always been the cornerstone of economic and social development both regionally as well as globally in human civilizations, is also transforming itself into a high-level scientific industry. Farming originated and evolved independently in many regions all over the world, yet either the agricultural total output or the unit output stagnated for tens and hundreds of centuries. Meanwhile, farming-engaged population kept increasing due to the lack of efficient equipment, high-quality plant seeds, scientific agronomic methodologies, and etc. Along with the global growth of population and social developments in human civilization, agriculture industry has also experienced several major transformations: from subsistence agriculture to commercialized agriculture, intensive agriculture, industrial agriculture, and eventually the precision agriculture.

Subsistence agriculture refers to farming systems that depend on manpower as well as animal power, by using hand tools and simple instruments to conduct agricultural production activities in ancient times. Mainly for self-sufficient and self-contained purpose under natural economic circumstances, subsistence farming enjoys the advantages of low energy consumption and non-pollution but also has to suffer from low-yield or worse: total crop failure in case of occurrence of natural disaster. Throughout the history of human civilization, famine, a widespread scarcity of food, was closely associated with each social change and reformation. The first famine in history was recorded 441 BC in ancient Rome, and in Somalia during 2011-2012 the death toll of famine was estimated up to 285,000, caused by 2011 East Africa drought [1]. In order to combat famine in respect to both frequency and severity, implementation of improved farming techniques and farming models to increase crop yield has been witnessed all over the globe.

Between the 16th and 17th century in western countries and at the beginning of the 20th century in oriental counties commercialization of agriculture emerged as feudal system fell apart, and farmers began to possess their own farmland as private property. Thereafter

prosperous farmers turned themselves into capitalist landowners and they strived to improve crop yields not merely for subsistence needs but for making a fortune by selling the surplus crops to areas that demanded that product. More and more farmlands were transferred and consolidated in the following years to certain distinguished individuals or corporations. As a result, surpluses of agricultural production were by and large guaranteed. The eagerness for profit was insatiable, and the power of capitals was infinite in promoting agricultural development. To furthermore increase crop yields, innumerable agricultural researches were initiated and experimental achievements on plants, soil, water, and all other crop related topics emerged on after another. By the year of 1642, Dr. Jan Baptist van Helmont conducted the famous 5-year willow experiment. Based on quantitative analysis, Dr. Helmont tested whether plants obtain their mass from soil and he concluded that the gain mass of wood, barks, and roots arose out of water only [2]. From then on, between the 17th and 18th centuries knowledge on the mineral nutrition of plants widely disseminated owing to several European naturalists. In 1727 Stephen Hales published experiment results on the nature of transpiration: the transport of water and solutes in plants [3]. By the 1840s, Professor Justus Freiherr Von Liebig, the pioneer of the agricultural chemistry and the "father of the fertilizer industry" investigated on indispensable mineral salts including nitrogen (N), phosphorus (P), and potassium (K) and concluded that N, P, and K, among other mineral elements are essential to plant growth. Besides, Professor Liebig put forward the "Law of the Minimum", arguing that plant growth relies on the supply of the scarcest mineral nutrition that is available to the plants [4]. The impact of "Law of the Minimum" on the agriculture industry has been far reaching. Professor Liebig himself advocated the agricultural application of nitrogen fertilizer to solve the problem of food availability, which fundamentally enlarged agricultural activity into a capitalized industry on an unprecedented scale.

The development of agricultural techniques has been through zigzagging process. It was not until the 1770s when the industrial revolution brought steam-powered machines into not only factories but also farmlands that intensive farming on large scale came into realization. However, as the old cliché goes that development of science and technology is always a double-edged sword: the advent of efficient agricultural machinery made it possible to produce adequate food for feeding more population, and global population boomed up to about 800 million for the first time by the end of 18th century after the securing of food production through massive agricultural mechanization [5], which in turn asked for more provision of food and biomass resources as industrial raw materials. Urgent food demand

further stimulated scientists and researchers to discover outstanding plant breeds suitable for intensive agriculture; to develop new plant varieties with specific capabilities such as drought tolerance, lodging-resistance, and high yields; to introduce new farming technology including man-made drainage systems, pesticides and herbicides, and synthetic fertilizers, etc. The invention of ammonia from nitrogen gas (N2) and hydrogen gas (H2) by Fritz Haber in collaboration with Carl Bosch in the 1910s fundamentally changed agriculture industry globally. The Haber–Bosch process of artificially synthesizing ammonia is still mainly used to produce nitrogen fertilizer today, accounting to 450 million tones anhydrous ammonia, ammonium nitrate, and urea per year [6]. In combination of pesticides application and adaptation of high-power agricultural machinery, massive use of synthetic fertilizers improved productivity of agricultural land dramatically through intensive farming techniques with higher levels of input and for higher levels of output per unit area of farmland.

Nowadays agricultures in most areas across the globe are intensive in one or more respects: capital, labor, machinery, fertilizer, and agricultural chemicals. As investments in intensive agriculture rely on industrial methods heavily, it is also referred to as industrial agriculture. At the meantime gene-modified breeds as well as hybridization crops also obtained rapid popularization. Around the 2010s breeding scientist Longping Yuan announced the success of a new strain of hybrid rice that was reported to produce 13.9 tons of rice per hectare [7], when the world population exceeded 6.9 billion [8]. In order to feed such a large number of mouths and to swipe out starvation in a global context, updating methodologies and equipment are introducing into intensive agriculture to cope with such issues like the unbalance of agricultural ecology: the abuse of agricultural chemicals, decreasing underground water level, soil compaction and erosion, land degradation and dissertation, etc. [9]. Using automated agricultural machinery and variable-rate technology in precision agriculture or site-specific crop management (SSCM) emerged as the times required in recent years, which enables each farmer to be able to feed 265 people on average, comparing with each farmer feeding 26 people on average in the 1960s [10].

1.1.2 Precision Agriculture

Precision agriculture improves upon the advantageous techniques used in intensive agriculture, whilst reduces the negative impacts on agricultural ecology for a low-input, high-efficiency, and sustainable agriculture [11]. Precision agriculture could also be called as ecological agriculture or eco-agriculture to some extent, as its prime objective is to construct

a decision supporting system by acquiring site-specific field information and responding to the within-field spatial variability [12]. The ultimate goal of precision agriculture is to build a sustainable agriculture by protecting arable land from degradation and pollution, and utilize agricultural inputs in a more efficient way without compromising the high-productivity of the present intensive agriculture system. The demand of precision agriculture rose after the completion of agricultural mechanization in well developed countries in the early 1980s, when farmers intended to maximize profit by dividing vast farmlands into smaller management zones and varying treatments of fertilizers and/or agricultural chemicals in response to the variability of each specific management zone [13]. Meanwhile researchers as well as policy-makers became concerned about environmental issues like N leaching, water pollution, and etc. [14]-[16].

The concept of precision agriculture was brought out by researchers at the University of Minnesota in 1985, designing variable-rate lime input experiments for improving soil's pH (potential of hydrogen) value within a farmland [17]. Thereafter, the importance and profitability of precision agriculture got universally acknowledged, many researchers all around the world initiated precision agriculture related projects including sensors, automated agricultural machinery, variable-rate agricultural implements, and etc. In 1989 Wagner and Schrock installed a pivoted auger grain flow sensor on a commercial combine harvester to determine within-field yield variations of wheat, so that general information on field productivity could be obtained [18]. In 1999 Yule and et al. developed a differential global positioning system (DGPS) based data acquisition system equipped on a tractor to map within-field variability of topology and soil moisture content, so that areas that needs remedial operations could be identified [19]. In 1999 Tian and et al. developed an intelligent sensing and precision spraying system based on machine vision technology to estimate weed density and size, so that herbicide application could be reduced by realizing site-specific weed control [20]. In 2001 Hummel et al. developed a near infrared (NIR) soil sensor to measure organic matters in soil and surface as well as subsurface soil's moisture contents for documenting the spatial variability of soil parameters [21]. In 2001 Noguchi et al. developed a robot tractor based on RTK-GPS (Real Time Kinematic Global Positioning System), gyroscope, and IMU (Inertial Measurement Unit) [22], which could conduct various kinds of field operations with acceptable accuracy. From then on vehicle and robotics laboratory in Hokkaido University developed a dual robot tractors system in master-slave fashion, and multi-robot tractors system operating in collaboration with each other to further improve

working efficiency. Ever since the beginning of 21st century, numerous sensors are being launched into agricultural market: handheld devices, equipment onboard ground vehicles, airborne instruments, and satellite sensors have greatly enriched the means of acquiring field information. In essence, the progress of precision agriculture has been closely linked to such technologies including agricultural mechanization and automation, GPS, GIS (Geographic Information System), IoT (Internet of Things) techniques, sensors, variable-rate applicators, remote sensing techniques, and etc., depicted in Fig.1. 1.

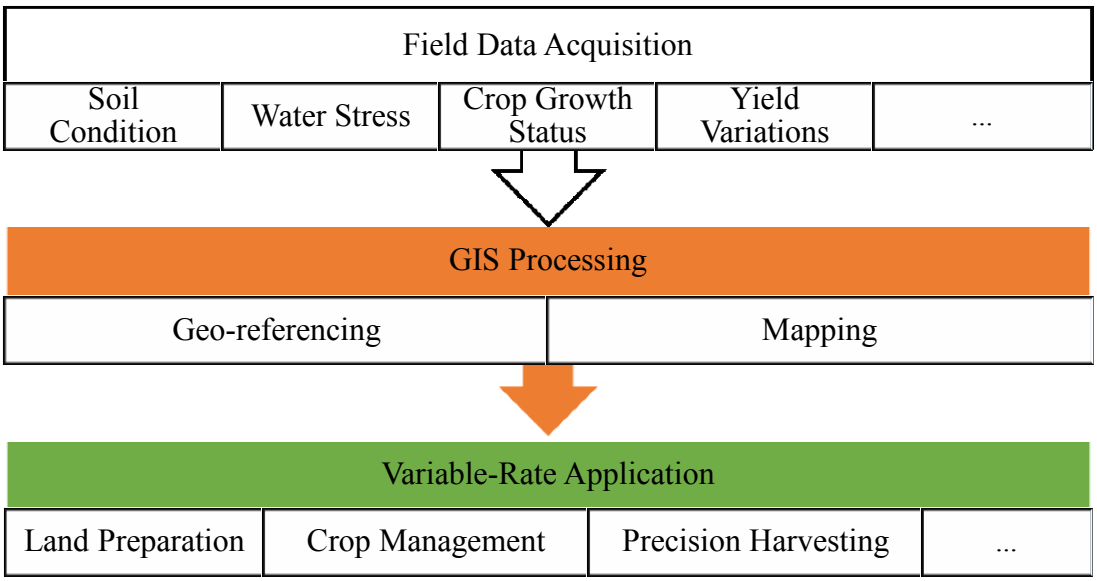

Fig.1. 1 Diagram of precision agriculture

As the massive production capability and reliability of integrated circuit products, or microchips, have been validated by market since the 1960s, numerous kinds of industrial sensors that are capable of collecting and processing instantaneous information were developed, which marked the advert of information era. GPS is deemed as one of the most successfully commercialized industrial technologies thanks largely to the extensive use of the miniaturized and economical integrated circuit products, which consists of three main segments: the space segment, the ground control segment, and the user segment. In a sense it is like that each point on or nearby the planet has been virtually mapped and attached with a unique coordinate, and all what the user needs is a GPS receiver to “estimate” one’s location (coordinates) on the map based on trilateration method by measuring distance between GPS receiver and GPS satellites [23].

The technical terminology of GNSS (Global Navigation Satellite System) is nowadays more preferable to GPS by researchers, which is a generic term including several satellite

navigation and positioning systems providing global services. GNSS mainly comprises the most widely used GPS of the United States of America, GLONASS (GLObalnaya NAvigatsionnaya Sputnikovaya Sistema) of Russia, Beidou of China, GALILEO of European Union, and each of them provides global positioning services at different levels of accuracy. It also includes QZSS (Quasi-Zenith Satellite System) of Japan as well as IRNSS (Indian Regional Navigation Satellite System) of India which provides regional positioning services to some extent. Theoretically it needs at least four GNSS satellites and each of them forms an unobstructed line of sight to a GNSS receiver in order to acquire a "fixed" 3D (three dimensional) coordinates. However, more than four GNSS satellites are usually included simultaneously into different navigation and positioning algorithms for higher accuracy, as the extra cost of superfluous access to GNSS satellites from multiple systems than to a single system is next to negligible. Fig.1. 2 showed an easy access to multiple GNSS satellites using a smart phone in northern China on 3 October 2017, from which we can see that 24 GNSS satellites in total were visible by that time: 9 GPS satellites, 6 GLONASS satellites, and 9 Beidou satellites, respectively.

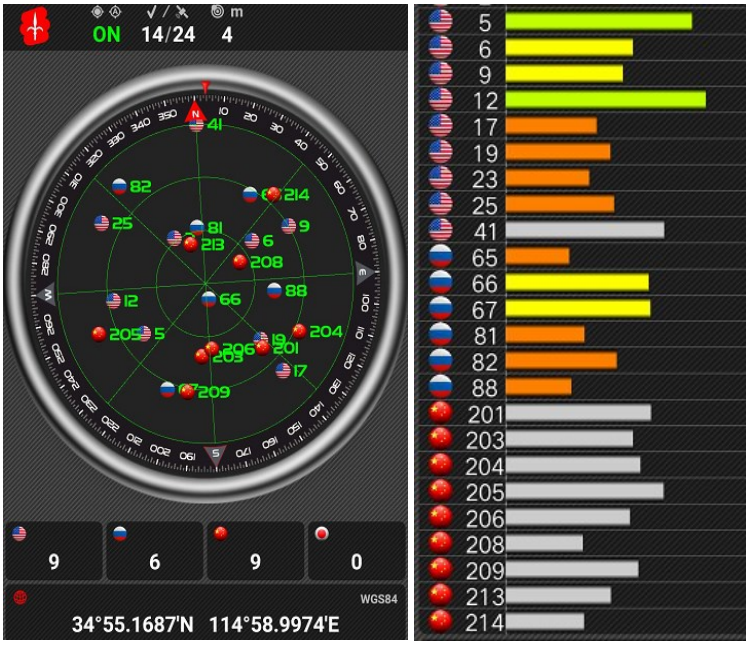

Fig.1. 2 Access to multiple GNSS satellites

Yet the inevitable problem of low positioning accuracy (less than five meters horizontally) resides with GNSS standalone positioning mode, due to clock precision, ionospheric disturbance, and etc. Thus, different augmentation systems were created to enhance positioning accuracy, integrity, and availability. DGPS improves GNSS positioning

accuracy up to about one meter, using a network of ground reference stations which continuously broadcast the difference of distance between the known fixed positions and the estimated positions indicated by the GNSS positioning algorithm. Subsequently, GNSS rover rectifies each estimated pseudo-range between GNSS receiver and GNSS satellites according to the correction information from base station, shown as Fig.1. 3. Basically RTK-GPS works in the same manner as that of the DGPS, providing two to five centimeters accuracy; the only difference is that RTK-GPS rover receives correction signal of carrier phase information from base station instead of pseudo-range measurements. Centimeter-level accuracy as it is, RTK-GPS requires a stable data link either via the radio signal or cellular network between the GNSS rover and the base station. On the other hand, PPK-GPS (Post Processing Kinematic Global Positioning System) processes the positioning information that is saved on board the GNSS receivers after each operation. Similar to RTK-GPS, one GNSS receiver remains stationary as a ground base station at a known position, whilst the other GNSS receiver that "observes" the same combination of GNSS satellites (usually within twenty kilometers from the ground base station) works as a rover receiver. However, when compared with RTK-GPS, PPK-GPS provides a more precise relative positioning result as it traces both backward and forward through the carrier phase data of these two GNSS receivers multiple times. Nonetheless, the absolute positioning accuracy of PPK-GPS relates to the accuracy of the "known" position of the ground base station, which is usually acquired by using a RTK-GPS module or estimated from hour-long measurements of standalone GNSS positioning.

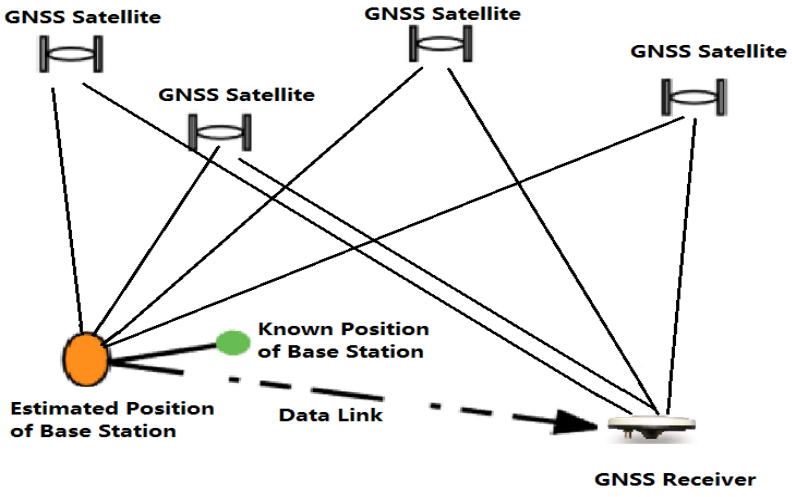

Fig.1. 3 Principle of DGPS

The utilization of global positioning services based on GNSS technology has profound impact on the implementation of precision agriculture, which tagged each field sample's attribute value (soil condition, water stress, crop growth status, yield variation, and etc.) with

an accurate spatial coordinates – a process called geo-referencing or geo-coding. The realization of processing these geo-referenced attribute values in GIS environment improved field sampling efficiency and spatial accuracy at an unprecedented level, as GIS applications are effective tools that enable researchers to visualize, edit, integrate, and analyze spatial-temporal information in a digitalized fashion [24]. It is also worth mentioning that GIS applications are capable of relating spatial-temporal information from different sources that is geo-coded by using GNSS devices or geo-referenced by measuring GCPs' (Ground Controlling Point) geographical coordinates afterwards. GNSS based autonomous navigation of agricultural machinery, i.e., tractors, transplanters, combine harvester, chemical spring airplanes and drone, and etc., have been breaking new grounds in precision agriculture domain. The mobile platform that not only knows where it is but also is aware of what it is about to do: changing advancing velocity, making a turn, controlling attached applicators according to a prescription map, and etc. Agricultural machinery equipped with GNSS receiver also greatly improves logistical efficiency, as the display of real-time feedback of vehicle's position in GIS applications provides plentiful information for decision-making relating to operation scheduling, path planning, shuttle truck arrangement. With the aid of accurate GNSS navigation and positioning techniques and the powerful GIS data management capabilities, we have good reason to believe that provision of adequate food, preserving agricultural ecology, and guaranteeing industrial profit would be brought into equilibrium in the future precision agriculture.

1.1.3 Agricultural Remote Sensing

In precision agriculture industry, information is king. The abundancy, frequency, as well as accuracy of the acquired field information influence decision-makers greatly on determining the appropriacy of each SSCM operation. The means of obtaining field information are various. Primitively field survey by experienced farmers was used for the last thousand years, in which visual inspection of stalk density, leaf area and pigment, number of pests, and etc., acted as a sole information source. Not so long ago until mineral nutritious elements were distinguished inside plant tissues that precise laboratory experiments came into realization by taking samples from the field. Later on handheld devices are included into field sampling operation, which mainly take advantage of spectroscopic technologies. However, either it should be visual inspection or instrumental sampling in the field, data collection can be enormously time consuming for the current large-scale farming. Moreover,

it is sometimes reported that the collected field information can be very deceptive when samples are scare or partially focused in featured regions.

Remote sensing is the science and art of obtaining information about an object, area, or phenomenon through the analysis of data acquired by a device without making physical contact with the object, area, or phenomenon under investigation [25], which has been successfully used as an effective and accurate means of collecting field information from the farmland-level, to the regional level and global level. On the basis of different types of remote sensing platforms carrying onboard sensors, agricultural remote sensing could generally be categorized into satellite remote sensing, aerial remote sensing and near-ground remote sensing. According to a survey conducted by Jacqueline and et al., at Purdue University of crop input dealers and their use of precision technology, up to 39.2% of the respondents used satellite or aerial remote sensing data for precision agriculture. The increasing trend of monitoring crop growth status from remote sensing imagery is now being accelerated by the easy access of civilian UAVs (Unmanned Aerial Vehicle).

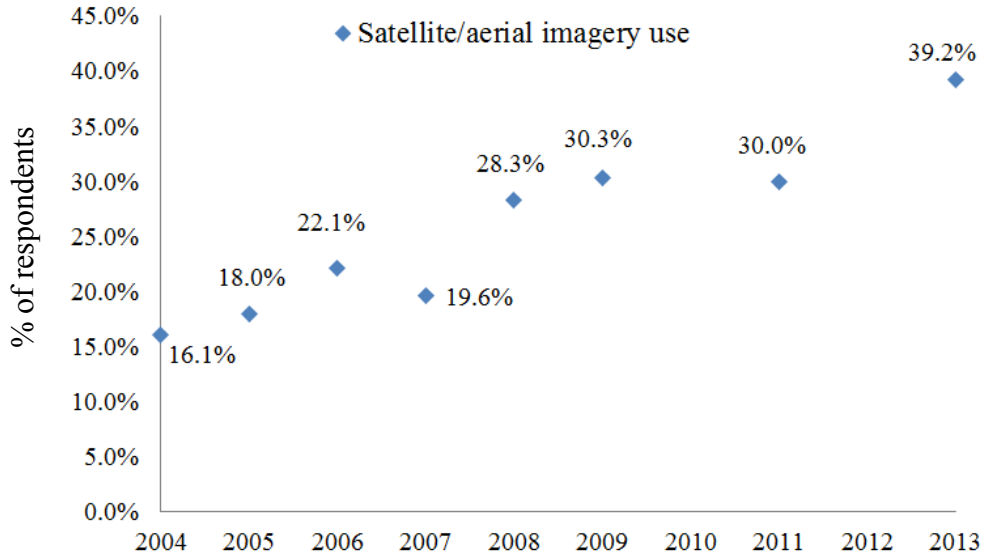

Fig.1. 4 Agricultural remote sensing in agriculture (based on a survey by Jacqueline K. and et al.)

Traditionally, multi-spectral satellite imagery has been successfully used to detect vegetation coverage, monitor crop growth status, and estimate crop yield, etc., in large scale [26], [27]. Through quantitative analysis of digitalized numbers of different bands of satellite images, or more often, of various kinds of vegetation indices calculated from the reflectance or radiance of specific bands, regression models could be built between remote sensing data

and ground truths. However, low spatial resolution, long revisiting-period as well as atmospheric effects, or weather interference, are known as inherent flaws of such kind of multi-spectral satellite imagery used in precision agriculture domain. On the other hand, aerial remote sensing using airplanes has been introduced into medium-scale agricultural applications as a supplementary method and often carried out as one-time operations since the 1950s [28]. Whilst near-ground remote sensing is often referred to as frame or pillar based applications and sensing systems that are installed on agricultural vehicles in the past, and recently the cutting edge application of small fixed-and/or rotary-wing drones or UAVs used in small-scale and experimental fields, with various kinds of commercial RGB cameras, multi-spectral cameras, and laser scanners mounted upon, shown in Fig.1. 5.

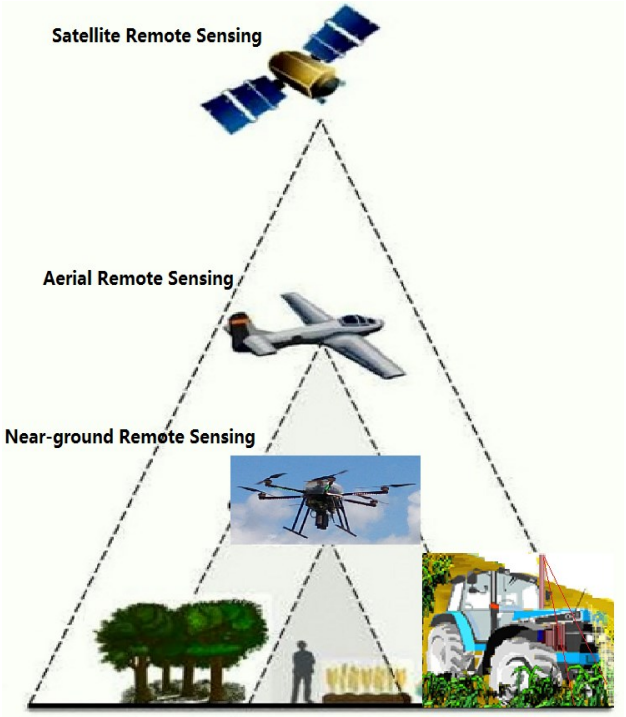

Fig.1. 5 Different platforms used in agricultural remote sensing

According to the definition of Federal Aviation Administration and the United State Air Force (USAF), UAV refers to an aircraft that is operated without the direct human intervention from within or on the aircraft, can fly autonomously or be piloted remotely, uses aerodynamic forces to provide vehicle lift, can be expendable or recoverable, and can carry a lethal or nonlethal payload. UAVs have also been called drones, RPVs (Remotely Piloted Vehicles), RPAs (Remotely Piloted Aircrafts), PAs (Pilotless Aircrafts), and other terms over the years depending upon their specific working scenarios. Current developments in UAVs trace their beginnings to World War One, and the application of modern UAVs emerged in

late 1950s in such manners that the pilot has real-time remote monitoring and controlling of the aircraft through command link and telemetry systems, in the development of unmanned aerial reconnaissance projects initiated by the USAF. Meanwhile, applications of UAV for non-military purposes was long time in its infancy until 2010s, when the multi-copter UAVs related industries were promoted as new stimulus for booming economy by several countries including China, the USA, Germany, and other governments. By then, the most intense use of commercial UAVs took place in Japan, where vertical take-off and landing (VTOL) helicopter-style UAVs are extensively operated under the jurisdiction of the Ministry of Agriculture, Forestry and Fisheries for chemical spraying. Nowadays civilian UAVs come in various kinds of shapes and sizes with widespread applications extending from professional topographic surveying and recreational aerial photography, to monitoring disaster site, data collection for precision agriculture, logistics, etc., due to the advantages of low cost, versatility, good maneuverability and efficiency.

Fig.1. 6 Constitutional diagram of UAS (image courtesy: jDrones)

Furthermore, the conception of UAS (Unmanned Aircraft System) was recently put forward, shown in Fig.1. 6, which refers to an integrated system usually compromised of the unmanned aircraft, onboard navigational and controlling unit, data link system, payload, peripheral equipment, and a GCS (Ground Control Station). The on-board navigational and controlling unit usually includes the micro-computer, battery managing system, GNSS unit, MEMS (Micro-Electronic Magnetic System) unit, gyroscope, barometer, and etc. The data link system connects the GCS with the unmanned aircraft through telemetry radio. And a

personal computer or a tablet would usually suffice as a GCS for most of the UAS applications to upload command to the aircraft and also receive flight data from the aircraft. UAS is generally categorized as VTOL or the rotary wing type, HTOLs (Horizontal Take-Off and Landing) or the fixed wing type, according to their shapes, and lift forces. Based on the flight duration and altitude, it could also be divided into High-Altitude Long-Endurance (HALE) UAV, Medium-Altitude Long-Endurance (MALE) UAV, and short range UAV. Based on the overall size and weight, it could be further categorized as small UAV and Micro Aerial Vehicle (MAV). The detailed description of the UAVs is shown in Table 1. 1.

Table 1. 1 Categories of UAVs

Type	Shape	Weight	Altitude	Endurance	Range	Power
HALE UAV	Fixed wing	＞1500	＞14000	＞24	＞1000	Engine
MALE UAV	Fixed wing	150~250	3000	3~6	30~100	Engine
Short range	Fixed/rotary	25~150	3000	＜3	10~30	Engine
Small UAV	Fix/rotary-wing	＜25	＜1000	＜1	＜20	Engine/battery
MAV	Rotary/flapping	＜5	＜250	＜1	＜10	Battery

Low-altitude UAV remote sensing data may be acquired more cost-effectively, with excellent maneuverability as well as increasing spatial resolution, and with greater safety when compared with manned aircrafts [29]. Generally there are three kinds of low-altitude UAVs that are widely utilized in agriculture industry. Helicopter-style UAV is featured with two heavy propellers which indicate massive potential safety hazards in case of mechanical failure or accidental operation. The severe vibration is another issue when precision measuring instruments such a camera, a laser scanner, and a LiDAR (Light Detection and Ranging) are installed the helicopter-style UAV. As the helicopter-style UAV adopts a gasoline engine as its power source, the payload capability is considerably high and the flight duration is also satisfactory. As such, the application of helicopter-style UAVs is usually limited in agricultural chemical spraying. Fixed wing UAV is, on the contrary, very lightweight and capable of long-time flight. The aerodynamics design generates lift force which depends on pneumatic difference of air pressure between top surface and bottom surface of the wing, shown in Fig.1. 8. However, due to structural restrictions, fixed wing UAV's payload capacity is rather low and cannot hover over a specific area of interest. Thus, fixed wing UAV is only suitable to capture aerial photographs to monitor crop's growth status over medium-scale farmland from 10 hectares up to 100 hectares in one sole flight. As the development and breakthrough in industrial application of lithium-polymer (LiPo) battery,

together with the improvement of GPS performance, commercialized micro brushless motors' reliability, and MEMS IMU measuring accuracy, the versatile multirotor UAV appeared into civilian market at the beginning of this 21st century, shown in Fig.1. 9. The number of propellers of multirotor UAV generally ranks from 4 to 12, and the payload capacity increases with the number as well as the size of the propeller. The overall weight of multirotor UAV used in agriculture industry varies from several hundred grams to tens of kilograms, and the overall size comes in various levels from palm-sized to two meters in diameter.

Fig.1. 7 Helicopter-style low-altitude UAV of Yammar (YH300)

Fig.1. 8 Fixed wing low-altitude UAV of Ag Eagle (RX60)

Fig.1. 9 Low-altitude multirotor UAV of EnRoute (CH940)

1.2 Research Objectives & Organization of Dissertation

In this study, we are going to develop and validate an agricultural remote sensing system based on the low-altitude UAV platform by integrating multiple sensors. The primary objectives are to acquire field information for the corresponding implementation of precision agriculture operations in an accurate and efficient manner. This dissertation would include three agricultural remote sensing projects such as conducting farmland topographic surveying, mapping the within-field spatial variations of wheat stalk density, and mapping the within-field spatial variations of wheat yield.

In Chapter 1, the evolution of agriculture and the crying needs for the precision agriculture have been overviewed. The increasingly important role of UAVs in the agriculture industry, especially in terms of agricultural remote sensing domain, was also discussed.

In Chapter 2, the issue of the unevenness of farmland surface was put forward, which causes crop die-off due to stagnant waters and other problems of non-uniformity of crop growth. In response, a UAV-LiDAR system was developed for conducting topographic surveying, and the resulting topographic map would be further utilized by the precision land levelling machinery. Firstly, the working principal of LiDAR was explained, and the integration of LiDAR distance measurements, UAV platform's attitude information, and the PPK-GPS coordinates was described in detail. Subsequently, the accuracy of the UAV-LiDAR topographic surveying system was validated by conducting an experiment over a wheat field in Hokkaido University, Sapporo, Japan, and the topographic data was compared with the corresponding RTK-GPS altitude. Another experiment conducted in a sugarcane field in Mackey, Australia also verified the feasibility of using this UAV-LiDAR topographic surveying system to detect bugles and pits inside the experimental fields.

In Chapter 3, different interpolation models were introduced to generate topographic maps by using the topographic data acquired from the UAV-LiDAR topographic surveying system. The accuracy of each resulting topographic map was validated by comparing the ground elevation data that were extracted from the topographic maps with the corresponding RTK-GPS altitude data. Furthermore, an aerial photogrammetric digital surface model (DSM) was generated and integrated with the topographic data of the UAV-LiDAR system, as the DSM has the advantage of large ground coverage whilst the topographic data of the UAV-LiDAR system has the advantage high accuracy.

In Chapter 4, the importance of timely monitoring of wheat growth status and estimation of wheat stalk density during the early growth stages was firstly addressed. Then a multispectral camera was integrated upon the UAV platform for acquiring images of a wheat field. Through image processing a NDVI map of the field under study was generated, and accordingly different models of vegetation coverage indices were presented. The vegetation coverage indices were correlated with the field samples of wheat stalk density, and the map that demonstrates the within-field variations of stalk density was produced for variable-rate nitrogenous topdressing.

In Chapter 5, the multi-temporal monitoring of wheat growth status was conducted by interpreting both multispectral satellite images and UAV Ortho-mosaic images acquired from a consumer digital camera. Wheat lodging could be spotted in the UAV Ortho-mosaic images clearly, and the vegetation index of the high-resolution UAV Ortho-mosaic images showed high correlation with the corresponding vegetation index of the satellite images. Finally, field sampled wheat yields were used to conduct stepwise regression with several vegetation indices extracted from the UAV Ortho-mosaic images. Based on results of the stepwise regression model, a map was generated that reflects the within-field spatial variations of wheat yield.

Chapter 6 summarized the main research results by drawing an abstract for the whole thesis.

Chapter 2 Conducting Topographic Survey Using UAV-LiDAR System

2.1 Introduction

Topography is the study of earth surface shapes and features, and topographic map refers to a 2D (two-dimensional) graphic representation of a terrestrial or 3D (three-dimensional) land surface feature using contour lines, hypsometric tints, and relief shading [30],[31]. In precision agriculture, high accurate topographic maps are essential to such operations including soil preparation, drainage arrangement, land forming and levelling, and etc. Surface unevenness of farmlands has been pointed out as a major issue that affected agricultural drainage efficiency of the current irrigation systems, which have been under great pressure for producing more with lower water supplies around many regions of the world [32]. Hu and et al. reported in 2014 that over 20% of irrigation water could be wasted due to rough land surface of paddy fields [33]. Besides, most kinds of plants including wheat, corn, soybean, and etc., are vulnerable to stagnant water throughout germination period to early growth stages. Either it be man-made irrigation or natural rainfall, puddles are likely to ensue inside farmland over lower areas, which are usually considered as potential threat that leads to crop drowning and occurrence of infestation as well as plant diseases due to high humidity, shown in Fig.2. 1. Rickman concluded in 2002 that unleveled rice fields suffered about 24% yield loss in average when compared to the effectively leveled ones for the same rice variety and the same fertilizer input [34].

Fig.2. 1 Crop failure due to stagnant waters

As precision land levelling facilitates surface drainage, improves crop establishment, reduces occurrence of infestation and plant diseases, and increases crop yield [35], many researchers both in academia and industry have proposed different methodologies on removing mounds and puddles inside farmland. Apart from conventional land preparation using ploughs and harrows after each crop season, generally two major proven techniques that have already been put into practice for precision land levelling could be enumerated: laser-assisted land levelling and GNSS based land levelling [36]. Nowadays not only in developed countries like the United States and Japan but also in developing countries such as China, India, and Brazil, laser-assisted land levelling techniques are gaining momentum rapidly, as it works in a simple fashion [37]: the laser transmitter continuously emits a laser plane, which is intercepted by the laser receiver in real time so that the height deviation to the target height plane could be calculated; the height deviation is sent to the control box, and the scraper automatically goes up and down according to commands from the control box aiming at minimizing the deviation between the laser receiver and the target height plane; as the scraper adapts the height, soil of higher ground is cut and hold in the bucket until it is carried to lower ground and got released. Furthermore, Li and et al. in 2012 developed an attitude measurement system for scraper of a laser-controlled land leveler by fusing data from a tri-axial accelerometer and a digital gyroscope, which made the whole levelling system work more efficiently and reliably [38]. Although it is explicit in structure and easy to operate, laser-assisted land leveler has its inherent flaws: the selection of location and preset height of the laser transmitter determines the cutting depth of each location (cut/fill ratios) directly, and without an accurate topographic land survey it is next to impossible to optimized the volumes of relocated earth. It is not unusual that operators find out that most of the time the scraper hangs too high to cut any soil (idle operation), or worse, the tractor gets stuck and slips over one spot and cannot move forward due to insufficient power when the cutting depth becomes too large.

On the other hand, GNSS based land leveler came into practical application since mid-1990s, when RTK-GPS service finally entered the market with an acceptable price and centimeters-accuracy for measurements of 3D positions (latitude, longitude, and altitude). GNSS based land leveler uses a GNSS receiver to measure 3D coordinates of the scraper and adjusts the scraper's height by comparing the current altitude with the desired one to complete the earth-moving operation [39]. But, it shares the same drawback with the laser-assisted land leveler: the GNSS based land leveler also needs an extra land survey, usually by

driving the GNSS receiver equipped tractor throughout the farmland prior to levelling operation in order to acquire an farmland surface elevation map. According to the elevation map drivers could preset an optimal ground height of each field and calculate cut/fill ratios for each point by using GIS technology. Either way, whether it is a laser-assisted land leveler or a GNSS based one, topographic survey is usually prerequisite, and land levelling accuracy, efficiency, as well as energy consumption is in high accordance with the delicacy of each topographic map of the farmland.

In order to generate topographic maps, new technologies including terrestrial laser scanning, airborne laser scanning, and aerial photogrammetry are recently utilized for different kinds of engineering applications like construction site, urban ecology modeling, forest monitoring, and etc. [40]-[44]. Whist theodolite, total station, and RTK-GPS module remain the conventional and primary methods that are used in common topographic surveying. Theodolite is a precise instrument for measurement of angles in both horizontal and vertical dimensions since sixteenth century; and total station is an all-electronic device developed from theodolite on the theory of electronic distance measurement [45]. Resop and et al. in 2010 compared different surveying techniques by using traditional total station and terrestrial laser scanner to monitor streambank retreat, and concluded that surveying error of total station would be significant when extrapolating to a certain reach, whist terrestrial laser scanner provides much more detailed spatial information [46]. Corsini and et al. in 2013 monitored and mapped a slow moving compound rock slide by integration of airborne laser scanner, terrestrial laser scanner, and automated total station, which quantified slope movement in the order of centimeters to a few decimeters [47]. Pablo and et al. in 2017 evaluated a mobile LiDAR system mounted on a car to develop an architectural analysis by generating 3D point cloud [48]. There are also plenty of research works and products providing digital surface model and digital elevation model based on airborne photogrammetry or satellite stereo-imagery [49]-[51], but the spatial resolution as well as vertical accuracy of such topographic maps generated from photogrammetric processing usually reaches several decimeters to tens of meters, which makes it unsuitable to be used in farmland for precision land leveling operation.

Therefore, in this study, we introduced a low-altitude UAV equipped with a high precision one-dimensional LiDAR (Light Detection and Ranging) distance measuring device to conduct topographic survey in a simple and totally autonomous manner. The research

objective is to integrate data of multiple sensors including LiDAR, MEMS IMU, and PPK (Post Processing Kinematic) GPS receivers, to generate a topographic map at farmland level by using a low-altitude UAV-LiDAR system. The accuracy of the UAV-LiDAR system based topographic surveying was validated by acquiring the corresponding RTK-GPS coordinates and through visual inspection as well.

2.2 Research Platform and Equipment

In this research we developed a UAV-LiDAR topographic surveying system by installing a one-dimensional LiDAR distance measuring device, a mini-computer, an external GPS rover receiver for PPK-GPS positioning, and other peripheral devices such as battery banks and an external GPS antenna on a small UAV. Each battery bank is meant for powering the LiDAR, the mini-computer, and the external GPS module, respectively.

2.2.1 UAV Platform and Built-in Sensors

As described in Sector 1.1.4, a hexa-copter (ENROUTE CO., LTD., Fujimino, Japan) was used as the small UAV platform in this study, shown in Fig.2. 2. This is a high-powered industrial UAV, which is originally designed for agricultural chemical spraying with the payload capacity of 6.6 kg. We altered the bottom part of this UAV so that the LiDAR, mini-computer, as well as battery banks could be fixed upon the UAV platform. The UAV itself uses two LiPo batteries and each of them is comprised of 6 battery chips (cells), which are separated and protected by aluminum plates. These LiPo batteries are capable of powering the no-load UAV for a 20-minute flight, however, as the payload increases the flight endurance become shorter. In the case of our developed UAV-LiDAR topographic surveying system, the maximum flight endurance reached up to about eight minutes when flying at the ground speed of 5 m/s and 30 meters above ground level. The specifications of the UAV are listed in Table 2. 1.

Table 2. 1 Specifications of the UAV platform

Overall size (with propellers uninstalled)	Φ1397*450mm
Propeller size	457.2mm
Battery type	LiPo 6 Cell
Battery capacity* number	99 Wh *2
Total number of Motor	6
Motor type	Zion5828-340KV

Weight	5.4 kg
Payload capacity	6.6 kg
Maximum climbing speed	5 m/s
Maximum flight speed	20m/s
Wind resistance	10 m/s

Fig.2. 2 A small UAV used in this study

This UAV utilizes an industrial standard PIXHAWK autopilot hardware as an onboard flight controller, which is designed by 3D Robotics Inc. in collaboration with ArduPilot Group. The PIXHAWK flight controller integrates several kinds of inertial MEMS sensors including a 3D accelerometer, a gyroscope, a magnetometer, and a barometer, which utilizes a high accurate and reliable algorithm for acquiring attitude information of the UAV and implementing self-balancing in real time. PIXHAWK flight controller could also records the spatial position as well as the orientation or attitude information of the UAV platform in real time when connecting with an external GPS module, which might be further analyzed for correcting LiDAR's distance measurements in this study. It has various kinds of ports that are ready to be connected with multiple sensors for augmentation purpose, shown in Fig.2. 3. Interface 1 is reserved for the digital spectrum modulation system, which is a newly released radio technology offering an interference-immune and impenetrable radio link; Interface 2 is for remote monitoring on GCS; Interface 3 is for remote monitoring controller; Interface 4 is for universal serial bus communication; Interface 5 is a serial peripheral interface; Interface 6 is for power unit; Interface 7 is for safety switch function; Interface 8 is for buzzer function; Interface 9 is for serial communicating; Interface 10 is for external GPS module; Interface 11

is for controller area network; Interface 12 is for inter-integrated circuit; Interface 13 is for analog-digital-converter to 6.6 voltage; Interface 14 is for analog-digital-converter to 3.3 voltage; and interface 15 is for light-emitting diode display.

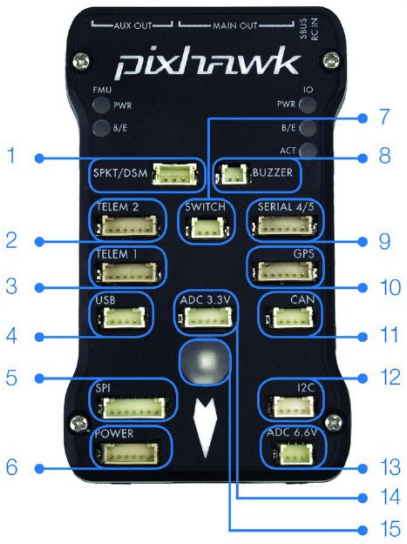

Fig.2. 3 PIXHAWK flight controller

2.2.2 LiDAR and Onboard Computer

LiDAR is originally a portmanteau term of Light Detection and Ranging, Light Imaging Detection and Ranging, and Laser Imaging and Ranging, which is a surveying method of measuring distance to a target by emitting a pulsed laser light and calculating the time or the changes of phase of the returned laser light [52]. LiDAR has a wide range of applications from meteorology to terrestrial mapping, vegetation coverage, and etc., based on the data's purpose and targeting objects. It could also be divided into terrestrial LiDAR applications and airborne LiDAR applications, according to different kinds of platforms. Within the category of airborne LiDAR applications it could further be divided into low-altitude airborne LiDAR applications and high-altitude airborne LiDAR applications, and both of them create 3D point cloud models. Low-altitude airborne LiDAR is currently the most efficient, detailed and accurate method of generating a digital surface model (DSM), while the high-altitude airborne LiDAR provides a bigger coverage with a reduction in distance measuring accuracy and spatial point density, shown in Fig.2. 4.

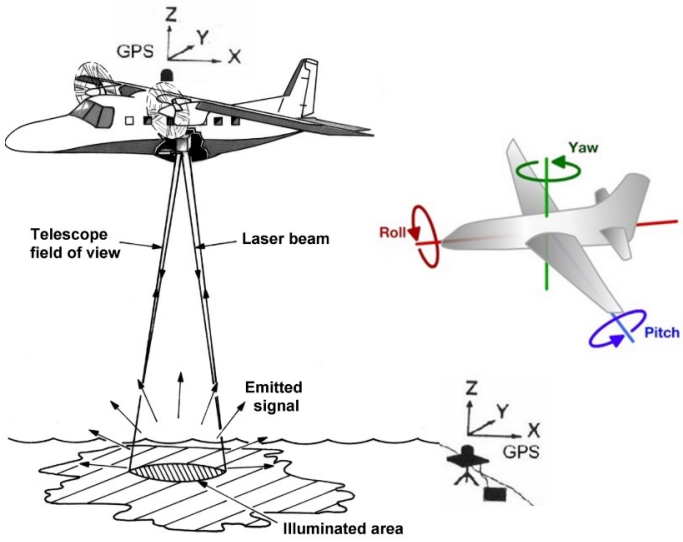

Fig.2. 4 Airborne LiDAR application

However, as shown in Fig.2. 4, in order to obtain accurate distance measurements and geographical coordinates for each measurement, the commercial airborne LiDAR system incorporate expensive RTK-GPS module and IMU sensors onboard. For small UAVs, there is not enough room for these extra but necessary auxiliary devices both physically and economically. Thus, in this study we introduced a high precision one-dimensional LiDAR device (Jenoptik, Jena, Germany) and took advantage of the inherent MEMS IMU sensors of the UAV platform's flight controller. The LiDAR distance measurement device is featured with time-of-flight measurement principle and has a measuring range up to 300 m on natural surfaces and 1 mm measuring resolution at the measuring frequency of 2000 Hz. Besides, the LiDAR distance measurement is equipped with two lasers, shown in Fig.2. 5: part 1 is transmitter optics and part 2 is pilot laser transmitter optics for collimation, whilst part 3 is receiver optics. The safety level of the laser for distance measurement is class 1, which means any case of injury of the unaided eyes of human can be excluded; whilst the safety level of the pilot laser is class 2, which means that human eye can be protected by the eyelid closure reflex against a short accidental look into the pilot laser beam without any additional protection appliances. Another advantage of this LiDAR distance measurement device is that the supply voltage has a wide range from 10 V to 30 V (direct current), which is basically immune to voltage instability and provides reliable continuous measurements. The power consumption of 5 W is also very low, which is suitable for the small UAV use as it cannot carry large volume battery bank onboard.

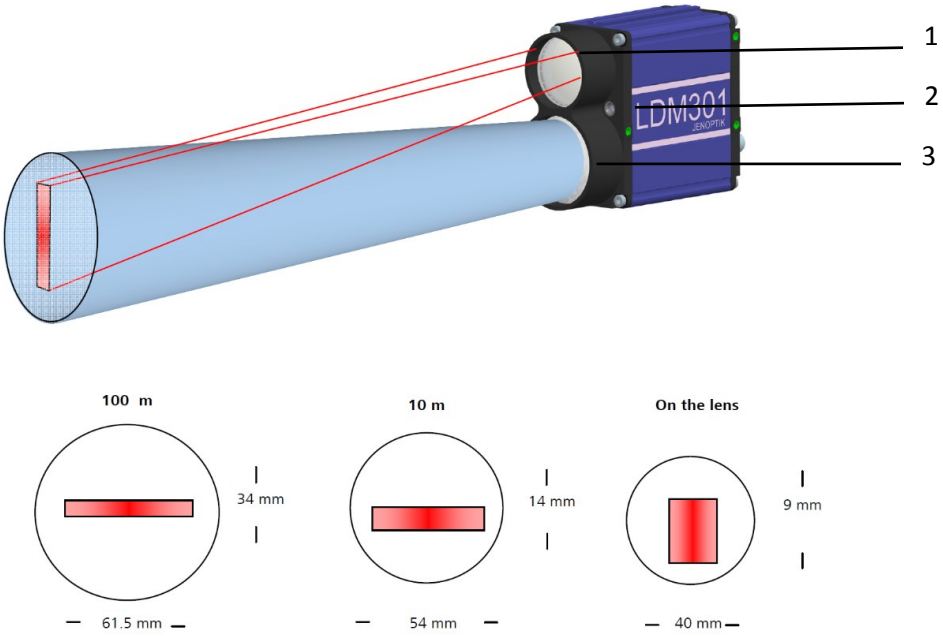

Fig.2. 5 Laser beam divergence and spatial resolution

Laser beam divergence, measured in milliradians (mrad) or degrees, is another important parameter of LiDAR distance measuring device, which is an angular measure of the increase in beam size with the distance from the transmitter optics where the laser beam emerges to a target. For many distance measurement applications, the lower the divergence of the laser beam is, the more preferable and accurate of the measurement becomes. In this study the laser beam divergence of the LiDAR distance measurement device is 1.7 mrad, and the spatial resolution of each measurement is about 60 mm * 20 mm when measuring from a distance of about 30 m, shown in Fig.2. 5.

The LiDAR distance measuring device provides various kinds of interfaces to be connected with a computer including RS232, RS422, and Profibus. A mini-computer is used to control as well as monitor the distance measuring operation, and at the same time to log and save each distance measurement onboard in real time. We adopted a light and compact mini-computer (GB-XMI1-3537, Gigabyte, Taiwan, China) in this study shown in Fig.2. 6, and utilized a USB 3.0 (Universal Serial Bus) port to connect with the LiDAR distance measuring device using a USB serial cable type A to D-sub 9 converter. The power supply of the mini-computer is 19 V DC, and the power consumption is about 65 W. The specifications of the LiDAR device and the mini-computer are listed in Table 2. 2.

Fig.2. 6 On board mini-computer

Table 2. 2 Specifications of LiDAR and onboard computer

LiDAR device	
Dimensions	136 mm * 57 mm * 104mm
Weight	800 g
Measuring resolution	1 mm
Beam divergence	1.7 mrad
Measuring laser wavelength	905 nm
Pilot laser wavelength	635 nm
Supply voltage	10 V to 30 V DC
Power consumption	< 5 W
Operating temperature	-40° C to +60° C
Operating humidity	15% to 90%
Onboard computer	
Dimensions	30 * 108 * 115 mm
Weight	400 g
Operating system	Windows 32/64 bit
CPU	Intel® Core™ i7-3537U 2GHz / 3.1GHz
Memory	8 Gigabyte
Interfaces	1 HDMI, 1 mini display port, 2 USB 3.0
Power supply	DC 19 V
Power consumption	65 W

2.2.3 PPK-GPS modules and RTK-GPS modules

Table 2. 3 Specifications of PPK-GPS modules

GNSS receivers	U-blox NEO-M8T
Processing unit	Intel Edison
Dimensions	45.5 * 27 * 9.2 mm
Weight	14 g
Antenna	Tallysman TW4721
Antenna dimensions	38 * 38 *14.3 mm
Antenna weight	50 g
Supply voltage	4.75 V to 5.5 V DC
Average power consumption	1 W
Operating temperature	-20° C to +65° C
Antenna DC bias	3.3 V
Internal storage	2 Gigabyte
Signals	GPS/QZSS L1, GLONASS G1, BeiDou B1
Channels	72

As mentioned in Sector 1.1.2, the positioning accuracy of standalone GPS mode, DGPS mode, and RTK-GPS mode is reported to be around 5 m, 1 m, and 2 cm, respectively. The RTK-GPS modules are usually used as a supplemental set outfit together with an IMU device when airborne LiDAR operations are under conduction. However, the commercial RTK-GPS module is too large in size and too heavy to be installed upon our small UAV platform. Besides, the cost of RTK-GPS service as well as the hardware is still a whopping price for individual users. Therefore, we introduced a small and lightweight PPK-GPS module in this study, which compromises of two identical GNSS receivers with the antenna and power supply module. One GNSS receiver remains stationary as a ground base station, whilst the other GNSS receiver is installed on the UAV-LiDAR topographic surveying system, shown in Fig.2.7, and works as a rover receiver within twenty kilometers away from the ground base station. The coordinates of the ground base station could be acquired by two ways. The most precise method is to measure the location's 3D coordinates (longitude, latitude, and altitude) using a RTK-GPS module prior to or after the experiment, which provides an absolute and accurate reference for PPK algorithm. The other one is a cost-efficient and easy to implement approach, which only utilizes the raw GNSS data of ground base station and average the location measurements for over thirty minutes up to two hours using least square method for example. The averaged 3D coordinates of the ground base station usually reaches up to a 0.5

m accuracy, but it only deviates the rover GNSS module's absolute location and the relative centimeter level accuracy is unaffected. This high precision GNSS positioning outfit utilizes an open source program package RTKLIB, which supports standard and precise positioning algorithm with GPS, GLONASS, Beidou, Galileo, and QZSS, using post processing analysis methods.

Table 2. 4. Specifications of RTK-GPS module

Receiver	Topcon GB-3
Dimensions	240 * 110 * 35 mm
Weight	600 g
Supply voltage	6 V to 28 V DC
Average power consumption	3.5 W
Operating temperature	-40° C to +75° C
Internal storage	2 Gigabyte
Signals	GPS, GLONASS
Channels	72
RTK accuracy	Horizontal: 10 mm
Antenna	PG-S1
Antenna dimensions	141.6 * 141.6 *54.2 mm
Antenna weight	615 g

RTK-GPS module was also used to validate the accuracy of the topographic map generated from the UAV-LiDAR topographic surveying system. RTK-GPS receiver working in a virtual reference station fashion usually provides a reliable and high precision 3D coordinates (longitude, latitude, and altitude) up to 2 cm, which has a wide range of applications in surveying as well as in the domain of autonomous driving. In this study we used a Topcon RTK-GPS receiver with a PG-S1 antenna (TOPCON Cor., Tokyo, Japan) to record reference 3D coordinates, shown in Fig.2.7, where part 1 marked in green box is the PPK-GPS receiver installed on the UAV platform and part 2 marked in red box is the RTK-GPS receiver for comparison. The specifications of the RTK-GPS receiver as well as antenna are listed in Table 2. 4.

Fig.2.7 RTK-GPS module and PPK-GPS module

2.3 Methodology

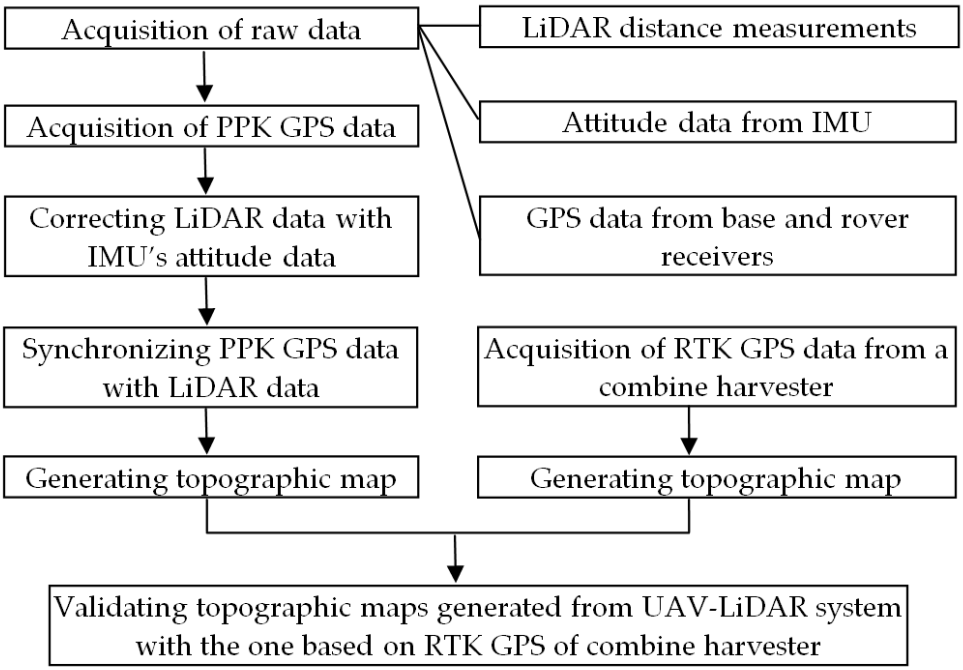

Fig.2. 8 Approach of generating topographic map

The overall approach of farmland topographic surveying by using the UAV-LiDAR system consists of six major steps: acquisition of raw data from LiDAR, MEMS IMU, and GNSS base as well as GNSS rover receivers; acquisition of PPK-GPS coordinates; correcting LiDAR distance measurements with attitude information from MEMS IMU; synchronizing PPK-GPS data with corrected LiDAR distance measurements; generating topographic map and validating the topographic map generated from UAV-LiDAR system using combine

harvester's RTK-GPS data, shown in Fig.2. 8. This study adopted World Geodetic System 1984, or WGS84, and map projection of UTM (Universal Transverse Mercator) Zone_54N with datum of WGS84, as the coordinate system in this paper, if not particularly indicated.

2.3.1 Field Site and Experiment Description

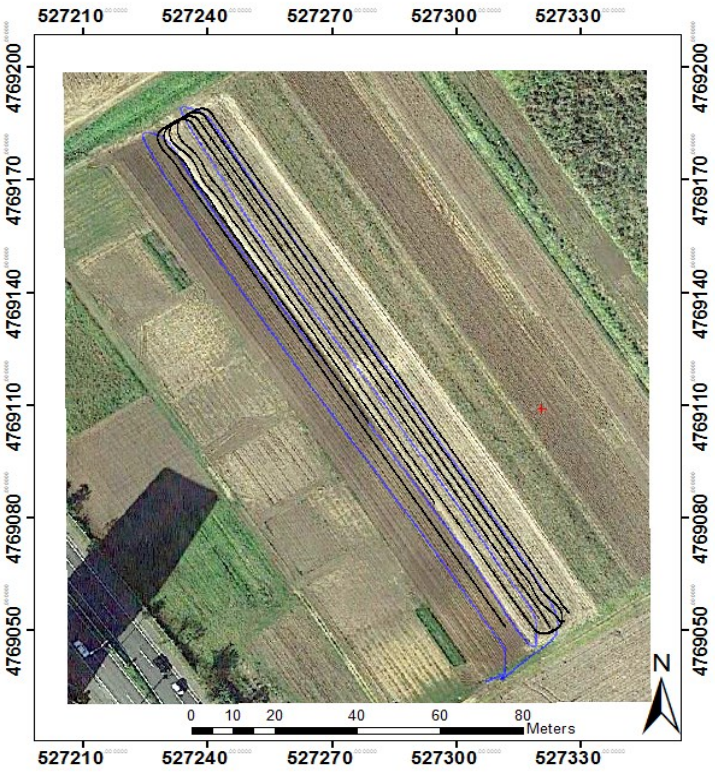

Fig.2. 9 A harvested wheat field under study

UAV-LiDAR system based topographic surveying experiment was established over a harvested wheat field located in Sapporo, Hokkaido, Japan, which accounts for about 0.4 hectare, shown in Fig.2. 9. High accuracy LiDAR device was fixed under the UAV platform pointing vertically downwards (shown in Fig.2. 2), and raw distance measurements data from the LiDAR device are ready to be corrected by using attitude data calculated from a tri-axial MEMS accelerometer, a tri-axial MEMS gyroscope, and a tri-axial MEMS magnetometer. Ground base station of the PPK-GPS module was measured and recorded by using the RTK-GPS module that were described in Sec. 2.2.3, whilst the rover receiver was attached on the top of the UAV platform. Autonomous flight was conducted on 10 August 2017, using flight paths that were designed beforehand at the speed of about 5 m/s and about 30 meters above ground level. Trajectory (two round trips) of the flight in blue color with the cross track interval of about 6 meters is shown in Fig.2. 9. As the output frequency of LiDAR distance

measurements and PPK-GPS data was synchronized at 10Hz, along track interval of each surveying point can be calculated as about 0.5 meter.

Besides, RTK-GPS data was also acquired by installing the Topcon GB-3 RTK-GPS receiver and the PG-S1 antenna on a combine harvester on 21 July 2017 when wheat harvesting was conducted in autonomous driving mode. The Topcon RTK-GPS module worked in a virtual reference station fashion, receiving correction information from GPS base station through network. The trajectory of the combine harvester based RTK-GPS was also shown in Fig.2. 9 in black color with the cross track interval of about 1.6 meters and along track interval of each surveying point of about 0.2 m.

2.3.2 Acquisition of UAV-LiDAR System's Attitude Information

The small UAV platform used in this study consists of six brushless DC motors, with three pairs of counter-rotating propellers which are fixed-pitch blades. These three pairs of counter-rotating propellers not only act as a propulsion system but also control and stabilize the UAV platform's attitude by changing the angular speed of each pair of motors, so that such movements like climbing, descending, turning direction, whirling, and even obstacle avoiding could be implemented. The rotational speed of each brushless motor is determined by the voltage imposed upon the motors, as Eq. (2.1).

$$n = \frac{U - IR}{C_e \Theta} \tag{2.1}$$

where:

n is the rotational speed of each motor;

U is the voltage imposed upon each motor;

I is the DC current through each motor;

R is the equivalent resistance of each motor's coil;

C_e is the constant variable of the motor ;

and Θ is the magnetic flux of each motor's coil.

In order to describe movements of the UAV platform, usually two reference systems are necessary. One is the earth fixed reference system using north, east, and down coordinates, which is tangent to the earth surface. The other one is a body fixed reference system, centered in the UAV platform's center of gravity. The absolute position (x, y, z) of the UAV is defined as linear to the body fixed reference system's origin, whilst the angular position of the UAV is usually described by means of the Euler angles defined as pitch (θ), roll (ϕ), and yaw (ψ). And thus, the transformation from the body reference system $[\,\theta\ \phi\ \psi]^{\mathrm{T}}$ to the earth reference system $[\mathrm{x\ y\ z}]^{\mathrm{T}}$ can be realized by using the rotation matrix R [53].

$$R = \begin{bmatrix} cos\theta cos\psi & cos\psi sin\theta sin\phi - cos\phi sin\psi & cos\phi cos\psi sin\theta + sin\phi sin\psi \\ cos\theta sin\psi & cos\phi cos\psi + sin\theta sin\phi sin\psi & cos\phi sin\theta sin\psi - cos\psi sin\phi \\ -sin\theta & cos\theta sin\phi & cos\theta cos\phi \end{bmatrix} \tag{2.2}$$

Therefore, acquisition of attitude information *(θ, ϕ, ψ)* of the UAV body is essential to control and stabilize the UAV, and also necessary for further analysis using attitude information to correct LiDAR distance measurements. 3D MEMS gyroscope is an inertial sensor for measuring orientation based on angular momentum principles, and the tri-axial angles $\left[\theta_{gyro}\ \phi_{gyro}\ \psi_{gyro}\right]^{\mathrm{T}}$ can be acquired by integral operation of angular speed of each axle, shown in Eq. (2.3). However, due to temperature variations of the MEMS gyroscope during operation, drift error of gyroscope and will accumulate along with time and accuracy as well as reliability of the attitude information calculated from a sole MEMS gyroscope would be compromised. On the other hand, 3D MEMS accelerometer can also be used to measure UAV's orientation based on the trigonometric functions of the acceleration of gravity components in each axial, shown in Eq. (2.4) and Eq. (2.5). But, the accelerometer is incapable of distinguishing the acceleration of gravity from external vibration, which means it is not suitable for attitude estimation application in cases of severe agitation such as aerial vehicles.

$$\left[\,\theta_{gyro}\ \phi_{gyro}\ \psi_{gyro}\right]^{T} = \int \left[\omega_x\ \omega_y\ \omega_z\right]^{T} dt \tag{2.3}$$

where $\theta_{gyro}, \phi_{gyro,}$ and ψ_{gyro} is the calculated pitch, roll, and yaw of UAV platform from gyroscope, respectively; whilst $\omega_{\mathrm{x}}, \omega_{\mathrm{y}},$ and ω_{z} is the raw rotation rates (degree/s) of each axial from the gyroscope, shown in

Fig.2. 10, at the sampling frequency of 50 Hz.

$$\theta_{acce} = -\arcsin\left(\frac{g_x}{\sqrt{g_x^2+g_y^2+g_z^2}}\right) \tag{2.4}$$

$$\phi_{acce} = arctan\left(\frac{g_y}{g_z}\right) \tag{2.5}$$

where θ_{acce} and ϕ_{acce} is the calculated pitch and roll of the UAV from accelerometer, respectively; whilst g_x, g_y, and g_z is the readings of acceleration components in each axial from the accelerometer, shown in Fig.2. 11, at the sampling frequency of 50 Hz.

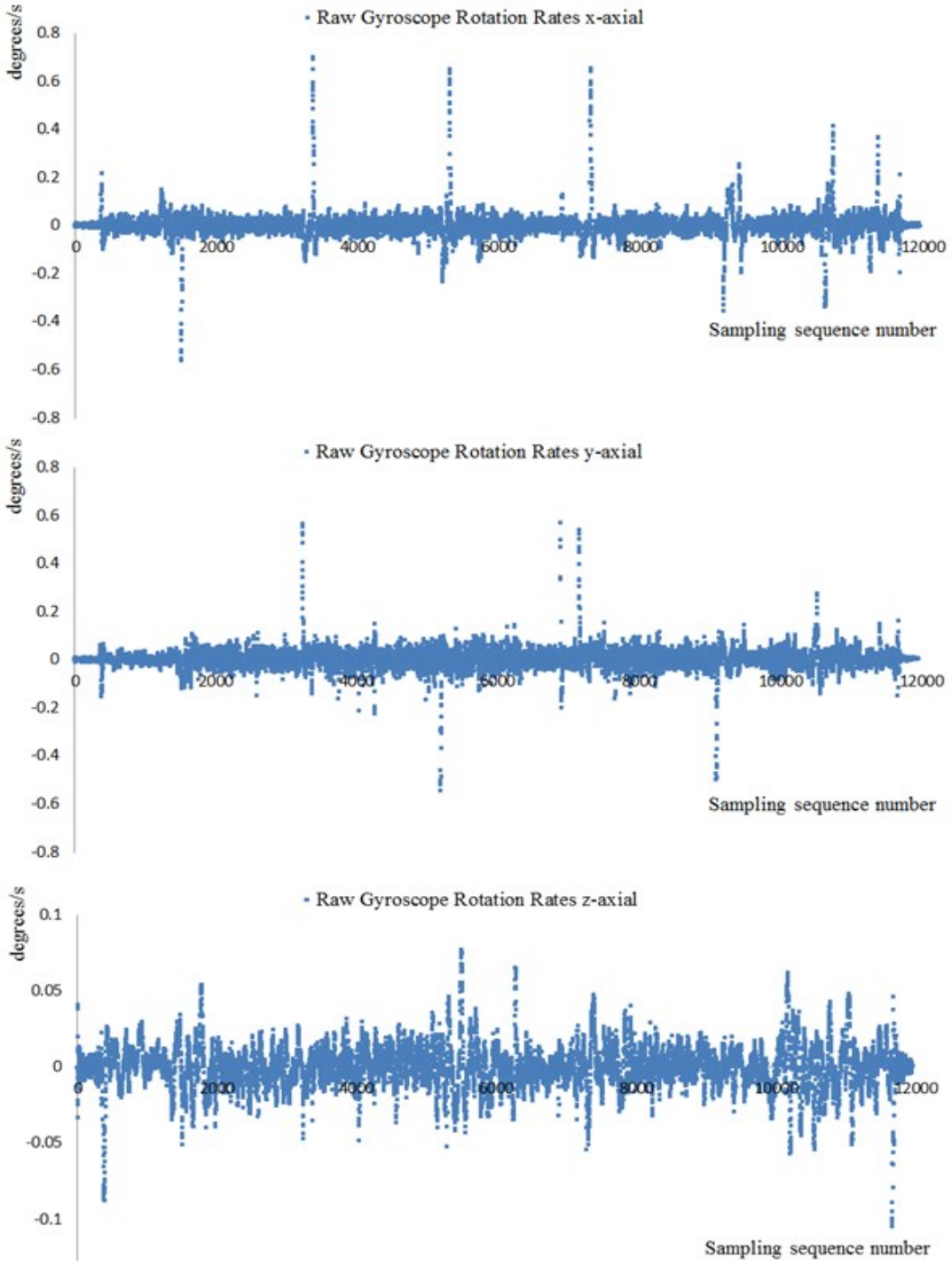

Fig.2. 10 Rotation rates of gyroscope

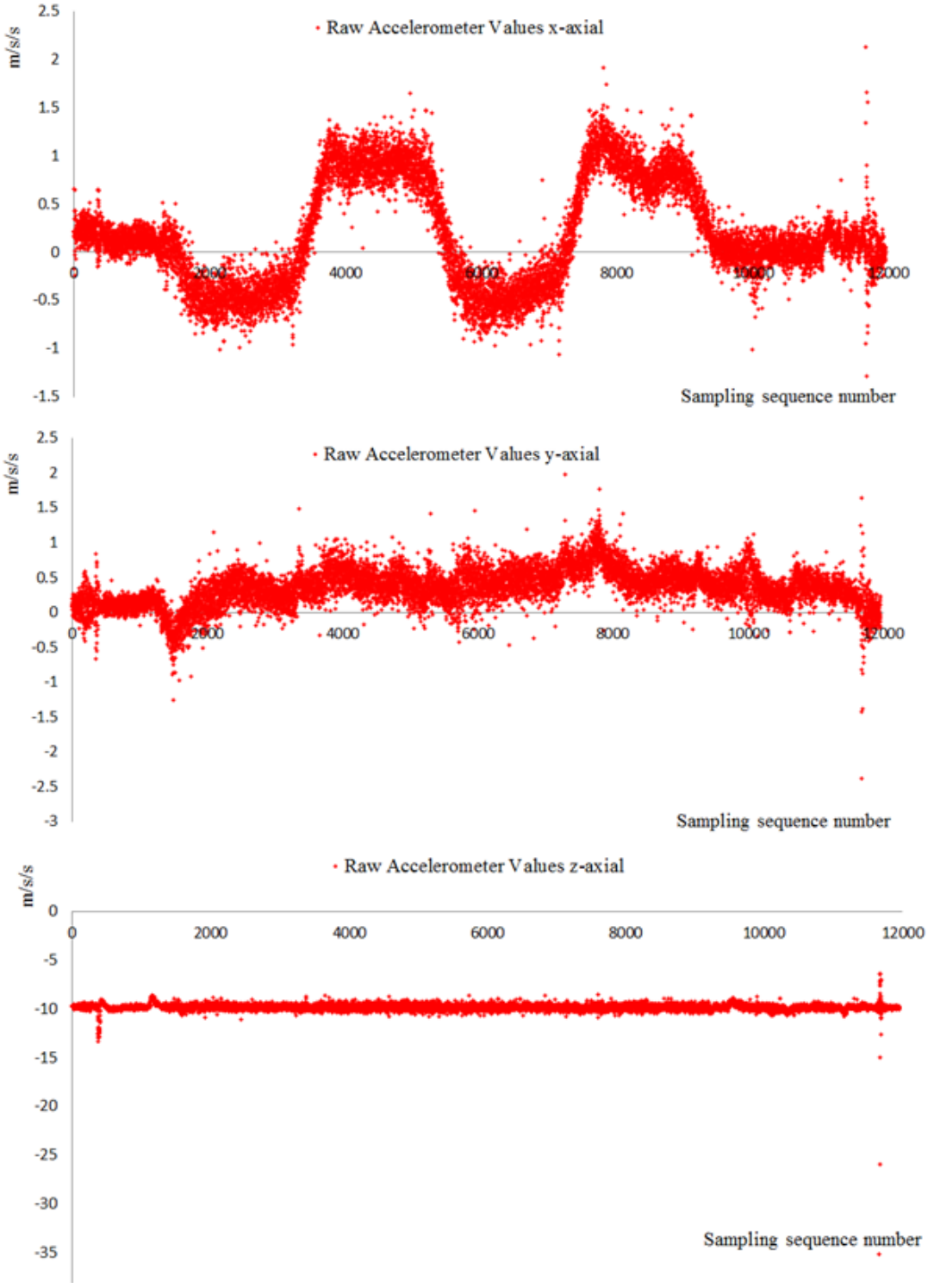

Fig.2. 11 Raw accelerometer values

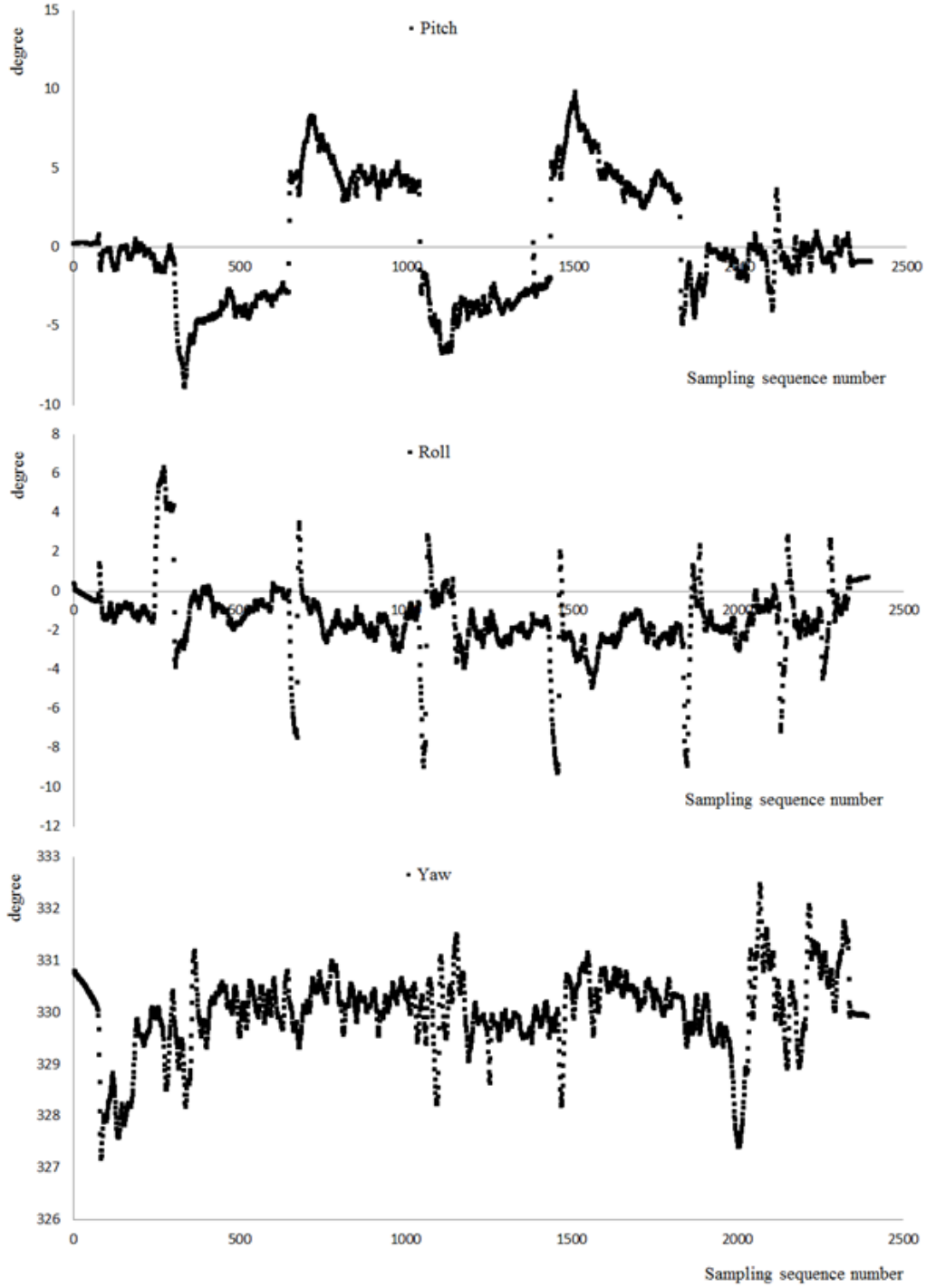

Fig.2. 12 Pitch, roll and yaw values of the UAV-LiDAR system

Moreover, magnetometer was also used as a complementary sensor for calculating the change of heading (yaw) of the UAV, in combination with the above mentioned gyroscope and accelerometer, as neither of them can be used solely for satisfactory attitude estimation in long time operations. There are more than one well-proved method for data fusion of gyroscope, accelerometer, and magnetometer in the domain of UAV attitude control, such as the explicit complementary filtering method, self-adaptive complementary filtering method,

gradient descent filtering method, Kalman filtering method as well as extended Kalman filtering method, and etc. In this study the UAV's flight controller utilizes an extended Kalman filter to fuse data from multiple sensors of accelerometer, gyroscope, and magnetometer for attitude estimation. The attitude estimation system is simplified as Fig.2. 13, whilst m_x, m_y, m_z, and ψ_{magn} is the magnetic intensity components in each axial and estimated yaw from magnetometer, respectively. In this way, attitude data of pitch, roll, and yaw values of the UAV-LiDAR system were acquired after the flight at the sampling frequency of 10 Hz, shown in Fig.2. 12. Attitude data of pitch and roll were used to correct LiDAR distance measurements for further analysis.

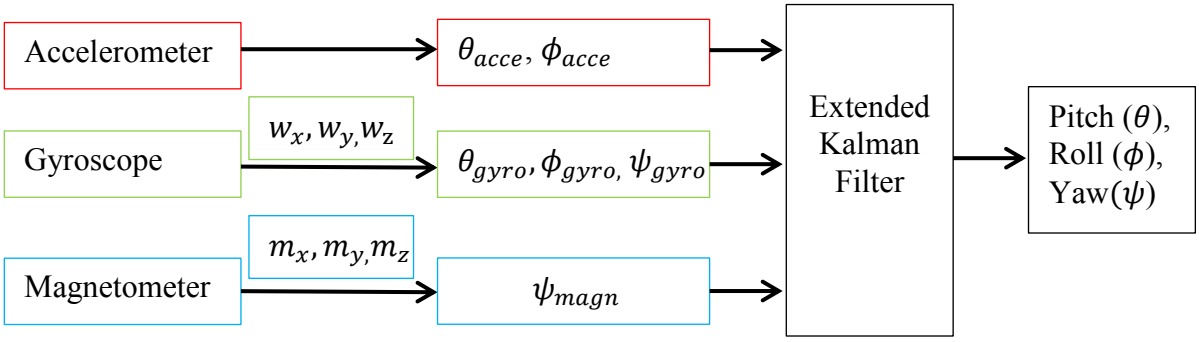

Fig.2. 13 Simplified attitude estimation system of the UAV

2.3.3 Synchronizing LiDAR Distance Measurements with PPK-GPS Data

Table 2. 5 PPK-GPS coordinates (in part)

Sample	Date	UTC	Latitude(degree)	Longitude(degree)	Altitude(m)
1	8/10/2017	01:04.2	43.0735617	141.3354461	14.078
2	8/10/2017	01:04.3	43.0735617	141.335446	14.078
3	8/10/2017	01:04.4	43.0735617	141.3354461	14.077
4	8/10/2017	01:04.5	43.0735617	141.3354461	14.077
5	8/10/2017	01:04.6	43.0735617	141.335446	14.079
…	…	…	…	…	…
4740	8/10/2017	08:58.1	43.0735336	141.3354268	14.263
4741	8/10/2017	08:58.2	43.0735336	141.3354268	14.265
4742	8/10/2017	08:58.3	43.0735336	141.3354268	14.261

PPK-GPS data were acquired by using an open source algorithm in RTKLIB software, after measuring absolute geo-spatial coordinates of ground base station as correction reference using a RTK-GPS module. The 3D coordinates was measured as (43.07355556 N, 141.3354386 E, 11.236 m). Considering the RTK-GPS module in the topographic map's validation experiment is installed on the top of the combine harvester's cabin, which is about 2.71 m above ground level, the altitude of the base station was rectified as 13.946 m by adding the RTK-GPS module's height of 2.71 m to the measured altitude 11.236 m. Thus, the PPK-GPS coordinates of the GNSS rover, which is attached to the UAV-LiDAR system, were calculated and listed in Table 2. 5. The number of samples of PPK-GPS measuring reached up to 4742 in total at the frequency of 10 Hz.

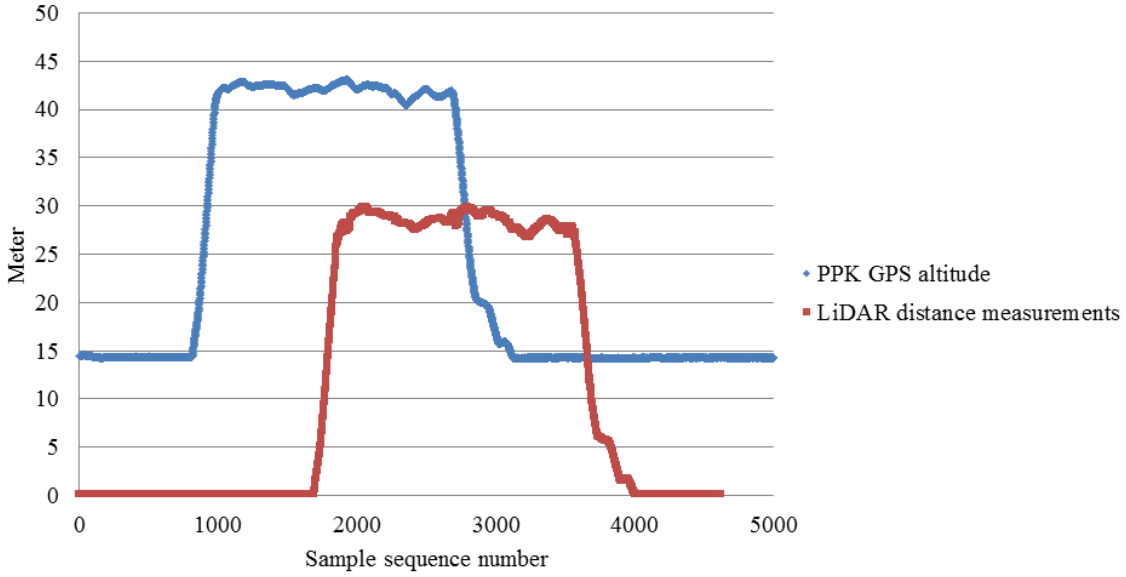

Fig.2. 14 Raw data of PPK-GPS altitudes and LiDAR distance measurements

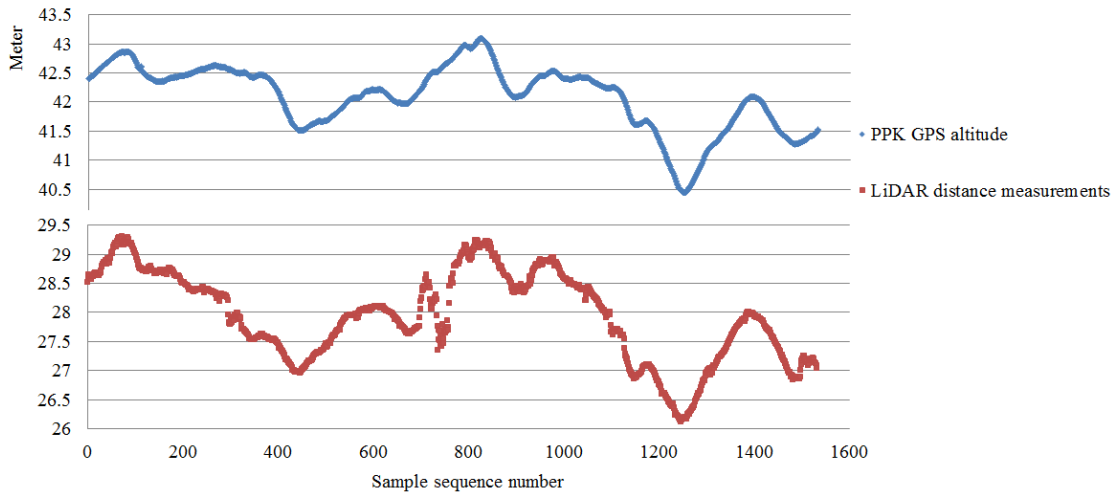

Fig.2. 15 Synchronized PPK-GPS altitudes and LiDAR distance measurements

As mentioned in Sec. 2.2.2, the LiDAR device used in this study measures distance at the frequency of 2000 Hz with the measuring resolution of 1 mm. Because the output frequency of PPK-GPS coordinates as well as the attitude data of the UAV-LiDAR system is fixed as 10 Hz, the LiDAR distance measurements cannot be directly corrected by using the attitude information, nor can it be directly aligned with the PPK-GPS coordinates. Besides, as the LiDAR distance measurement's output has no timestamp, it has to be synchronized with PPK-GPS data in the first place so that each LiDAR distance measurement could be tagged with timestamp, and then be aligned with the attitude data using timestamp and be further corrected by using the attitude data. In order to synchronize the 2000 Hz LiDAR distance measurements with the 10 Hz PPK-GPS coordinates as well as to improve measuring precision, a mean filter was applied to the LiDAR distance measurements so that the output was averaged from 2000 Hz to 10 Hz. The PPK-GPS altitude values and the averaged LiDAR distance measurements are shown in Fig.2. 14. Subsequently, taking LiDAR distance measurements and PPK-GPS altitude that are on the point of taking off as a benchmark, we synchronized two sets of height data so that each LiDAR distance measurement could be geo-coded and timestamped. The synchronized result of corrected LiDAR distance measurements with PPK-GPS altitude was shown in Fig.2. 15.

2.3.4 Correcting LiDAR Distance Measurements and Calculating Ground Elevation

As shown in Fig.2. 12, the attitude of the UAV-LiDAR system is apt to be changing all the time during each flight, due to inherent aerodynamic characteristics. The changing attitude of the UAV-LiDAR system impairs the accuracy of each LiDAR distance measurement, as the LiDAR device is rigidly fixed upon the UAV platform pointing downwards. Because each LiDAR distance measurement has already been geo-coded and timestamped by synchronizing with PPK-GPS data, we sued the timestamp information on the LiDAR distance measurements and attitude data of the UAV-LiDAR system to synchronize them together. Therefore, in order to eliminate such effects of continuously changing attitudes of the UAV-LiDAR system during the flight on the LiDAR distance measurements, synchronized attitude data of pitch and roll were utilized to correct the LiDAR distance measurements using the model expressed as Eq. (2.6). The corrected LiDAR distance measurements were shown in Fig.2. 16.

$$d_{corr} = d \times \cos\theta \times \cos\phi \tag{2.6}$$

where d_{corr}, d, θ, and ϕ indicates the corrected LiDAR distance measurements above ground level, the raw LiDAR distance measurement, and the attitude data of pitch and roll, respectively.

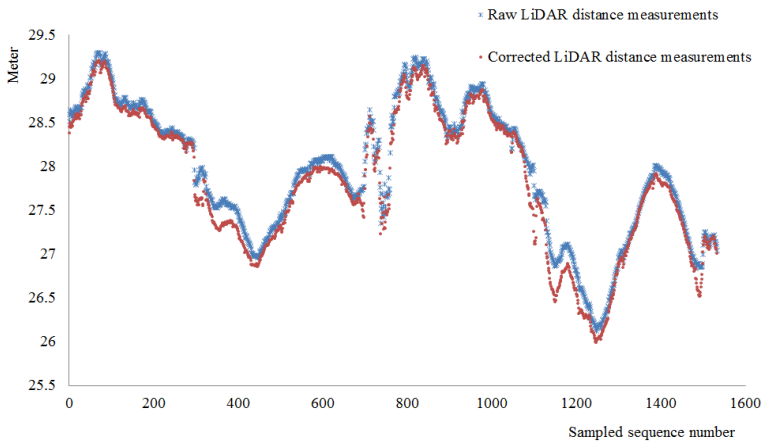

Fig.2. 16 Corrected LiDAR distance measurements

Based on the synchronized results of corrected LiDAR distance measurements with PPK-GPS 3D coordinates, ground elevation of each surveying point could be calculated using the model expressed as Eq. (2.7). We removed superfluous data during the process of taking off, turning round, and landing by visual inspection. And the total number of surveying points within the field under study amounted to 1135 in total, shown in Fig.2. 17.

$$e = h_{ppkgps} - h_{fix} - d_{corr} \tag{2.7}$$

where e, h_{ppkgps}, h_{fix}, and d_{corr} indicates the ground elevation of each surveying point, the PPK-GPS altitude, the height difference between PPK-GPS rover receiver's antenna and LiDAR's laser lens (0.36 m), and the corrected LiDAR distance measurement, respectively.

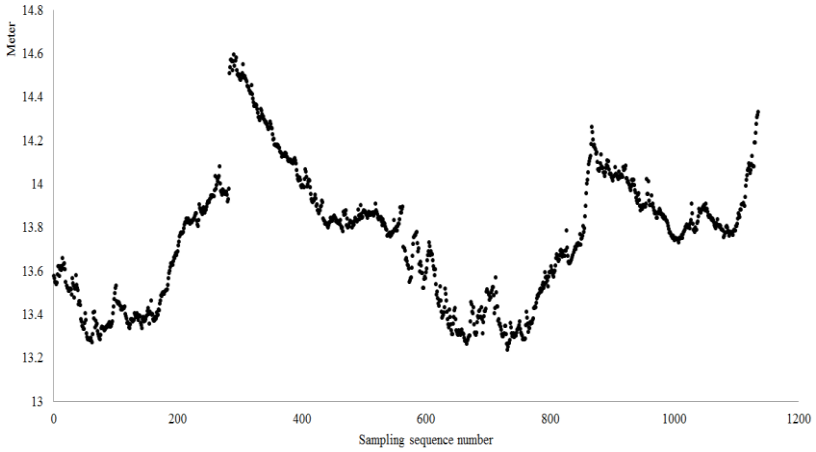

Fig.2. 17 Ground elevation of each surveying point

2.4 Result and Discussion

2.4.1 Accuracies of PPK-GPS Altitude and LiDAR Distance Measurements

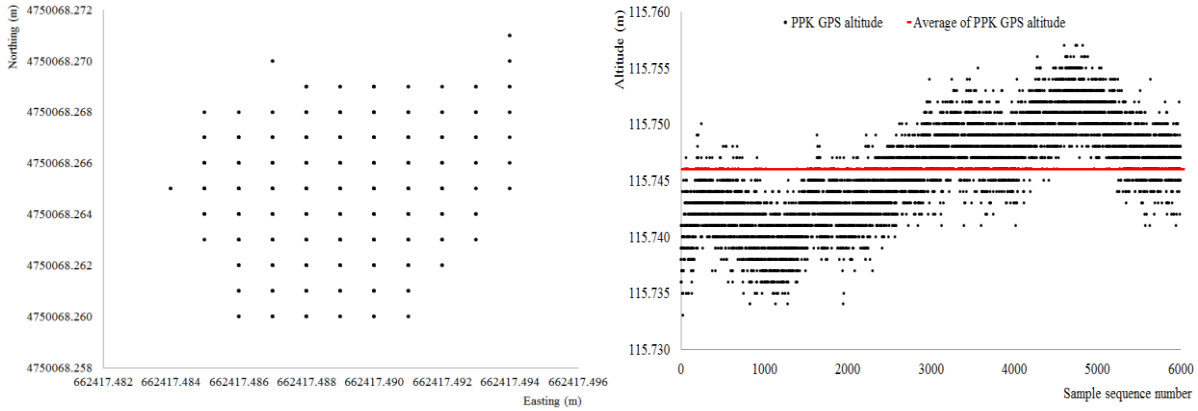

Fig.2. 18 Accuracy of PPK-GPS coordiantes

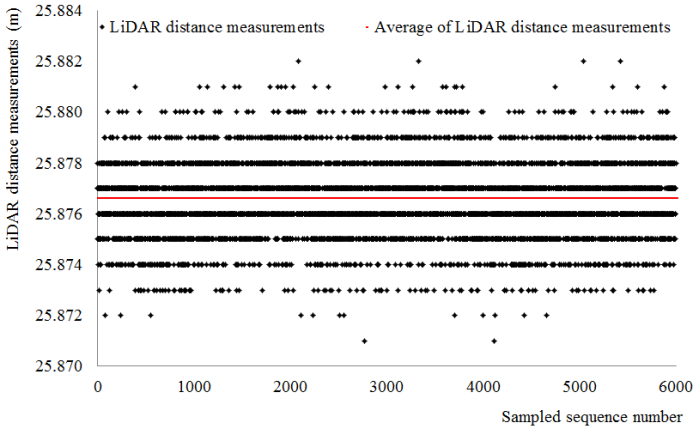

Fig.2. 19 Accuracy of LiDAR distance measurements

To validate the accuracies of PPK-GPS coordinates, we extracted 6000 sets of PPK-GPS data consecutively ten minutes before the UAV-LiDAR system took off when the PPK-GPS rover's antenna was hold stationary. The horizontal and vertical accuracy of PPK-GPS coordinates was shown in Fig.2. 18, from which we may conclude that the horizontal accuracy is as good as about 0.01 m (1cm), as most of the 6000 set of easting and northing coordinates fall within the range of about 0.01m. On the other hand, from Figure 8 we may understand that altitude measurements of PPK-GPS changed along with time, mainly due to adoption of different combinations of satellites over time. The altitude measurements varied from about 115.735 m to 115.755 m with vertical accuracy of about 0.02 m (2 cm). Besides, another 6000 sets of static LiDAR distance measurements were also acquired by pointing the LiDAR device at a wall about 25 m far away and holding it still for ten minutes, shown in Fig.2. 19. From Figure 9 we could conclude that LiDAR distance measurements remained

substantially constant over time, mostly ranging from 25.872 m - 25.882 m, and the measuring accuracy could be confirmed as within 0.01 m (1 cm). Thus, we may declare that the accuracy of this high accurate topographic surveying outfit surpasses the dominant handheld RTK-GPS based topographic surveying device.

2.4.2 Validating UAV-LiDAR Based Topographic Surveying Accuracy

Based on the calculated ground elevation of each surveying point, a map indicating spatial variations of within-field ground elevation was generated by using GIS (Geographic Information System) software ArcMap (ESRI Inc., Redlands, AB, Canada), shown in Fig.2. 20. From the graduated symbols representing different levels of ground elevation, we can visually understand the general high-north-low-south terrain of the field under study, with the ground elevations varying from 13.237 m to 14.594 m. From Fig.2. 20 we may also conclude that the area that is marked in green box has relatively low ground elevation, and the influx of irrigation water as well as snowmelt water or heavy rainfall is very likely to form puddles, which pose potential threaten to the crop growth and yield. In order to achieve uniform growth status of crops and improved yield, an east-west direction's land leveling operation could be suggested to effectively fill the puddles and remove the mounds.

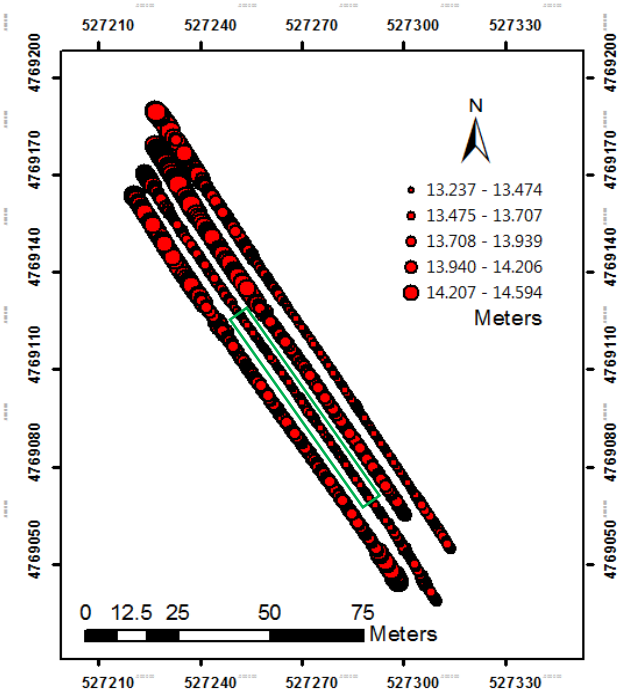

Fig.2. 20 Ground elevation of each surveying point showed in graduated symbols

A RTK-GPS module was installed on an autonomous combine harvester to acquire accurate 3D coordinates (easting, northing, and altitude) for validating the UAV-LiDAR system based topographic surveying method, as RTK-GPS positioning is a well-proved method of conducting field survey with reliable centimeter-level accuracy,. The combine harvester's working speed was set as 1 m/s, and as the RTK-GPS positioning frequency was set as 5 Hz, the along track interval of each surveying point could be calculated as about 0.2 m. Besides, as the cross track interval was set as about 1.6 m, the spatial resolution of RTK-GPS surveying points could be determined as about 1.6 m* 0.2 m. The amount of RTK-GPS surveying points were 7330 in total, with several missing points due to GPS failure, shown in Fig.2. 21 as black dots. Totally 35 pairs of validating samples that were distributed all over the field under study were collected according to the overlapping trajectories of the UAV-LiDAR system and the combine harvester, shown in Fig.2. 21. The red dots, the black dots, and the green dots represent each surveying point's location acquired by using UAV-LiDAR topographic surveying system, combine harvester based RTK-GPS module, and validating samples, respectively.

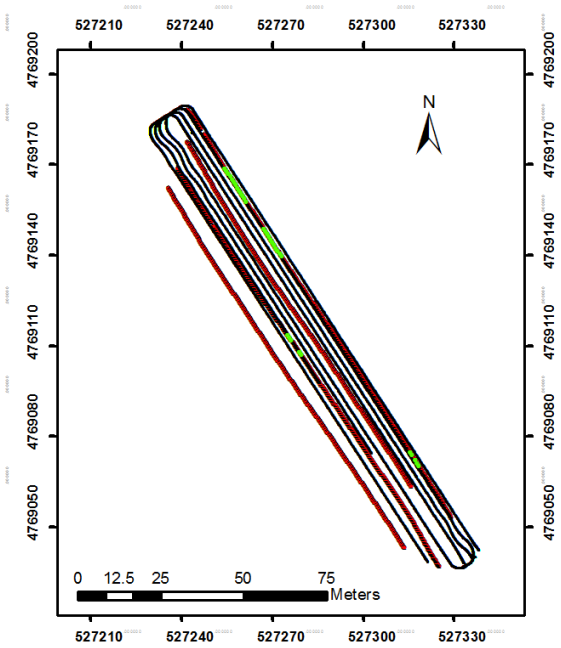

Fig.2. 21 Distribution of validating samples

These 35 pairs of validating samples consist of 35 RTK-GPS surveying points and their counterparts of UAV-LiDAR system's surveying points that overlapped (or fell within the very near neighborhood) each other. The ground elevation values' differences among each

pair of validating samples were shown in Fig.2. 22, from which we can conclude that the ground elevation values of UAV-LiDAR system based topographic surveying points correlate well with the ones of RTK-GPS's altitude values. We can also see that the ground elevation values of RTK-GPS are smoother than the ones of the UAV-LIDAR system, as the combine harvester that carries the RTK-GPS module follows the field terrain closely and all residual straws or standing plants would be crushed below the chassis due to heavy dead weight of the vehicle. On the other hand, as explained in Sec. 2.2.2 the UAV-LiDAR system measures the field terrain in an area-scanning fashion (about 6 cm * 2 cm when flying at the height of 30 m above ground level) rather than a point-measuring fashion like the RTK-GPS module installed on the combine harvester due to laser beam divergence. Within the scanning area there might be the existence of residual straws or standing plants over the harvested wheat field, which poses as a potential outlier in the ground elevation survey.

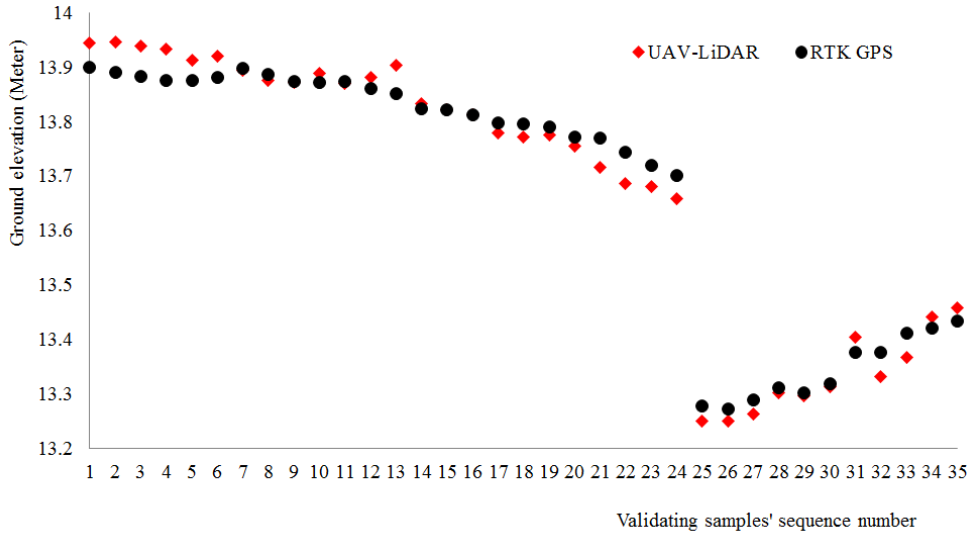

Fig.2. 22 Differences among validating samples' ground elevation

Finally, according to Eq. (2. 8) the Root Mean Square Error (RMSE) between these 35 pairs of ground elevation data of RTK-GPS and UAV-LiDAR system was calculated as 0.035 m (3.5 cm). Considering that the ground elevation of the field under study varies from 13.237 m to 14.594 m according to the topographic survey using the UAV-LiDAR system, the value of the RMSE is acceptable in comparison with the elevation difference of 1.357 m, which indicates that the UAV-LiDAR topographic surveying system is very precise.

$$RMSE_{UAV-RTK} = \sqrt{\frac{\sum_{i=1}^{35}(e_{UAVi}-e_{RTKi})^2}{35}} \quad (2.8)$$

where e_{UAVi} and e_{RTKi} indicates the ground elevation data of the UAV-LiDAR system and the RTK-GPS data, respectively.

2.4.3 Visual Validation of UAV-LiDAR System Based Topographic Survey

An experiment was also established over a harvested sugarcane farmland located in Mackay, Queensland, Australia (around 21.259794°S–21.263142°S and 149.091325°E–149.094109°E), shown in Fig.2. 23, which accounts for about 3 hectares. Autonomous flight using the same UAV-LiDAR topographic surveying outfit was conducted in December 7 2016 at the ground speed of 5 m/s and altitude about 30 meters above ground level. Trajectory of the flight also was shown in Fig.2. 23 as red dots, and the track intervals were set every 20 m. In order to confirm the UAV-LiDAR system's working capability, several bumps and hollows (about 30 cm in depth and 1.5 m in length) were artificially built inside the field by using a plough attached to a tractor, shown in Fig.2. 24. From Fig.2. 25 we can clearly see that two hollows under the flight trajectory of the UAV-LiDAR system were precisely spotted, showed in black circle and rectangle, respectively. And we can come to the conclusion that the UAV-LiDAR topographic surveying system has good capability of conducting a farmland topographic survey for precision land leveling.

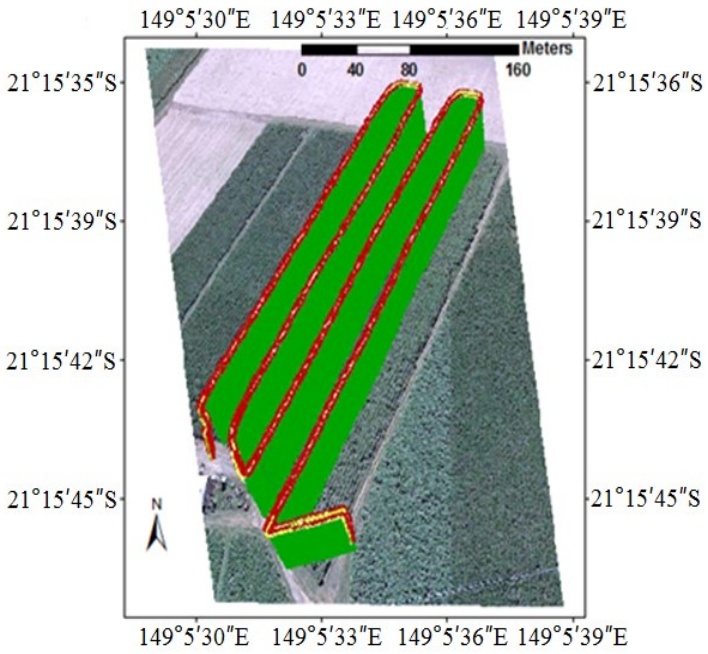

Fig.2. 23 Field site of experiment for visual validation

Fig.2. 24 Building bumps and hollows using a plough

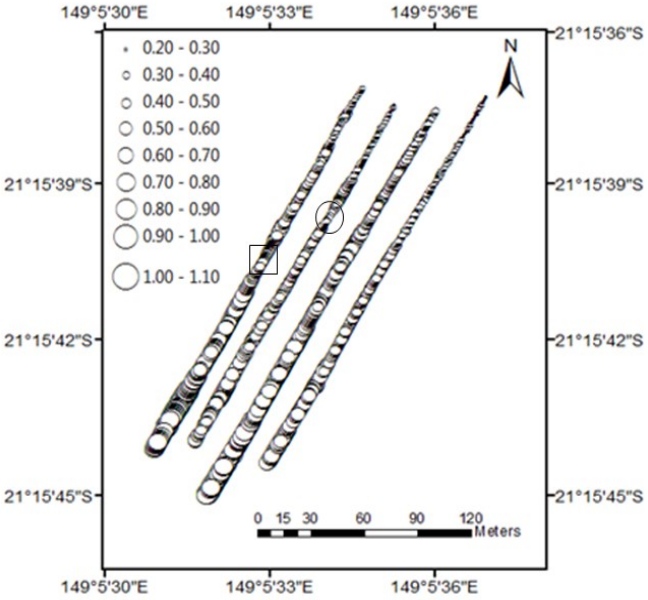

Fig.2. 25 Visual validation of spatial variations of within-field ground elevation

2.5 Conclusions

Evenness of ground surface of a farmland is paramount, as optimal crop production requires adequate soil moisture during the growing season; however, too much stagnant water can lead to yield losses from disease and root problems. Precision land levelling deals with this kind of issue by cutting soils from where the ground elevation is relatively high and releasing soils over where the ground elevation is relatively low, in order to form a uniformly flat ground surface. However, topographic survey is usually indispensable to either the laser-assisted land leveling or the GNSS based land leveling operation. And topographic survey using conventional equipment is proven to be extremely time-consuming to take enough

samples manually, not even to say that the conduction itself is highly dependent on professionals. In this study, we developed an innovative topographic surveying method by integrating LiDAR distance measurements with PPK-GPS coordinates, using a low-altitude UAV as a platform.

The accuracy of PPK-GPS altitude as well as the LiDAR distance measurements was validated as 2 cm and 1 cm, respectively, which showed good capability of conducting topographic surveying operations. We conducted a topographic surveying experiment in a harvested wheat field using the UAV-LiDAR system, and the total number of surveying points within the wheat field under study amounted to 1135 in total, when superfluous data were removed during the process of taking off, turning round, and landing by visual inspection. Ground elevation values of these topographic surveying points were calculated by using the synchronized results of corrected LiDAR distance measurements with PPK-GPS 3D coordinates. Based on the calculated ground elevation of each surveying point, a map indicating spatial variations of within-field ground elevation was generated by using GIS software ArcMap. From the graduated symbols representing different levels of ground elevation, we can understand the general high-north-low-south terrain of the field under study. We may also visualize several puddles inside the wheat field, and accordingly an east-west direction's land leveling operation was suggested to effectively fill the puddles and remove the mounds of the field.

Furthermore, in order to validate the accuracy of the ground elevation data of the UAV-LiDAR topographic surveying system, a RTK-GPS module was utilized to acquire topographic surveying data on the same field, as RTK-GPS positioning is a well-proved method with reliable centimeter-level accuracy. Totally 35 pairs of validating samples that were randomly distributed all over the field under study were collected according to the overlapping trajectories of the UAV-LiDAR system and the RTK-GPS module. The RMSE between ground elevation data of RTK-GPS and UAV-LiDAR system was calculated as 0.035 m. In consideration that the ground elevation of the field under study varies in the range of 1.357 m according to the topographic survey data of the UAV-LiDAR system, the RMSE of 0.035 m is considered as highly accurate and acceptable. Besides, an experiment in a harvested sugarcane field was also conducted for visual validation of the working capacity of the developed UAV-LiDAR topographic surveying system. Bumps and hollows in the middle of the field artificially made by using a plough could be clearly spotted by visual

interpretation, which practically proved the applicability of this UAV-LiDAR system for topographic mapping operations.

In short, the proposed UAV-LiDAR system based approach of conducting topographic survey could practically provide ground elevation reference for laser-assisted land leveler to preset the height of the laser transmitter, and also could be used to produce cut/fill ratio map for GNSS based land leveler. And the topographic surveying system is of high precision, efficient in time and cost, and simple in structure, which is also highly flexible in designing and executing autonomous flight for each specific farmland.

Chapter 3 Integrating Aerial Photogrammetric DSM with UAV-LiDAR System's Topographic Surveying Data

3.1 Introduction

Precision land levelling deals with the issues of unevenness of the farmland ground surface, and neither the laser-assisted land leveler nor the RTK-GPS guided land leveler can deliver the optimal performance unless an accurate topographic map of the field is available prior to land leveling operation. Generally, a topographic map is generated by interpolating individual surveying points that are uniformly distributed around the area of interest. Total station and portable RTK-GPS module are often used in common topographic surveying as the conventional and primary tools, whilst terrestrial laser scanner, airborne laser scanner, and aerial photogrammetry devices are recently utilized for different kinds of topographic applications like construction site, urban ecology modeling, forest monitoring, and etc. However, the time-consuming conventional topographic surveying methods as well as the low vertical accuracy of the new fashioned topographic surveying techniques are not suitable to generate precise topographic maps for farmland's precision land leveling operation.

Besides, the overall accuracy of topographic maps not only depends on the accuracy of each surveying measurements, but is also influenced by the spatial resolution as well as the spatial distribution of the surveying points to a great extent. As it is well known that the interpolating results are apt to be less reliable as the surveying points' spatial resolution increases. Basically, there are no other alternatives to improve the overall accuracy of an interpolated topographic map but to increase the total number as well as the sampling spatial resolution of the measured points, which is usually time-consuming or impossible to perform in practice. On the other hand, aerial photogrammetric DSM is featured with great spatial resolution, however, needs a large number of GCPs uniformly spreading around the area of interest for guaranteeing the accuracy of the resulting surface elevation values.

Aerial photogrammetric DSM possesses the advantages of good spatial resolution and large coverage, which has been utilized for many years in urban ecological study, forest monitoring, and etc. But the processing of aerial images for generating photogrammetric DSM usually needs strict camera calibration and well distributed ground control points (GCPs). GCP in photogrammetry or computer vision domain refers to such features that are

easily recognizable and distinguishable in both the reality world and in the images during post-processing, such like crossroads, bridges, field corners, and etc. The geospatial accuracy as well as the ground elevation accuracy of the photogrammetric DSM is in high accordance with the GCPs' condition.

Furthermore, in recent years many commercial photogrammetric processing software products emerged that are capable of generating point clouds, 3D models, and DSMs from digital images based on computer vision techniques, which could find a wide range of applications in 3D reconstruction and visualization, urban ecological surveying and mapping, agricultural remote sensing and mapping, and etc. Agisoft PhotoScan (Agisoft LLC, St. Petersburg, Russia) is one of the most advanced photogrammetric processing software suitable for low-altitude UAV remote sensing. The Agisoft PhotoScan software utilizes the latest multi-view 3D reconstruction theory for extracting key-points from each individual aerial image, matching the identical key-points from multiple images, automatically estimating camera parameters according to the image matching result, and finally stitching multiple images into an ortho-mosaicked one.

Therefore, we came up with a solution of integrating the UAV-LiDAR system based topographic surveying data, as described in Chapter 2, with the low-altitude UAV based photogrammetric DSM for generating a precise topographic map. Because the topographic surveying data using the UAV-LiDAR system is highly accurate but lacks adequate spatial resolution when interpolated for generating topographic maps, whist the aerial photogrammetric DSM is featured with great spatial resolution and rich details but cannot guarantee the absolute accuracy of the pixels values (surface elevation values) that are away from GCPs. In this chapter, we are to discuss the methodology of integrating these two different sources of topographic data for generating a topographic map in an efficient and accurate manner. This new topographic surveying method does not require the arrangement of plentiful artificial GCPs for constraining the accuracy of each pixel's ground elevation value of the resulting aerial photogrammetric DSM, and does not need extra UAV-LiDAR flights for acquiring a great deal of samples by shortening the cross-track intervals.

3.2 Methodology

In geo-statistics, interpolation is a method of approximating and assigning new data for locations where no samples have been taken within the range of a discrete set of known data

points, as it is in practice always impossible to take samples at every location in an area of interest due to restrictions of equipment or limited sampling time. Besides, interpolation is commonly used to create continuous surface from data of discrete points in GIS domain for better understanding of the overall trend and spatial variations, because real world phenomenon are always continuous in nature such as ground elevation, depths of river, temperatures, precipitations, and so on.

Interpolation results can vary significantly depending on different interpolating models, since intermediate values for locations where no measurements are available are inferred by a process based on different mathematical calculations. Piecewise constant interpolation is the simplest interpolation model, which assigns the nearest known data value for the non-given points. Nearest-neighbor algorithm is one of the most commonly used piecewise constant interpolation method, which does not consider the values of neighboring points and only selects the value of the nearest point for each interpolating location. This algorithm is very easy to implement, and is usually used in digital imaging applications to select color values for a textured surface. Besides, there are other interpolating models such as linear interpolation, polynomial interpolation, spline interpolation, and Gaussian process regression which is also known as Kriging, and etc. Each of the interpolating model suits specific needs when used for building continuous maps. For example, Kriging interpolation originates from geological mineral concentration analysis, whilst inverse distance weighting (IDW) interpolation is best suitable for demographical surveys.

There are various interpolation methods available nowadays, which could be divided into two categories in regard of forms of digital representation. One is based on regular rectangle grids, using such interpolating algorithms like IDW, Kriging, natural neighbor, and etc., to calculate and assign values for non-sampled grids according to the neighboring grid values. The topographic map generated from the regular rectangle grid method is often referred to as a raster map. The other one is based on triangulation method, and triangulated irregular network (TIN) is a most popular representation of a continuous surface consisting entirely of triangular facets by linking triplets of nodes and maintaining pointers from each triangle to its three neighbors [54], shown in Fig.3. 1.

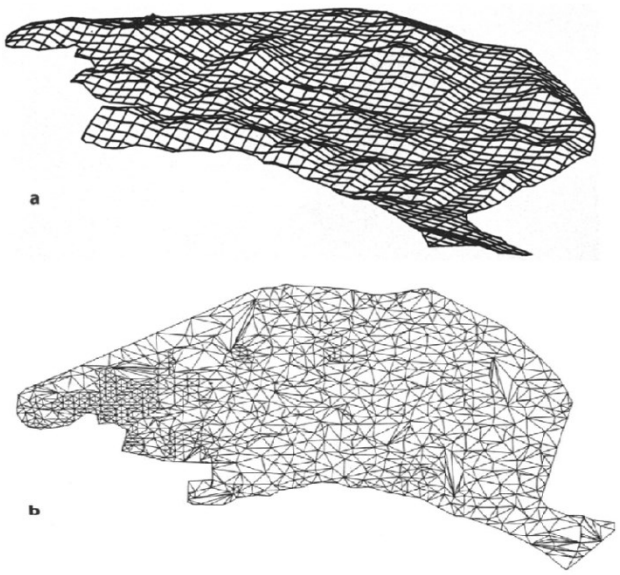

Fig.3. 1 (a) grid and (b) TIN based topographic modeling (Yih-ping Huang)

Hence, in this study we took advantage of 1135 ground elevation data, which were sampled at the spatial interval of about 6 m * 0.5 m using the UAV-LiDAR system we developed and mentioned in Chapter 2, for generating and assessing continuous topographic maps out of different interpolation methods in ArcMap software. Another 3889 ground elevation data were also acquired over a different farmland using the same outfit at the spatial resolution of about 20 m * 0.5 m for experimental validation.

3.2.1 Interpolating Topographic Surveying Data

TIN interpolation method is suitable for modeling natural complicated terrains due to the efficiency in data storage and capability to accommodate irregularly distributed elevation points according to actual terrain features in GIS applications, as the roughness of the terrain is always neither constant nor periodic but continuously changes from one place to another. TIN is a vector-based model by triangulating a set of points, which are featured with 3D attributes, to form a network of triangles of irregular size and shape. Among a number of ways for the construction of a TIN model from a given set of irregularly distributed spatial data, Delaunay triangulation is most widely used due to non-overlapping advantages and local equiangularity [55]. Most of TIN models use indirect interpolation principles to estimate z-values for non-measured locations after completing construction of triangles network based on triangular linear interpolating algorithm. TIN's triangular linear interpolation process begins with determining the triangular to which the interpolation point

belongs; then calculating the parameters of a, b, and c for plane equations of each triangular using 3D coordinates of three vertices (points), expressed as Eq. (3.1); and finally the elevation data of every interpolation points within the triangular could be acquired according to Eq. (3.2).

$$\begin{bmatrix} z_1 \\ z_2 \\ z_3 \end{bmatrix} = \begin{bmatrix} 1, x_1, y_1 \\ 1, x_2, y_2 \\ 1, x_3, y_3 \end{bmatrix} \begin{bmatrix} a \\ b \\ c \end{bmatrix} \tag{3.1}$$

$$z = a + bx + cy \tag{3.2}$$

where a, b, and c is the parameter for determining plane equation, respectively; whilst x_i, y_i, and z_i (i=1, 2, and 3) is the 3D coordinate (easting, northing, and elevation) of each vertice of the triangular, respectively; and x, y, and z is the 3D coordinates of each interpolation point, respectively.

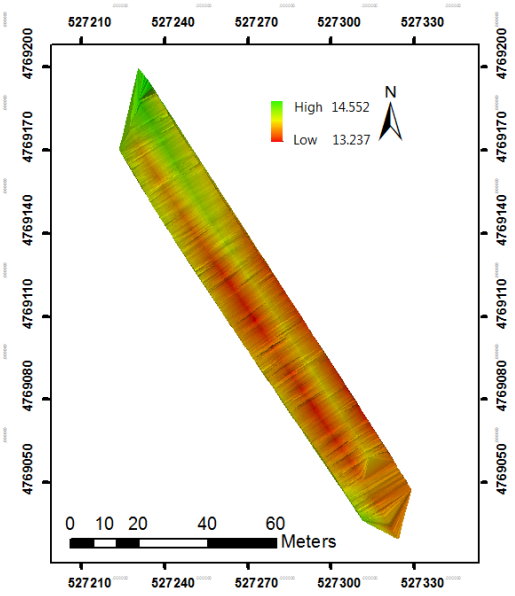

Fig.3. 2 TIN model of the field under study

In this study, we constructed a topographic map to represent the ground elevation features of the field under study in ArcMap software using TIN model, shown in Fig.3. 2. From the map we can see clearly that the field has a high-north-low-south trend in elevation varying from 13.237 m to 14.552 m; besides, we can also visualize a distinguishing ridge (shown in green and yellow color in the map in south-north direction) as well as a line of ditch (shown in red color in south-north direction) within the field. According to field survey

we confirmed that the ditch in south-north direction is around the border of two adjacent fields with relatively low ground elevation.

IDW model is referred to as a deterministic method for multivariate interpolation, which assigns a weighted average value of serval neighboring measured points (marked in red color in Fig.3. 3) to the unknown points (marked in yellow color in Fig.3. 3) using an inverse distance weighted technique. This method assumes that the influence of the measured point's z–value decreases on the interpolation point's z–value over the increasing distance from the measured points to the interpolation point, which finds good application in, for example, retail site analysis on the consumer purchasing power [56],[57].

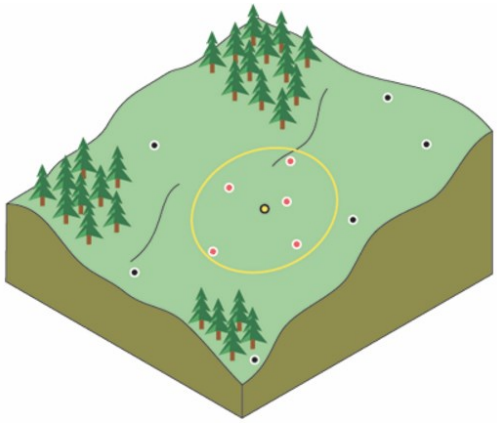

Fig.3. 3 Illustration of IDW method (by Esri)

There are several means of including neighboring measured points for calculating the z–value of each interpolation point by directly specifying the number of measured points to use, by specifying a certain radius and measured points within the radius will all be included, or by using a polyline dataset as barriers. Furthermore, the influence of each included measured point would also be controlled by changing the power parameter of the mathematical model expressed as Eq. (3.3), Eq. (3.4), and Eq. (3.5). The default power value is 2, and by defining a higher power value the nearby points will have more influence on the z–value of the interpolation point, resulting in a less smooth but more detailed surface; whilst by defining a lower power value, on the other hand, more influence will be given to surrounding points far away from the interpolation point, resulting in a smoother but less detailed surface. In this study, we adopted the default power value and specified the number of measured points as 12 in the variable search radius fashion using ArcMap software. The interpolation result was shown in Fig.3. 4, from which we can also see a high-north-low-south ground elevation trend

of this field under study; besides, we can see more clearly that a ditch (in red color) of south-north direction is very distinguishing when compared with the TIN model.

$$w_i = \frac{{d_i}^{-p}}{\sum_{i=1}^{n_{idw}} {d_i}^{-p}} \tag{3.3}$$

$$d_i = \sqrt{(x - x_i)^2 + (y - y_i)^2} \tag{3.4}$$

$$\hat{z}(x, y) = \sum_{i=1}^{n_{idw}} w_i z(x_i, y_i) \tag{3.5}$$

where w_i, d_i, p, and n_{idw}, is the weighting factor of each measured points, distance of each measured point to the interpolation point, power parameter (using default value of 2 in this study), and the number of measured points included in the IDW model (setting as 12 in this study), respectively; whilst (x, y) and (x_i, y_i) is the coordinate of easting and northing of the interpolation point and each measured point, respectively; $\hat{z}(x, y)$ and $z(x_i, y_i)$ is the estimated ground elevation of the interpolation point and each measured point's ground elevation, respectively.

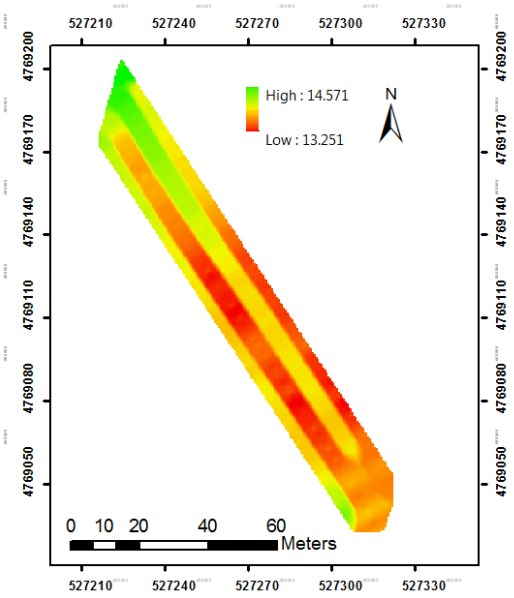

Fig.3. 4 Interpolation result using IDW method

Spline model interpolates the measured points for a smooth raster surface using a mathematical 2D minimum curvature spline technique that minimizes the total curvature of the surface. In the simple mathematical form, spline is continuous and has a continuous first derivative as well as a continuous second derivative. When spline model is used for

interpolation, the resulting smooth surface passes exactly through all of the measured points by fitting a mathematical function to a specified number of nearest measured points [58],[59], according to Eq. (3.6). The spline interpolating model is best for representing gradually changing surfaces including pollution concentrations, ground elevations, and etc. In this study we created a topographic map out of the 1135 UAV-LiDAR topographic surveying data described in Chapter 2, using the spline interpolating model in ArcMap software, shown in Fig.3. 5. From the resulting map we can see the general high-ends-low-middle trend of the field under study with the variation of ground elevation from 10.933 m to 16.489 m. Several locations with high elevation (in green color) were also easily spotted inside the field from this spline method based topographic map, which were not visible in the TIN model or the IDW method based map, as the smooth surface passes exactly through the measured points instead of estimating z – values for all of the points in the map.

$$\hat{z}(x,y) = T(x,y) + \sum_{i=1}^{n_{spl}} c_i R(d_i) \tag{3.6}$$

$$T(x,y) = s_1 + s_2 x + s_3 y \tag{3.7}$$

$$R(d_i) = \frac{1}{2\pi}\left\{\frac{{d_i}^2}{4}\left[ln\left(\frac{d_i}{2\tau}\right) + c - 1\right] + \tau^2\left[K_o\left(\frac{d_i}{\tau}\right) + c + ln\left(\frac{d_i}{2\pi}\right)\right]\right\} \tag{3.8}$$

where $\hat{z}(x,y)$ is the estimated ground elevation of the interpolation point; $T(x,y)$ is regularized algorithm's coefficient determined by Eq. (3.7); $R(d_i)$ is the regularized algorithm's coefficient determined by Eq. (3.8); n_{spl} is number of measured points that are included in the spline interpolation model (using the default value of 12 in this study); c_i is the coefficient determined by the solution of a set of linear equations for each measured points; d_i is the distance from each measured point to the interpolation point; $s_1, s_2,$ and s_3 is also the coefficient determined by the solution of a set of linear equations for each measured points; τ is the weight parameter (using the default value of 0.1 in this study); c is a constant of 0.577215; K_o is the modified Bessel function; and (x, y) is the easting and northing coordinate of each interpolation points, respectively.

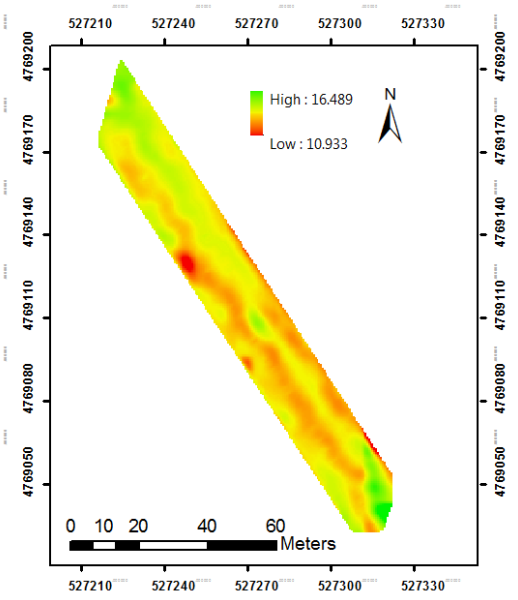

Fig.3. 5 Interpolation result using spline method

Natural neighbor interpolation model is very similar to the IDW model, except that it determines weight parameter based on proportionate areas instead of the inversed distances, shown in Fig.3. 6, where the red star mark represents the interpolation point and the black dots represent the surrounding measured points. The weight parameter for each surrounding measured point is calculated according to the proportion of overlapped areas between each measured point's polygon and the interpolation point's polygon, and the polygons are generated using Voronoi diagram [60]. The natural neighbor model only uses the closest subset of the measured points that surround the interpolation point. Same with the spline interpolation model, the resulting surface passes exactly through each measured point [61]. We created a topographic map using the natural neighbor interpolation model in ArcMap software, shown in Fig.3. 7. From the resulting map we can also understand the general high-north-low-south terrain of the field under study, with the variation of ground elevation from 13.253 m to 14.560 m. The ditch over the border of two adjacent fields was clearly distinguished and shown in red color, whilst a short ridge inside the field was shown in yellow color.

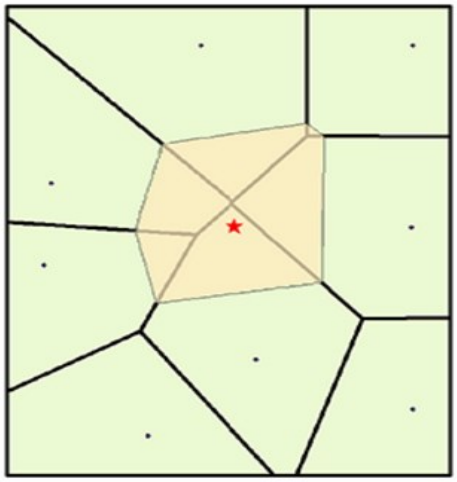

Fig.3. 6 Illustration of natural neighbor method (by Esri)

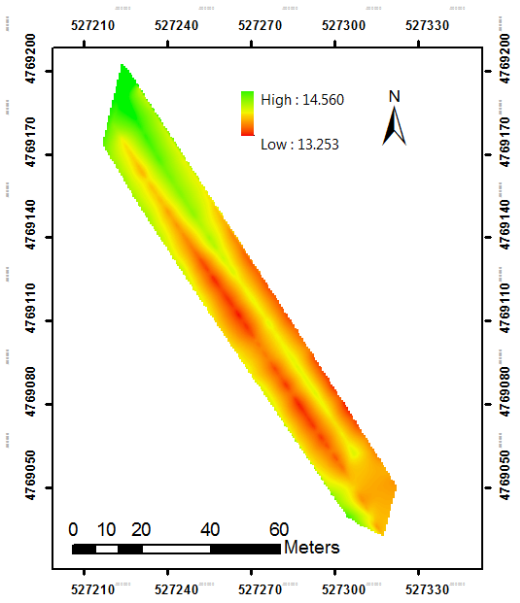

Fig.3. 7 Interpolation result using natural neighbor method

Kriging model, which is an advanced geostatistical procedure, interpolates scattered points with z–values to create a raster surface. Whilst the above mentioned interpolation methods including IDW, spline, or natural neighbor are solely based on the surrounding measured points' z–values for estimating the z–value for each interpolation point, Kriging model is essentially different from them because it is based the geostatistical relationships among the measured points by assuming that the spatial correlation between measured points can be used to explain variations in the surface. Thus, in contrast with the IDW model, the weight parameter for each surrounding measured point in the Kriging model is not only based

on the distance to the interpolation point but also influenced by the overall spatial autocorrelation of the measured points, expressed as Eq. (3.9). Kriging interpolation is originated from mineral exploration, and is very popular in geological analysis. In this study we used the ordinary Kriging method with the spherical semivariogram model in ArcMap software to generate a topographic map from the 1135 UAV-LiDAR system based topographic surveying data described in Chapter 2, shown in Fig.3. 8. From the resulting surface map we may conclude that the Kriging method based topographic map is very similar to the IDW method based one: the general high-north-low-south trend of the ground elevation of the field under study can be clearly observed, and a ditch (in red color) in south-north direction could also be visualized.

$$\hat{z}(x,y) = \sum_{i=1}^{n_{kri}} w_i z(x_i, y_i) \tag{3.9}$$

where $\hat{z}(x,y)$, n_{kri}, w_i, and, $z(x_i, y_i)$ is the estimated z-value of the interpolation point, the number of measured points included in the Kriging model (using the default value of 12 in this study), weighting factor of each measured points, and each measured point's z -value, respectively.

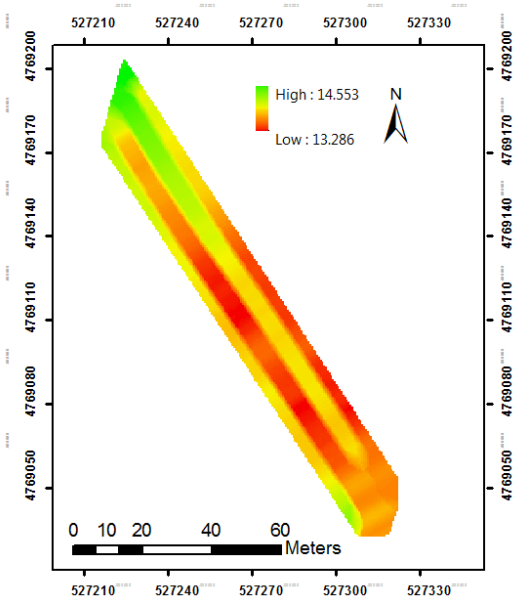

Fig.3. 8 Interpolation result using Kriging method

3.2.2 Generating Low-altitude Aerial Photogrammetric DSM

Aerial photogrammetric DSM is suitable for large-scale areas or mountainous areas where it is not easy to directly measure the ground elevations. Aerial photogrammetric DSM is also featured with good spatial resolution, and it has been reported that about 85% of topographic maps are generated using aerial photogrammetric techniques [62]. However, generating photogrammetric DSM from aerial photographs usually needs high-quality arrangement of GCPs spreading uniformly around the whole area of interest. Unfortunately, it is always impossible in practice to find enough distinguishable features both in real world as well as aerial images to be used as GCPs in farmlands, and artificially setting up enough markers as GCPs seems not only time-consuming but also not feasible during crop growing season for crop height estimation. Thus, in this study we investigated the accuracy of ground elevation values extracted from the aerial photographic DSM by comparing them with the corresponding RTK-GPS data explained in Chapter 2.

Table 3. 1 Flight plan and camera specifications

Flight Plan		**Camera Specification**	
Altitude (above ground level, m)	80	Weight (gram)	180
Endurance (min)	2	Dimensions (cm)	12.1 * 6.6 * 4.6
Flight Range (m)	400	Camera resolution	1280 × 960 pixels
Speed (m/s)	6	Focal length (mm)	5.5
Captures	121	Sensor size(mm)	4.8 × 3.6
Tracks	2	Horizontal Field of View (degree)	47.2

The aerial photogrammetric DSM is acquired by stitching 121 individual images based on multi-view 3D reconstruction image processing technique in Agisoft PhotoScan software. The RedEdge camera (MicaSense Inc., Seattle, WA, USA) was used to take these images, which is installed on the UAV platform described in Chapter 2. The UAV-camera system flew at about 80 m above ground level with the ground speed of about 8 m/s and the flight track interval of 15 m. The camera captured one image per second with the spatial resolution of about 0.05 m (5 cm). Accordingly, the forward overlap rate and the side overlap rate could be calculated as 83% and 77%. According to the specifications for office operation of low-altitude digital aero-photogrammetry, the minimum forward overlap rate and side overlap rate is claimed no less than 53% and 8%, respectively, and our flight satisfies the operation

requirements. Four field corners were selected as GCPs in this experiment, and the geospatial coordinates were measured by using RTK-GPS module to geo-reference the resulting photogrammetric DSM.

The process of generating photogrammetric DSM from low-altitude aerial images was shown in Fig.3. 9, and the resulting photogrammetric DSM is shown in Fig.3. 10. In the DSM map four GCPs' locations were indicated using star marks in black color, and the field of interest was distinguished using black polylines (RTK-GPS's trajectory). From the DSM map we can see that the surface elevation varies from 3.86 m to 18.724 m and it does not comply with the real world situation. We may conclude that the absolute accuracy of the field's surface elevation is not reliable, due to the poor capability of interpolation when the elevation values of the features that are outside the rein of GCPs are determined. However, we may also conclude that the low-altitude aerial photogrammetric DSM has good relative accuracy: in the north-most area we can see the growing maize stalks (about 2 m in height) were distinctively depicted in green color (the highest surface elevation); in the middle part of the west-most area we can see the growing soybean stalks (about 0.8 m in height) were depicted in yellow color (medium-high surface elevation); the harvested wheat field's bare soil part was shown in red color (low surface elevation); whilst the ditch (about 2 m in depth) over the northern headland of the wheat field was shown in dark red color (the lowest surface elevation).

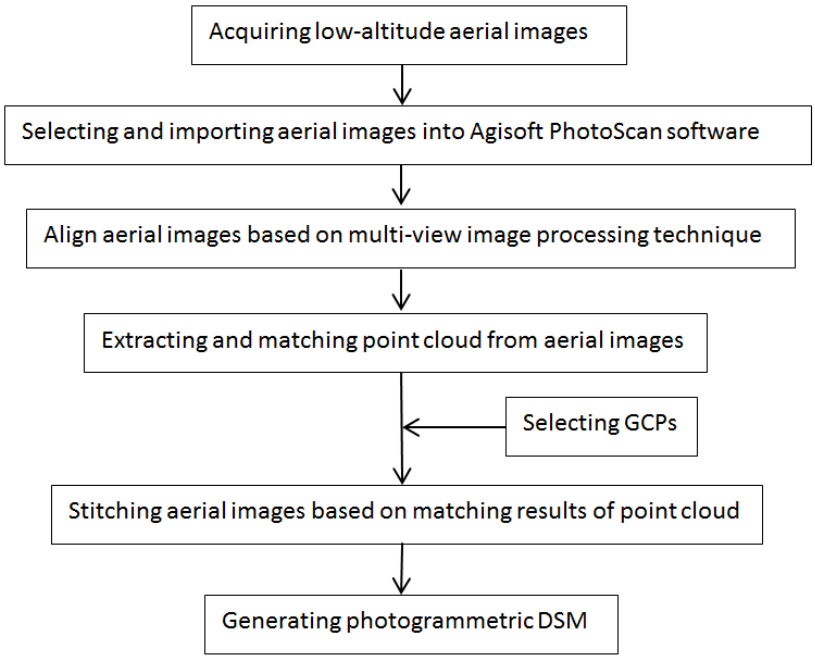

Fig.3. 9 Workflow of generating photogrammetric DSM

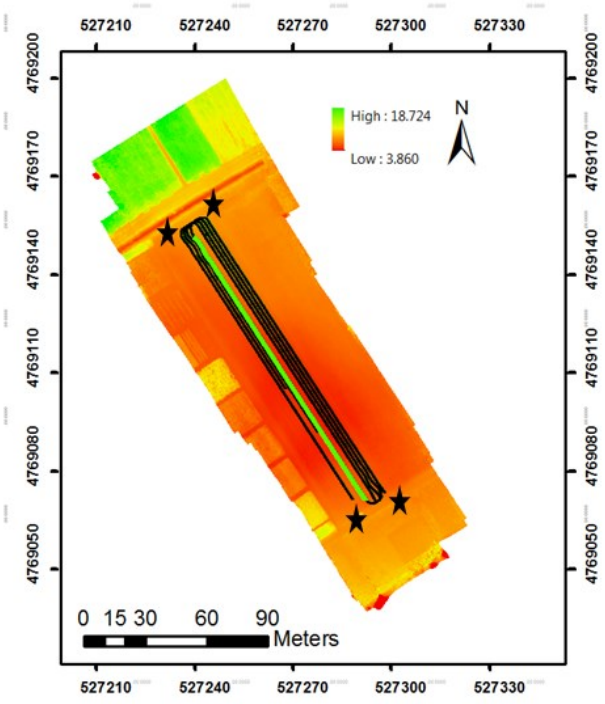

Fig.3. 10 The resulting photogrammetric DSM from aerial images

3.2.3 Integrating Aerial Photogrammetric DSM with UAV-LiDAR Data

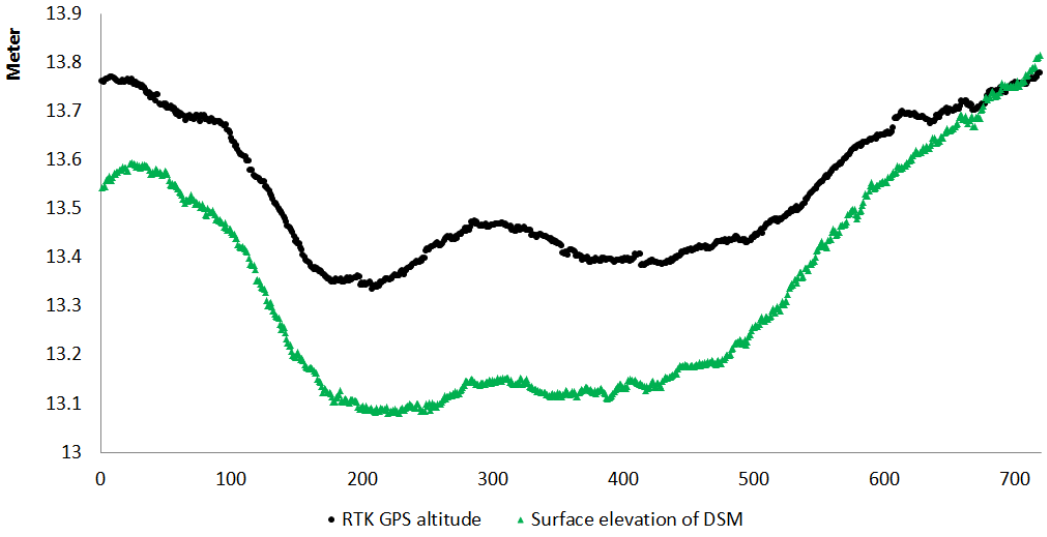

Fig.3. 11 Variations of RTK-GPS's altitude and the corresponding DSM's surface elevation data

A set of RTK-GPS data were used in order to evaluate the ground surface elevation values of the resulting aerial photogrammetric DSM. The spatial distribution of RTK-GPS samples for validation was also shown in Fig.3. 10 in bright green color. Subsequently,

surface elevation data which shares the same coordinates with these RTK-GPS samples were extracted from the aerial photogrammetric DSM in ENVI software (Exelis VIS, Inc., Boulder, CO, USA). The variations of RTK-GPS's altitude as well as the corresponding aerial photogrammetric DSM's surface elevation data were shown in Fig.3. 11. From Fig.3. 11 we may conclude that surface elevation values of the DSM samples that are near to the GCPs have good absolute accuracy when compared with the corresponding RTK-GPS samples' altitude, and the accuracy of DSM samples' surface elevation values decreases as samples deviate from the GCPs. Nonetheless, from the highly coincident tendencies of these two sets of elevation data we may come to a conclusion that the relative accuracy between the neighboring pixels of the aerial photogrammetric DSM is considerably good. Therefore, we came up with a solution which utilizes the relative difference of the surface ground elevations among the neighboring pixels of the aerial photographic DSM for integration with the UAV-LiDAR system based topographic surveying data, described in Chapter 2, for an improved topographic map.

This method utilizes the simple and autonomous flight of the UAV-LiDAR system and requires only a few boundary corners to be measured as GCPs for the generation of aerial photogrammetric DSM (usually measuring the coordinates of 4 corners of the field under study is the minimum requirement for geo-referencing purpose). Firstly, all of the 1135 UAV-LiDAR system based topographic surveying points (shown in Fig.3. 12 as larger dots) were defined as standard data set, denoting ($x_{UAVi,}\, y_{UAVi,}\, z_{UAVi}$). Furthermore, the georeferenced aerial photogrammetric DSM was processed using a median filter (with the kernel size of 11) in ENVI software for such reasons: a). Adverse impact of the potential misplaced geo-registration between each UAV-LiDAR system based topographic surveying data and the corresponding pixel of the geo-referenced aerial photogrammetric DSM could be compensated; b). The abnormal values of the ground surface elevations of the aerial photogrammetric DSM could be screened out, which tend to occur during multi-view 3D image reconstruction process due to feature mismatching, camera intrinsic malfunction, and etc. Secondly, ground surface elevation values of the points that share the same geospatial coordinates with the standard data set were acquired out of the median-filtered aerial photogrammetric DSM and defined as reference data set, denoting ($x_{UAVi,}\, y_{UAVi,}\, z_{DSMi}$). Thirdly, surface elevation values of the surrounding points (shown in Fig.3. 12 as smaller dots amounting to as many as 6810 points) within the neighboring areas of the standard data set were also acquired from the same median filtered aerial photogrammetric DSM, denoting

($x_{neighbori}$, $y_{neighbori}$, $z_{neighbori}$). Subsequently, the differences of ground surface elevation values between each point of reference data set and its corresponding neighboring point were calculated according to Eq. (3.15). Finally, the aerial photogrammetric DSM based surface elevation of each surrounding point could be rectified using the corresponding UAV-LiDAR system based topographic surveying data according to Eq. (3.16), denoting ($x_{neighbori}$, $y_{neighbori}$, $z'_{neighbori}$).

$$\Delta z_i = z_{neighbori} - z_{DSMi} \tag{3.15}$$

$$z'_{neighbori} = z_{UAVi} + \Delta z_i \tag{3.16}$$

where $z_{neighbori}$, z_{DSMi}, and Δz_i is the aerial photogrammetric DSM's surface elevation values of the surrounding points within the neighboring areas of the reference data set, the aerial photogrammetric DSM's surface elevation values of the reference data set, and the difference of ground surface elevation between each point of reference data set and its corresponding neighboring point, respectively; whilst z_{UAVi} and $z'_{neighbori}$ is the ground elevation value of the UAV-LiDAR system based topographic surveying points and the rectified ground elevation values of each surrounding point.

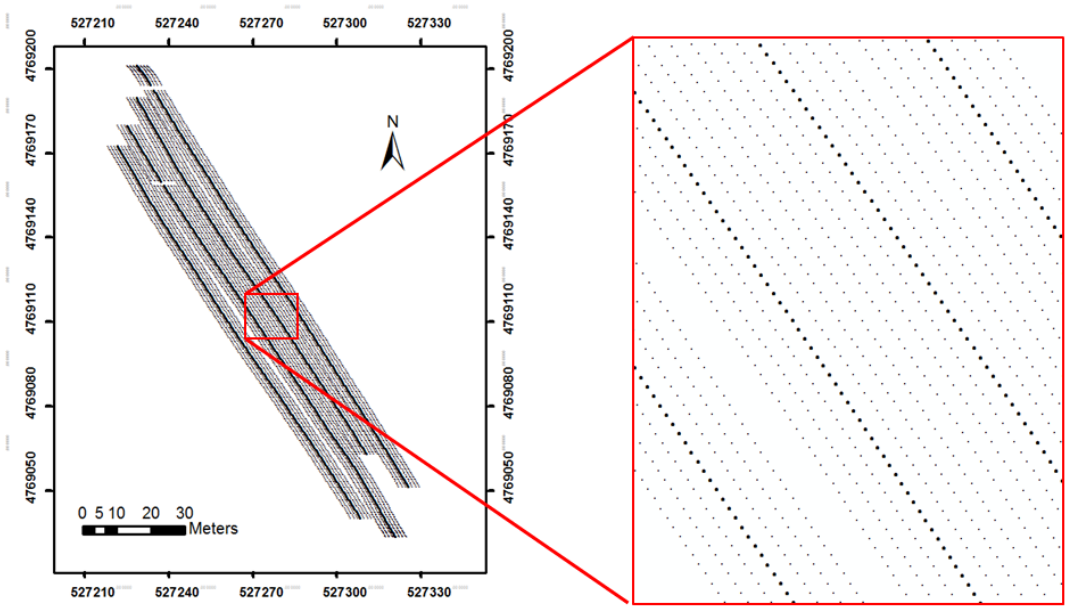

Fig.3. 12 Improved spatial resolution of topographic surveying points

3.3 Results and Discussion

3.3.1 Evaluating Topographic Maps Based on Different Interpolating Methods

The accuracy of the interpolated topographic map is depending on two systems of error: one is the measuring accuracy of each sampled points, i.e. the primitive error. As mentioned in Chapter 2, the RSME between ground elevation value of each RTK-GPS surveying point and the corresponding ground elevation value of the UAV-LiDAR system based topographic surveying point was calculated as 0.035 m. Considering that the ground elevation of the field under study varies from 13.237 m to 14.594 m according to the topographic survey data using the UAV-LiDAR system, the RMSE is acceptable when compared with the elevation difference of 1.357 m, which demonstrated that the primitive error of the UAV-LiDAR topographic surveying system is minimal. The other system of error adheres to the mathematical model of each specific interpolation method, i.e. the interpolation error. Interpolation error is the main source that contributes to the accuracy of the resulting topographic surface map, as the z–value of each interpolation point is not only determined by the surrounding measured points' z–values but also influenced by the neighboring measured points' spatial distribution, density, and etc.

Table 3. 2 Samples for evaluating accuracy of each interpolation method (in part)

Sample Numbe	Geo-spatial coordinates		Ground elevation (m)					
	Easting	Northing	RTK-GPS	TIN	IDW	Kriging	Spline	Natural Neighbo
1	527314.13	4769057.87	13.689	13.643	13.731	13.723	15.285	13.642
2	527315.63	4769062.87	13.645	13.598	13.570	13.573	14.683	13.597
3	527313.14	4769066.34	13.613	13.606	13.595	13.594	14.675	13.603
4	527308.13	4769066.87	13.558	13.581	13.676	13.669	13.335	13.655
5	527316.98	4769067.10	13.653	13.658	13.595	13.582	13.737	13.583
…	…	…	…	…	…	…	…	…
48	527252.63	4769166.87	13.875	13.921	13.917	13.916	13.924	13.994
49	527251.29	4769168.51	13.889	13.942	13.940	13.944	13.943	13.946
50	527244.13	4769176.37	13.852	14.142	13.982	14.030	14.224	14.142

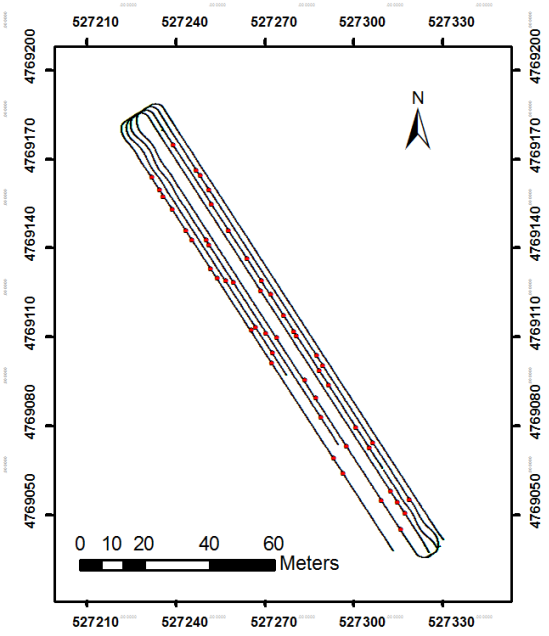

Fig.3. 13 Distribution of RTK-GPS samples for evaluating interpolation models' accuracy

In this study, 50 RTK-GPS samples with 3D coordinates (easting, northing, and altitude) were collected randomly around the whole field under study, shown in Fig.3. 13, in order to evaluate five different interpolation models' applicability in representing the within-field variations of ground elevation for farmlands that are going to be precisely leveled. These RTK-GPS data were explained in Chapter 2. According to the 50 RTK-GPS samples' easting and northing coordinates, another 50 samples' z –values were extracted out of the TIN, IDW, spline, natural neighbor, and Kriging model based topographic map, respectively, which share the same coordinates with the RTK-GPS samples, listed in Table 3. 2.

Subsequently, the ground elevation values of each sampled points, which are extracted from different topographic maps based on each specific interpolation methods, were compared with the corresponding ground elevation values of the RTK-GPS data. Fig.3. 14 indicates the variations of ground elevation values of sampled points both from RTK-GPS data and each resulting topographic map based on different interpolation methods. From the figure we can easily understand that the spline model is most unsuitable to be used for interpolating ground elevation data for generating a topographic map, when compared with other interpolation models. Besides, samples of all of these interpolation models at different locations indicate varied accuracy when compared with the reference values of RTK-GPS data. For example, the ground elevation data with the sample sequence number of 5, 11, 19,

20, 21, 26, 27, 38, 42, 44, and 49 of all these five interpolation models have quite good accuracy when compared with the reference values of RTK-GPS data; however, ground elevation data with other sequence numbers deviate badly from the corresponding RTK-GPS data in one interpolation model or another.

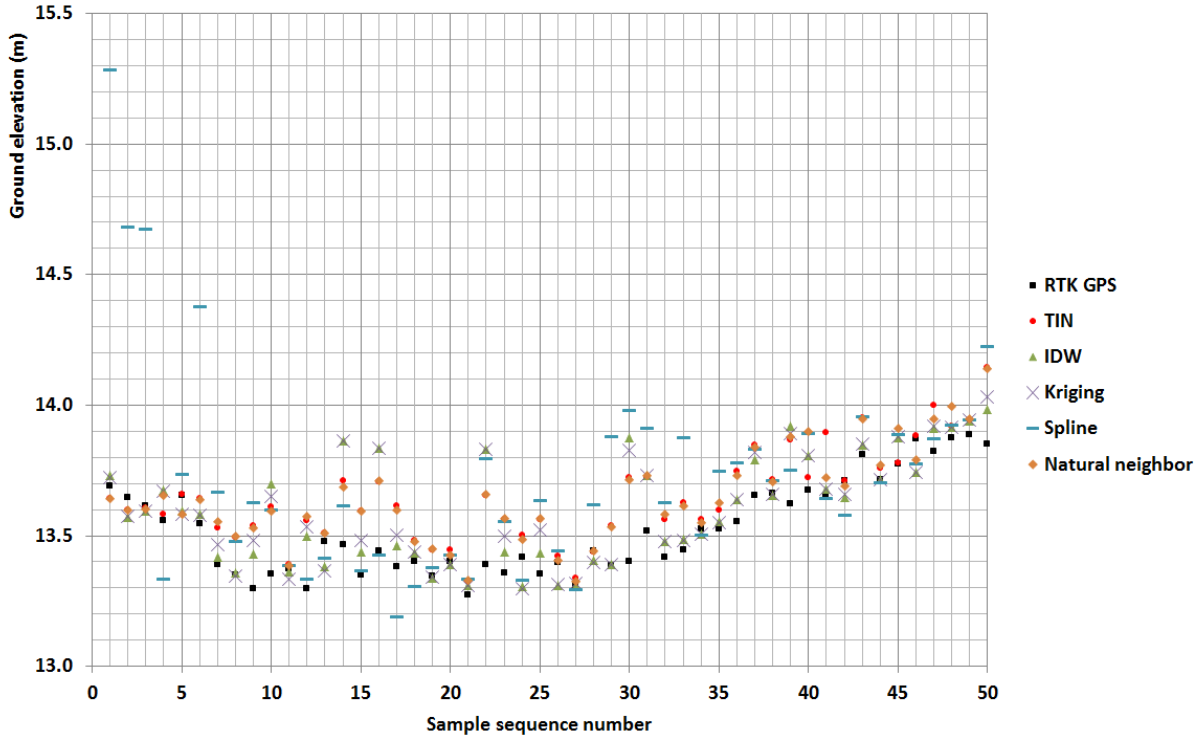

Fig.3. 14 Variations of sampled ground elevation of RTK-GPS data and topographic maps

Finally, the accuracy of each topographic surface map based on different interpolation models is quantitatively analyzed by calculating the RMSEs between the reference ground elevation values of RTK-GPS data and the interpolated ground elevation values of each resulting topographic maps by using TIN model, IDW model, spline model, natural neighbor model, and Kriging model, respectively, according to Eq. (3.10) ~ Eq. (3.14). And the results are as follows: $\mathrm{RMSE}_{\mathrm{TIN}} = 0.137\mathrm{m}$, $\mathrm{RMSE}_{\mathrm{IDW}} = 0.158$ m, $\mathrm{RMSE}_{\mathrm{spl}} = 0.388\mathrm{m}$, $\mathrm{RMSE}_{\mathrm{nat}} = 0.139$ m, and $\mathrm{RMSE}_{\mathrm{Kri}} = 0.160$ m, respectively. We may conclude that the TIN model is the most suitable interpolation model for the study of representing within-field variations of ground elevation by using UAV-LiDAR topographic surveying data, whilst the other four interpolation models have relatively poor capability of interpolating UAV-LiDAR data for generating a topographic map of a farmland.

$$RMSE_{TIN} = \sqrt{\frac{\sum_{i=1}^{50}(e_{RTki} - e_{TINi})^2}{50}} \quad (3.10)$$

$$RMSE_{IDW} = \sqrt{\frac{\sum_{i=1}^{50}(e_{RTki} - e_{IDWi})^2}{50}} \quad (3.11)$$

$$RMSE_{spl} = \sqrt{\frac{\sum_{i=1}^{50}(e_{RTki} - e_{spli})^2}{50}} \quad (3.12)$$

$$RMSE_{nat} = \sqrt{\frac{\sum_{i=1}^{50}(e_{RTki} - e_{nati})^2}{50}} \quad (3.13)$$

$$RMSE_{Kri} = \sqrt{\frac{\sum_{i=1}^{50}(e_{RTki} - e_{Krii})^2}{50}} \quad (3.14)$$

where $RMSE_{TIN}$, $RMSE_{IDW}$, $RMSE_{spl}$, $RMSE_{nat}$, and $RMSE_{Kri}$ is the root mean square error between the reference ground elevation values of RTK-GPS data and interpolated ground elevation values by using TIN model, IDW model, spline model, natural neighbor model, and Kriging model, respectively; whilst e_{RTki}, e_{TINi}, e_{IDWi}, e_{spli}, e_{nati}, and e_{Krii} is the ground elevation value of each sample of the RTK-GPS data, the ground elevation value of each sample from topographic maps by using TIN, IDW, spline, natural neighbor, and Kriging interpolation model, respectively.

3.3.2 Evaluating Accuracy of the Improved Topographic Map

1135 original UAV-LiDAR system based topographic surveying data as well as the 3D coordinates of 6810 surrounding points were acquired, and the ground elevation values of the surrounding points were rectified by integrating the aerial photogrammetric DSM data with the corresponding UAV-LiDAR system based topographic data. Out of these 7945 points' ground elevation values, improved topographic maps based on TIN, IDW, Kriging, Spline, and natural neighbor interpolation models were generated, respectively. Subsequently, the ground elevation's accuracy were also validated by comparing 50 randomly distributed RTK-GPS samples' altitude with the corresponding samples' ground elevation values that were extracted from the improved topographic maps based on different interpolation models as well as the aerial photogrammetric DSM, shown in Fig.3. 15. These 50 groups validating samples share the same geospatial coordinates with the ones for validating each topographic map generated from the original UAV-LiDAR system based topographic surveying data, also shown in Fig.3. 13.

From Fig.3. 15 we may conclude that the sampled ground elevation values of the aerial photogrammetric DSM have the smoothest tendency; however, it also expressed the most deviated situation from the corresponding reference RTK-GPS data; and same with situation in Fig.3. 14 spline interpolation model is still most unsuitable to be used for interpolating ground elevation data for generating a topographic map of a farmland due to a wide range of fluctuation. Besides, samples of all of these interpolation models for the improved topographic maps at different locations indicate varied accuracy when compared with the corresponding altitude values of RTK-GPS data. The ground elevation data with the sample sequence number of 5, 8, 11, 19, 20, 21, 26, 27, 28, 29, 34, 35, 36, 38, 41, 42, 44, 47, 48, and 49 of all these five interpolation models have very good accuracy when compared with the corresponding altitude values of RTK-GPS data; and the overall accuracy of ground elevation values of most samples of these different improved topographic maps was improved by a large extent. The ground elevation's accuracy of the resulting aerial photogrammetric DSM, as explained in Sec.3.2.3, is good when the sample is near to the location of GCPs and deteriorates as the distance from the sample to the location of GCPs increases.

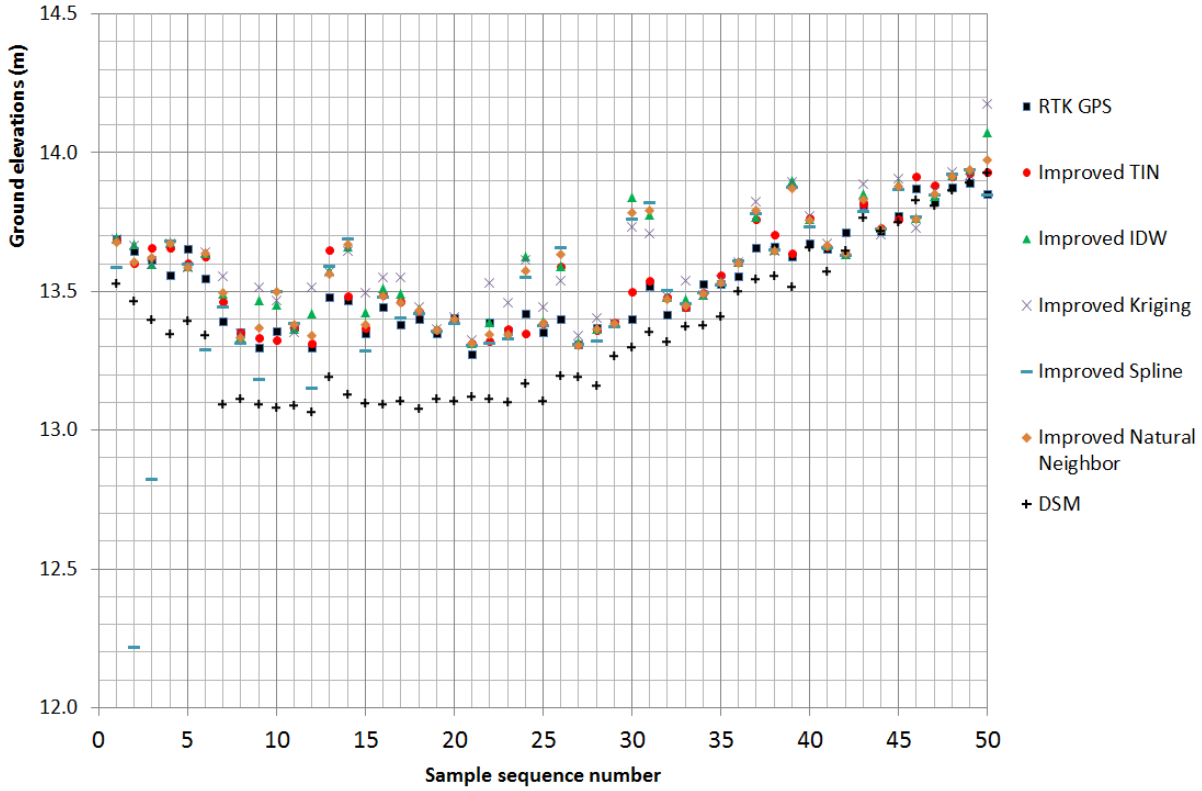

Fig.3. 15 Variations of sampled ground elevation of RTK-GPS data and improved topographic maps as well as the aerial photographic DSM

Table 3. 3 Samples for evaluating accuracies of the aerial photogrammetric DSM and the improved topographic maps (in part)

Sample Numbe	Ground elevation (m)						
	RTK-GPS	Improved TIN	Improved IDW	Improved Kriging	Improved Spline	Improved Natural Neighbor	Aerial DSM
1	13.689	13.685	13.694	13.691	13.586	13.677	13.527
2	13.645	13.603	13.670	13.665	12.218	13.605	13.466
3	13.613	13.658	13.598	13.600	12.823	13.621	13.398
4	13.558	13.657	13.678	13.672	13.681	13.674	13.345
5	13.653	13.602	13.589	13.588	13.599	13.587	13.394
…	…	…	…	…	…	…	…
48	13.875	13.914	13.919	13.932	13.921	13.914	13.863
49	13.889	13.927	13.939	13.919	13.937	13.937	13.892
50	13.852	13.930	14.071	14.177	13.847	13.976	13.927

The ground elevation values extracted from the improved topographic maps based on different interpolation models as well as the aerial photogrammetric DSM and the corresponding RTK-GPS altitude data were, in part, listed in Table 3. 3. And accordingly the RMSEs between each sample's RTK-GPS altitude and the corresponding samples' ground elevation value extracted from the improved topographic maps as well as the aerial photogrammetric DSM were calculated, respectively, according to Eq. (3.15)~ Eq. (3.20).

$$RMSE_{impTIN} = \sqrt{\frac{\sum_{i=1}^{50}\left(e_{RTki}-e_{impTINi}\right)^2}{50}} \tag{3.15}$$

$$RMSE_{impIDW} = \sqrt{\frac{\sum_{i=1}^{50}\left(e_{RTki}-e_{impIDWi}\right)^2}{50}} \tag{3.16}$$

$$RMSE_{impspl} = \sqrt{\frac{\sum_{i=1}^{50}\left(e_{RTki}-e_{impspli}\right)^2}{50}} \tag{3.17}$$

$$RMSE_{impnat} = \sqrt{\frac{\sum_{i=1}^{50}\left(e_{RTki}-e_{impnati}\right)^2}{50}} \tag{3.18}$$

$$RMSE_{impKri} = \sqrt{\frac{\sum_{i=1}^{50}\left(e_{RTki} - e_{impKrii}\right)^2}{50}} \quad (3.19)$$

$$RMSE_{DSM} = \sqrt{\frac{\sum_{i=1}^{50}\left(e_{RTki} - e_{DSMi}\right)^2}{50}} \quad (3.20)$$

where $RMSE_{impTIN}$, $RMSE_{impIDW}$, $RMSE_{impspl}$, $RMSE_{impnat}$, $RMSE_{impKri}$, and $RMSE_{DSM}$ is the root mean square error between each sample's RTK-GPS altitude and the corresponding ground elevation value extracted from the improved topographic maps by using TIN, IDW, spline, natural neighbor, and Kriging interpolation model, respectively, as well as the aerial photogrammetric DSM; whilst e_{RTki}, $e_{impTINi}$, $e_{impIDWi}$, $e_{impspli}$, $e_{impnati}$, $e_{impKrii}$, and e_{DSMi} is the ground elevation value of each sample of the RTK-GPS data, the ground elevation values of each sample from improved topographic maps by using TIN, IDW, spline, natural neighbor, and Kriging interpolation model, respectively, as well as the aerial photogrammetric DSM.

As a result, $\mathrm{RMSE_{impTIN}}$, $\mathrm{RMSE_{impIDW}}$, $\mathrm{RMSE_{impspl}}$, $\mathrm{RMSE_{impnat}}$, $\mathrm{RMSE_{impKri}}$, and $\mathrm{RMSE_{DSM}}$ was calculated as 0.059 m, 0.118 m, 0.258 m, 0.107 m, 0.127 m, and 0.197, respectively. In comparison, the RSMEs between the same sets of RTK-GPS data with the corresponding ground elevation values that are extracted from the resulting topographic maps generated from the original 1135 sets of topographic surveying data of the UAV-LiDAR system based on different interpolation models have already been calculated in Sec. 3.3.1 as follows: $\mathrm{RMSE_{TIN}} = 0.137$ m, $\mathrm{RMSE_{IDW}} = 0.158$ m, $\mathrm{RMSE_{spl}} = 0.388$ m, $\mathrm{RMSE_{nat}} = 0.139$ m, and $\mathrm{RMSE_{Kri}} = 0.160$ m, respectively. Hereby we may conclude that the integration of aerial photogrammetric DSM data with the topographic surveying data based on the UAV-LiDAR system has distinctive benefits on improving the accuracy of each interpolated topographic map, and the improved topographic map based on TIN interpolation model has the best accuracy with the RSME of 0.059 m (5.9 cm).

The resulting topographic map generated from the integrated surveying data and based on the TIN interpolation model was shown in Fig.3. 16, from which we can clearly recognize the general high-north-low-south terrain of the field under study, and a long ditch over the west border of two adjacent fields in south-north direction could also be observed. Furthermore, the detailed fluctuation of ground elevation inside the field was much more obvious in this improved topographic map due to high spatially intensive measured points

(with the spatial resolution of about 1 m * 0.5 m), in comparison with the topographic map generated from the original UAV-LiDAR surveying points (with the resolution of about 6 m * 0.5 m). We may also see two deep puddles marked in black circle and rectangle in both Fig.3. 16 (the dark red areas) and Fig.3. 17 (the vegetative green area). Due to the relatively low ground elevation of these two puddles, wheat plants were drown (crop failure) during the growing season when precipitation is concentrative in October and snowmelt water converges in April. As the wheat plants die, weed ensues in the following days to cause further yield loss, shown in Fig.3. 17.

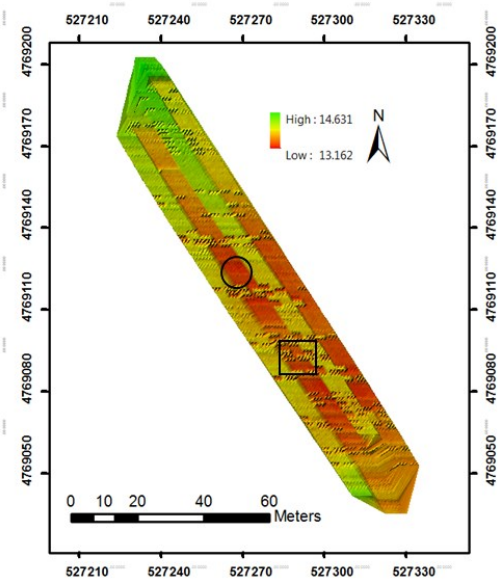

Fig.3. 16 Improved topographic maps using TIN interpolation method

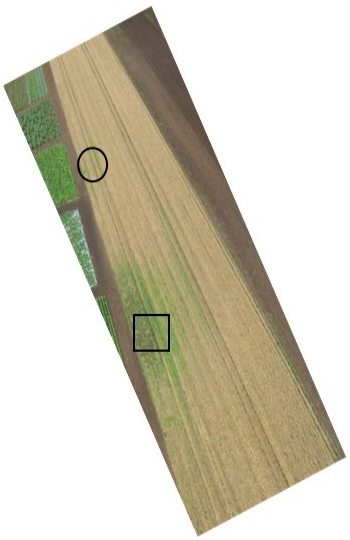

Fig.3. 17 Actual field condition of wheat (two days prior to harvesting)

3.4 Validating Experiment on Large-scale Farmland

A supplementary experiment was conducted on 7 September 2017 in a large-scale harvested wheat field (about 6 hectares) located in Memuro, Hokkaido, Japan, shown in Fig.3. 18, to validate the applicability of this topographic mapping methodology in large-scale farmlands by integrating low-altitude aerial photogrammetric DSM with the UAV-LiDAR system based topographic surveying data.

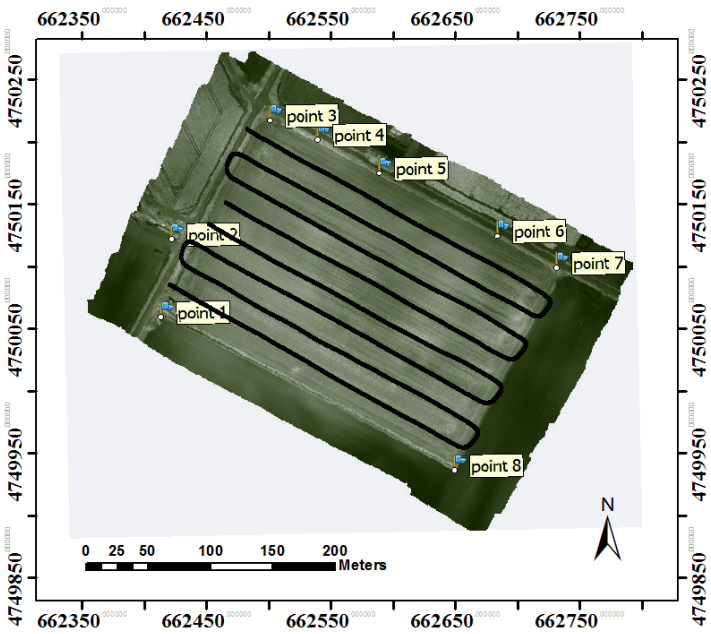

Fig.3. 18 Large-scale farmland used in the validating experiment

Totally about 400 individual images acquired by using the same UAV-camera system that were described in Sec.3.2.2 were stitched as an ortho-mosaic image, and a photogrammetric DSM was generated based on the 3D reconstruction image processing technique in Agisoft PhotoScan software. The photographic flight was also conducted at about 80 m above ground level with the ground speed of about 8 m/s and the flight track interval of 15 m. The camera captures one image per second with the spatial resolution of about 0.05 m (5 cm). According to the camera specification described in Sec.3.2.2, the ground coverage of each individual image reached up to about 48 m * 64 m, and the forward overlapping rate as well as the side overlapping rate could be calculated as about 83% and 77%, respectively. Eight points spreading around the farmland under study were selected as GCPs for geo-referencing the photogrammetric DSM, shown in Fig.3. 18, which are field corners, power transmission poles, and other distinguishable and clearly recognizable features

in both the real-world and each individual image. 3D coordinates of these GCPs were also measured by using the same RTK-GPS module with the centimeter-level accuracy, described in Sec.3.2.2. The resulting aerial photogrammetric DSM was shown in Fig.3. 19, from which we can see the general high-east-low-west terrain of the farmland under study. Besides, we can also conclude that the aerial photogrammetric DSM reveals good relative accuracy of the neighboring pixels, as the about 10-meter high trees, the about 5-meter high warehouse, the about 2-meter high corn plants, and the about 1-meter high wheat plants were depicted in deep green color, light green color, brown color, and brown-red color, respectively. However, the surface elevation around the farmland varies from 112.441 m to 137.625 m, denying the compliance with the real world, which obviously needs further processing for quantitative applications such as precision land levelling.

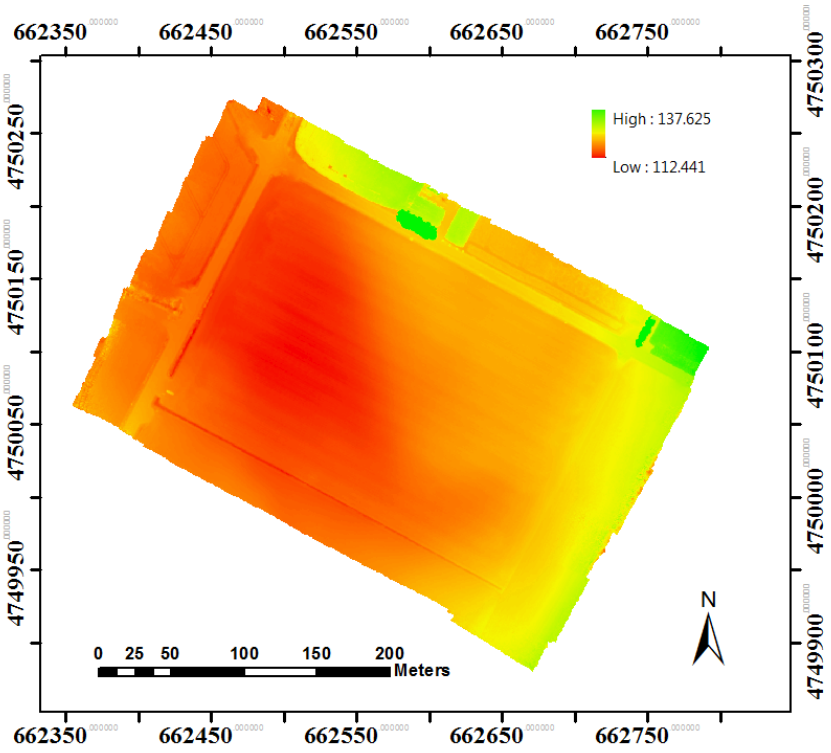

Fig.3. 19 The resulting aerial photogrammetric DSM

The UAV-LiDAR system based topographic surveying experiment was conducted over the same farmland after the aerial photogrammetric flights. The trajectories of were also shown in Fig.3. 18 as black lines, with the flight altitude of about 30 meter above ground level and at the ground speed of 5 m/s. The track intervals between each flight was set as 20

meters for large coverage, and the UAV-LiDAR system based topographic surveying points' spatial resolution could be accordingly calculated as 20 m * 0.5 m, described in Sec.2.3.1.

We removed the samples during the process of taking off, turning around, and landing of the UAV-LiDAR topographic surveying system, and totally 3889 sets of effective sample data were acquired. Using TIN interpolation method, a topographic map was generated based on these 3889 original UAV-LiDAR system's topographic surveying data, shown in Fig.3. 20. From Fig.3. 20 we may also conclude that the farmland under study has the same general high-east-low-west terrain feature with the one of the aerial photogrammetric DSM, and the ground surface elevation varies from 112.944 m to 118.818 m. With a heavy change in elevation of about 6 meters, this farmland desperately needs land forming operation in order to achieve optimal crop growth status and yield. For example, dividing this large-scale farmland into several terraced sub-zones and then implementing precision land leveling operation would be advisable, so that the fertile top soils over the high ground elevation area could be preserved to the maximum extent.

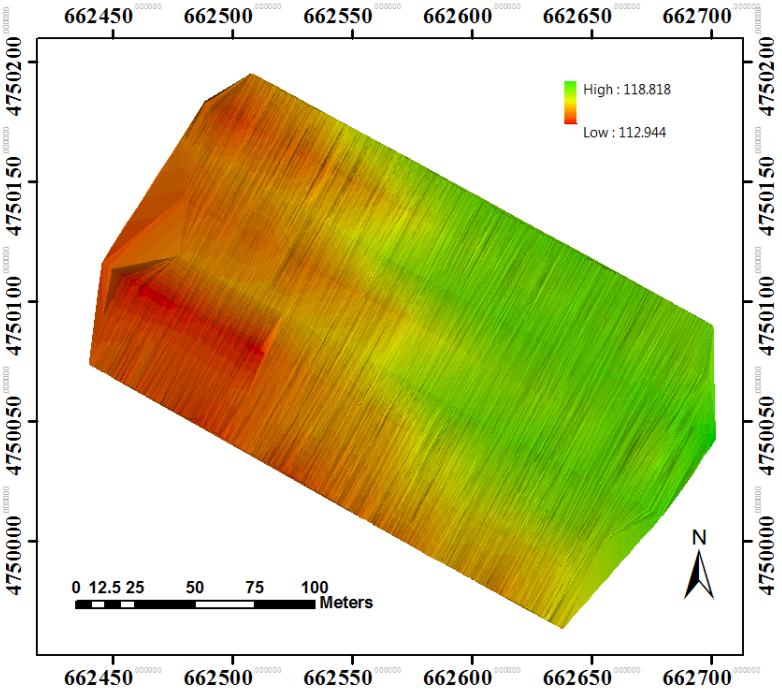

Fig.3. 20 The resulting topographic map based on TIN interpolation method using UAV-LiDAR system based topographic surveying data

We have already discussed in Chapter 2 that the poor spatial resolution of topographic surveying points influences the overall accuracy as well as the capability of demonstrating

the detailed features in an interpolated topographic map. In this section we are to evaluate the applicability of generating a topographic map by integrating ground elevation values of an aerial photogrammetric DSM with the topographic surveying data based on the UAV-LiDAR system for large-scale farmland.

Firstly, the spatial resolution of topographic surveying points was improved to about 1 m * 0.5 m from about 20 m* 0.5 m using the same methodology explained in Sec.3.2.3, shown in Fig.3. 21: the larger dots are the original topographic surveying data based on UAV-LiDAR system, whilst the smaller ones are neighboring samples whose ground elevation values are rectified using the same methodology explained in Sec.3.2.3. Subsequently, all of these original topographic surveying data based on the UAV-LiDAR system and the rectified neighboring samples were included to generate an improved topographic map using TIN interpolation model, and the resulting map was shown Fig.3. 22.

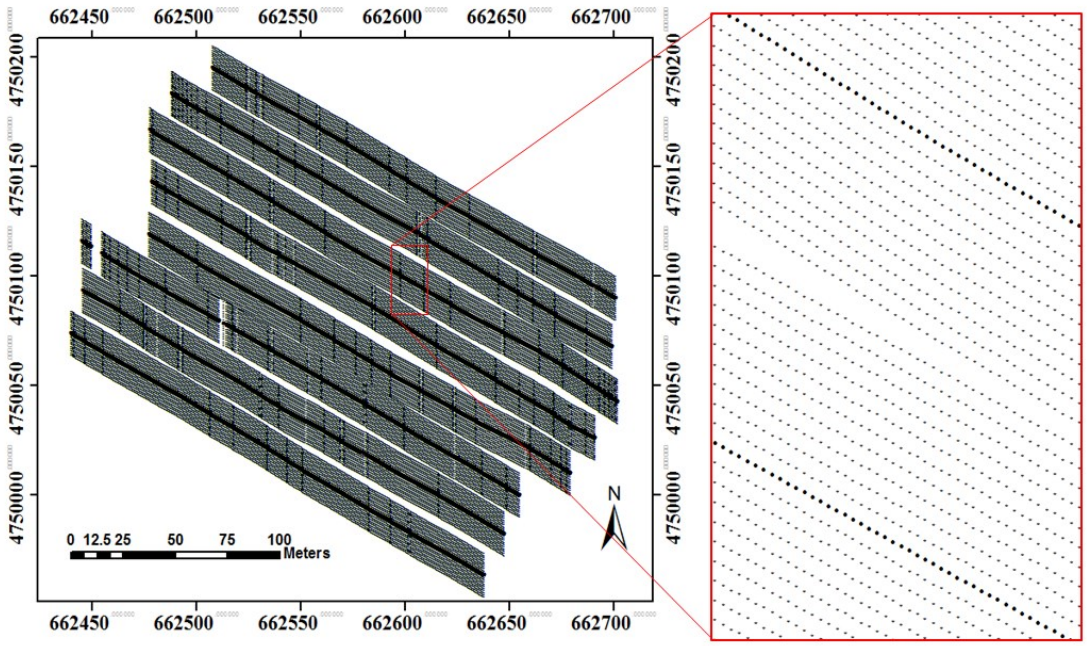

Fig.3. 21 Spatial distribution of topographic surveying data in large-scale farmland

From Fig.3. 22 we can conclude that the improved topographic map demonstrates much more detailed terrain information of the farmland under study than the former one that was merely based on the UAV-LiDAR system's topographic data, shown in Fig.3. 20, with the general high-east-low-west terrain and ground elevation's variation from 112.806 m to 119.098 m. Two large and several small puddles could also be spotted at the west most part

and in the middle part of the field, shown in red and dark yellow color, which poses potential threat to the healthy growth as well as yield of crops due to stagnant water and high humidity.

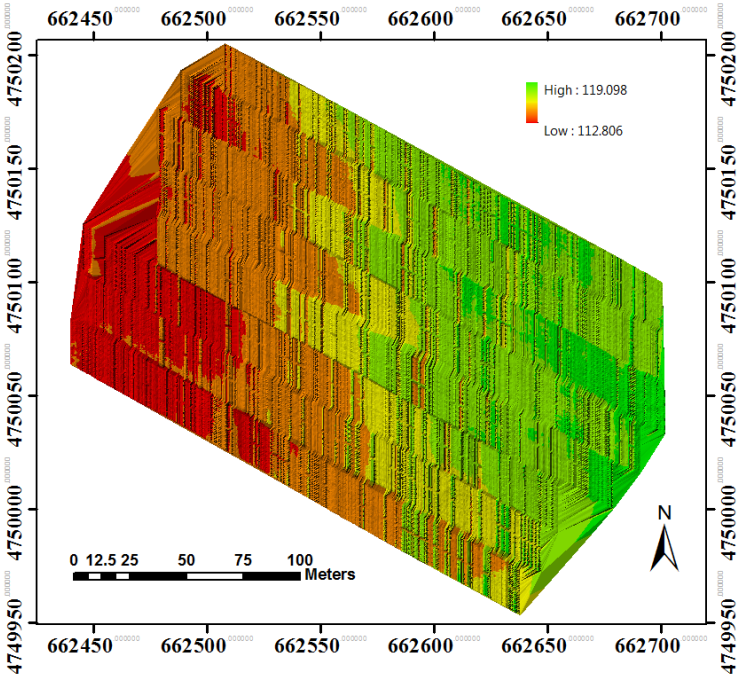

Fig.3. 22 The resulting topographic map by integrating aerial photogrammetric DSM and UAV-LiDAR system based topographic surveying data

Table 3. 4 Samples for evaluating accuracy of each interpolation method (in part)

Sample Number	Geo-spatial coordinates		Ground elevation (m)			
	Easting	Northing	PPK-GPS	Aerial DSM	Topographic Map	Improved Topographic
1	527314.13	4769057.87	114.165	114.264	113.908	113.939
2	527315.63	4769062.87	114.643	113.727	114.515	114.679
3	527313.14	4769066.34	114.213	113.839	114.360	114.439
4	527308.13	4769066.87	114.205	113.895	114.000	114.051
5	527316.98	4769067.10	114.134	113.978	114.085	114.032
…	…	…	…	…	…	…
18	662654.36	4750021.11	117.688	116.480	117.676	117.652
19	662665.97	4750049.94	117.838	116.648	117.900	117.864
20	662677.91	4750077.74	117.436	116.625	117.623	117.557

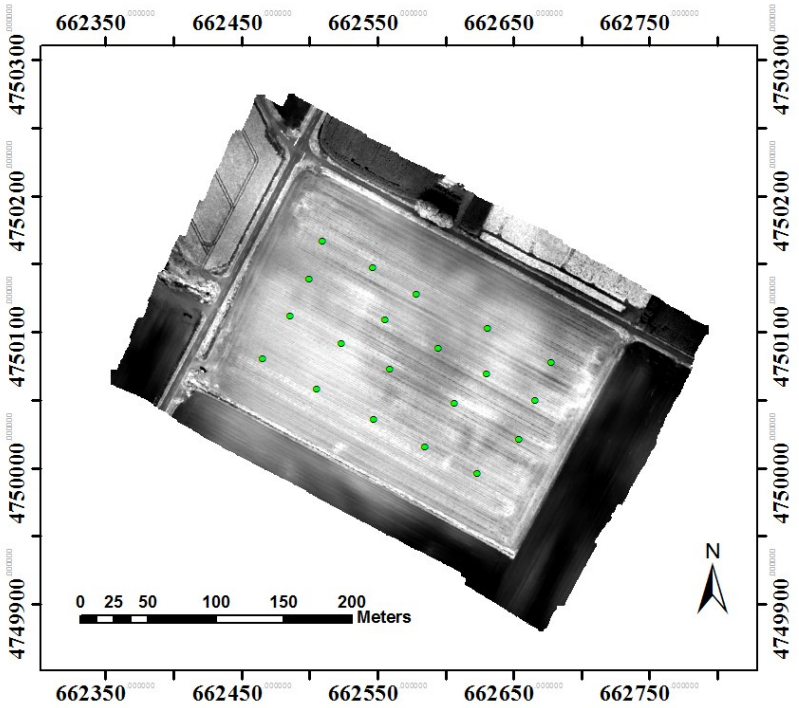

Fig.3. 23 PPK-GPS samples' spatial distribution

Finally, 20 samples' 3D coordinates were measured by using the handheld PPK-GPS module with the centimeter-level accuracy, explained in Sec.2.4.1. The coordinates of these samples were listed in Table 3. 4, and the spatial distributions were shown in Fig.3. 23. Accordingly, ground elevation values of the aerial photogrammetric DSM, the topographic map based on TIN interpolation model using the original UAV-LiDAR system's topographic surveying data, and the improved topographic map based on TIN interpolation model by integrating the UAV-LiDAR system's topographic surveying data and the aerial photogrammetric DSM data of these samples were extracted, respectively. The ground elevation values of different models were also listed in Table 3. 4, and RMSEs of sampled ground elevation data between the improved topographic map based on the UAV-LiDAR system's topographic surveying data and the aerial photogrammetric DSM, the topographic map based on the original UAV-LiDAR system's topographic surveying data, the aerial photogrammetric DSM, and the corresponding PPK-GPS's altitude was calculated according to Eq. (3.21) to Eq. (3.23). As the result, $\mathrm{RMSE}_{\mathrm{DSMlar}}$, $\mathrm{RMSE}_{\mathrm{TINlar}}$, and $\mathrm{RMSE}_{\mathrm{ImpTINlar}}$ was calculated as 1.040 m, 0.468 m, and 0.132 m, respectively. And we may conclude that the methodology of integrating UAV-LiDAR system based topographic surveying data with the

aerial photogrammetric DSM significantly improves the accuracy of the resulting topographic map by a large margin.

$$RMSE_{DSMlar} = \sqrt{\frac{\sum_{i=1}^{20}(e_{PPKi} - e_{DSMlari})^2}{20}} \quad (3.21)$$

$$RMSE_{TINlar} = \sqrt{\frac{\sum_{i=1}^{20}(e_{PPKi} - e_{TINlari})^2}{20}} \quad (3.22)$$

$$RMSE_{ImpTINlar} = \sqrt{\frac{\sum_{i=1}^{20}(e_{PPKi} - e_{ImpTINlari})^2}{20}} \quad (3.23)$$

where $RMSE_{DSMlar}$, $RMSE_{TINlar}$, and $RMSE_{ImpTINlar}$ is the root mean square error between the reference ground elevation values of PPK-GPS data and ground elevation values of the aerial photogrammetric DSM, the topographic map based on TIN interpolation model using the original UAV-LiDAR system's topographic surveying data, and the improved topographic map based on TIN interpolation model by integrating the UAV-LiDAR system's topographic surveying data and the aerial photogrammetric DSM, respectively; whilst e_{PPKi}, $e_{DSMlari}$, $e_{TINlari}$, and $e_{ImpTINlari}$ is the ground elevation value of each sample of the PPK-GPS data, the aerial photogrammetric DSM, the topographic map based on TIN interpolation model using the original UAV-LiDAR system's topographic surveying data, and the improved topographic map based on TIN interpolation model integrating the UAV-LiDAR system's topographic surveying data and the aerial photogrammetric DSM, respectively.

3.5 Conclusions

In this study we evaluated the accuracy of the ground elevation values and the capability of describing peaks and pits of the topographic maps based on different interpolation methods using the UAV-LiDAR topographic surveying system, so that scientific reference could be provided for precision land leveling conducted under the aid of each resulting topographic map. We firstly investigated the applicability of different interpolation methods for generating topographic maps using the 1135 sets of topographic surveying data of the UAV-LiDAR system, so that the most suitable model for interpolating field topographic surveying data into a topographic map could be determined. 50 RTK-GPS samples with 3D coordinates (easting, northing, and altitude) were collected randomly around the field under study. According to the RTK-GPS samples' geospatial coordinates, ground elevation values were extracted out of the topographic maps based on TIN, IDW, spline, natural neighbor, and

Kriging model, respectively. And we can understand that the spline interpolation model is most unsuitable to be used for interpolating ground elevation data for generating a topographic map, whilst the topographic map based on the TIN interpolation model is the most accurate one.

From the resulting topographic map based on the TIN interpolation model, we can see clearly that the field has a high-north-low-south trend in elevation varying from 13.237 m to 14.552 m; besides, we can also visualize a distinguishing ridge in south-north direction as well as a line of ditch in south-north direction within the field. According to field survey we confirmed that the ditch in south-north direction coincides with the border of two adjacent fields with relatively low ground elevation, where large area of wheat plants were drown to death and weeds spring up during the ripening growth stage of wheat. RMSE between the sampled reference altitude values of RTK-GPS data and the corresponding ground elevation values of the resulting topographic map based on TIN interpolation model was calculated as 0.137 m, which is not ideal but acceptable in consideration of the field's elevation change of about 1.4 m.

Then an aerial photogrammetric DSM model of the same field was created based on multi-view image processing techniques after acquiring digital images from a UAV-camera system. Ground elevation values were extracted out of the aerial photogrammetric DSM, which share the same geospatial coordinates with the original UAV-LiDAR system based topographic surveying data as well as the corresponding neighboring pixels. In this way, the spatial resolution of the surveying points was improved from about 6 m * 0.5 m to about 1 m * 0.5 m, as the spatial density of the surveying points also plays a paramount role in generating an accurate topographic map by using interpolation methods. Afterwards, the samples' ground elevation values of the aerial photogrammetric DSM were rectified and improved topographic maps were generated based on the totally 7945 sets of samples' ground elevation values using TIN, IDW, Kriging, Spline, and natural neighbor interpolation models, respectively. Accuracies of the improved topographic maps were also validated by calculating RMSEs between RTK-GPS samples' altitude and the corresponding samples' ground elevation values that were extracted from the improved topographic maps based on different interpolation models. We may conclude that the overall accuracy of each improved topographic map was improved by a large extent when compared with the accuracy of the corresponding topographic map generated by only using the original UAV-LiDAR system's

topographic surveying data. And still, TIN interpolation model expressed best performance when used to generate an improved topographic map based on the integrated data of aerial photogrammetric DSM and the original UAV-LiDAR system's topographic surveying data. The RSME between the RTK-GPS altitude and the corresponding ground elevation values of the improved topographic map based on TIN interpolation model was calculated as 0.059 m (5.9 cm), due to high spatially intensive interpolated points with the spatial resolution of about 1 m * 0.5 m. The accurate improved topographic map confirmed the feasibility of conducting topographic survey for farmlands by using the simple and efficient UAV-LiDAR system in combination with the low-altitude aerial photogrammetric flights.

Finally, we also experimentally validated the accuracy as well as feasibility of using such a topographic surveying outfit in a large-scale farmland, by changing the cross-track interval of the UAV-LiDAR topographic surveying flights from about 6 meters to about 20 meters for large coverage. We improved the spatial resolution of the interpolation points from about 20 m * 0.5 m to about 1 m * 0.5 m by integrating the original UAV-LiDAR system's topographic surveying data and the aerial photogrammetric DSM data, and an improved topographic map was generated using TIN interpolation model. We may conclude that the methodology of integrating UAV-LiDAR system based topographic surveying data with the aerial photogrammetric DSM significantly improves the accuracy of the resulting topographic map in large-scale farmland as well, when compared with the accuracies of the resulting topographic map solely using the UAV-LiDAR system's topographic surveying data and the photogrammetric DSM. The RMSE between the ground elevations of the improved topographic map, the original topographic map, as well as the aerial photogrammetric DSM, and the corresponding PPK-GPS's altitude was calculated as 0.132 m, 0.468 m, and 1.040 m, respectively. In consideration that the field is featured with a ground elevation change of about 6 m, we may conclude that the proposed methodology of generating topographic maps for precision land leveling by integrating UAV-LiDAR system based topographic surveying data with the low-altitude aerial photogrammetric DSM is of high practical values.

Chapter 4 Mapping within-Field Variations of Wheat Stalk Density

4.1 Introduction

Wheat (Triticum Spp., or Triticum Aestivum L.), a self-pollinate staple crop, has been amongst the first domesticated food crops and the most produced cereal grains for over 8000 years in human civilization. In 2009 the global wheat production reached about 680 million tons and in 2016 global production of wheat increased up to 749 million tons, which made it the second most-produced cereal grain after maize [63]. The demand of wheat from global market is still expending [64], as wheat is the leading source of vegetal protein due to its unique major component of gluten and also a rich source of multiple kinds of essential mineral nutrients. Wheat flour contains rather high protein content (about 13% and the value varies among different strains and varieties) when compared with other major cereal crops such as maize and rice, and world trade in wheat alone is greater than for all other crops combined [65].

In general it is divided into spring wheat and winter wheat even though the cultivation of wheat widespread over a vast geographical area all over the globe, according to flowering responses to cold temperatures. Spring wheat is normally sowed at early spring, which needs 110 to 130 days to complete vegetative growth and reproductive growth from sowing to harvesting, varying upon seed strain, climate, and soil conditions. On the other hand, winter wheat is usually sowed in the autumn to germinate and grow into a young plant which stays in a state of dormancy during winter time when temperature falls below 0 – 5 Celsius degree and resumes vegetative growth in early spring. The growth cycle of wheat includes germination, seedling establishment, tillering, stem elongation, heading, flowering, grain filling, ripening, and maturity. Detailed understanding of wheat growth status during each development stage is vital for optimal wheat field management operations. Several existing systems to identify wheat development stages are available, with Zadoks scale being the most widely used. Zadoks scale is a standard system which describes successive development stages reached by the crop during each agricultural season [66]. According to Zadoks scale, wheat development stages are generally divided into 10 distinct growth stages and of each specific growth stage, three to dozens of sub-stages are further identified with two-digits from 00 to 99 [67], shown in Fig.4. 1.

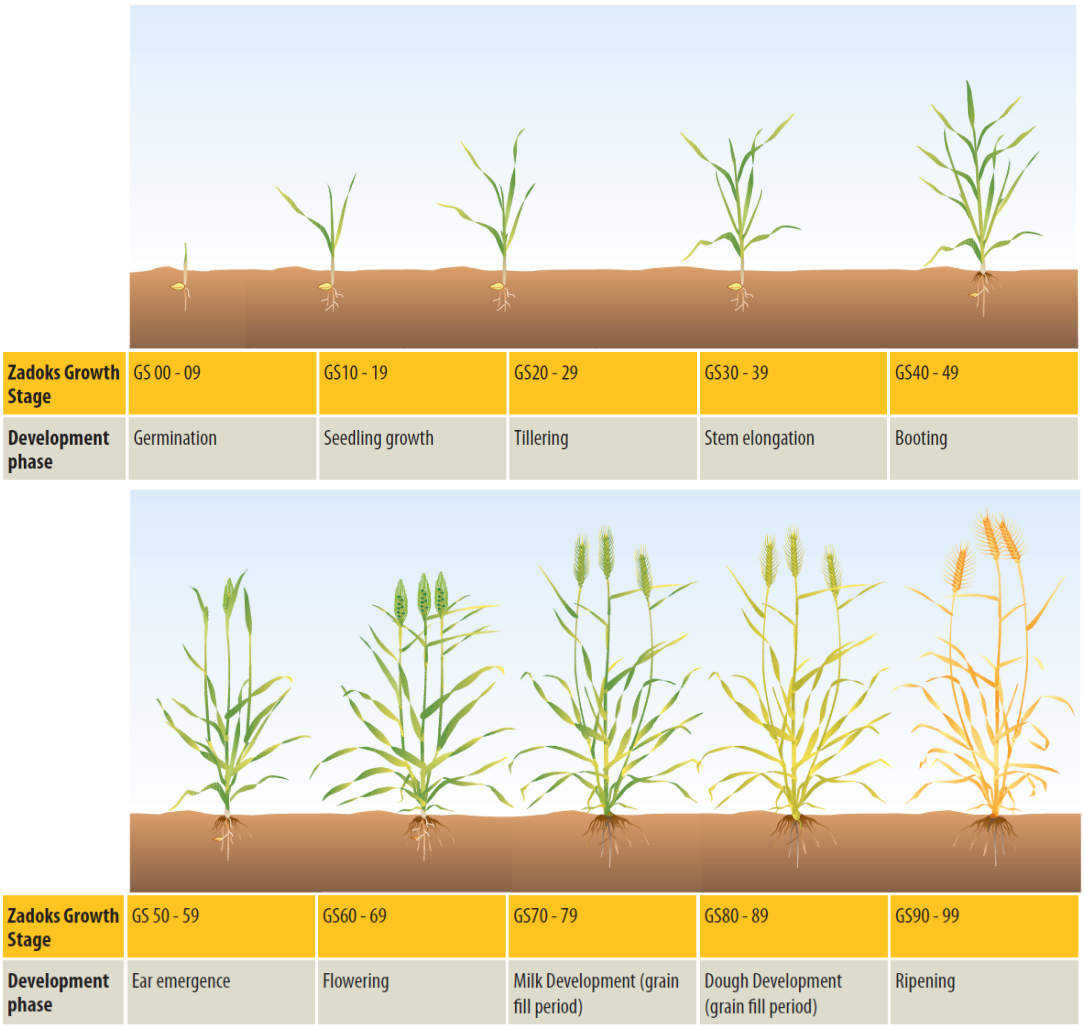

Fig.4. 1 Wheat development stages (illustration of Nick Poole, FAR)

Necessary operations such as herbicides and insecticides spraying as well as nitrogenous topdressing (for example urea solution) should be implemented timely, as different rate of nitrogenous topdressings, herbicides, and fungicides are typically applied only at specific stages during the wheat growth cycle. In order to optimize wheat yield and grain quality, especially in terms of protein content that varies significantly depending on different agricultural practices, field management in accordance with the specific growth situation of each wheat development stage is critical. For instance, the nitrogenous topdressings are advisable at the rate of 40~60 kg/ha during tillering stage (GS 20~29) so that the process of tillering could be stimulated and adequacy of stalks (or stalk density) could be guaranteed for enough wheat ears and thus the high yield. On the other hand, the nitrogenous topdressing rate of 20~30 kg/ha during the booting stage (GS 40~49) could boost grain weight and also grain protein content. Furthermore, recent studies on canopy management showed that not only spring fertilizer rate but timing of fertilization also should be tailored to achieve desired

canopy sizes at specific development phases, which means if the wheat stalk density is too low around the beginning of tillering stage, nitrogenous topdressing timing should be brought forward with a higher rate in order to boost the total number of stalks. Therefore, real time monitoring of actual wheat growth status throughout these several specific stages is of vital importance in helping wheat growers with field management decision making.

For many years, stalk counting has been used around the world as an empirical method of roughly estimating wheat stalk densities and understanding wheat growth status at early growth stages. Randy Weisz et al. developed a model for decision making related to wheat stalk densities before growth stage 30 [68], which was described as Eq. (3.1). According to the calculation, suggestions on different rates of nitrogenous topdressing could be proposed. Although it is feasible in case of small-scale wheat fields, this method is not suitable for large farmlands due to the time-consuming manual sampling operation. Besides, point-source information acquired through manually calculated stalk densities usually cannot accurately reflect the actual spatial-variated growth status even within small-scaled farmlands. On the other hand, remote sensing has been successfully used as an effective alternative for data collection in applications of precision agriculture through analysis of digitalized numbers of different bands of image data, or more often, of various kinds of vegetation indices calculated from the reflectance or radiance of specific bands [69]. Multi-spectral satellite imagery of visible and near infrared portions of the spectrum has been applied into detecting vegetation areas, monitoring crop growth status, and estimating crop yield, et al., in large scale. Whilst airborne remote sensing has been introduced into medium-scale agricultural application as a supplementary method and often carried out as one-time operations, which employs airplane or balloon as the carrier flying at the height of from less than 5,000m to 20,000m, and uses digital photography with sub-meter spatial resolution. Near-ground remote sensing is often referred to frame-based or pillar-based applications in the past, and recently the cutting edge application of small fixed-and/or rotary-wing UAVs used in small-scale and experimental field for spatial sampling or mapping for variable-rate operations has soared in the field of precision agriculture.

$$d = (t \times 4) / w \tag{4.1}$$

where d denotes the number of stalks per square meter, t denotes stalks per meter of row, and w denotes row width in meter.

Aerial photography has been used to monitor crop growth status since 1950s by using color or color-infrared cameras, but it is not until the start of the 21st century that widespread applications of UAVs occurred in agricultural precision management when aerial imagery using UAVs can be acquired more cost-effectively, with increasing spatial resolution due to low-altitude flight capacity, and with greater safety than manned aircraft [70]-[74]. Wang [75] et al. successfully differentiated vegetation areas from non-vegetation areas by analyzing color images acquired from a UAV; Rasmussen [76] et al investigated four different vegetation indices acquired from a color camera and a color-infrared camera by using both a fixed-wing UAV and a rotary-wing UAV, and concluded that vegetation indices based on UAV imagery have the same ability to quantify crop responses with ground-based recordings. In this study, we are to acquire aerial digital photographs by using an agricultural digital camera (ADC) mounted on the low-altitude UAV platform; and subsequently estimate the within-field spatial variations of wheat stalk density from the aerial images in a less time-consuming and accurate manner, so that suggestions on variable-rate nitrogenous topdressing could be accordingly recommended.

4.2 Methodology

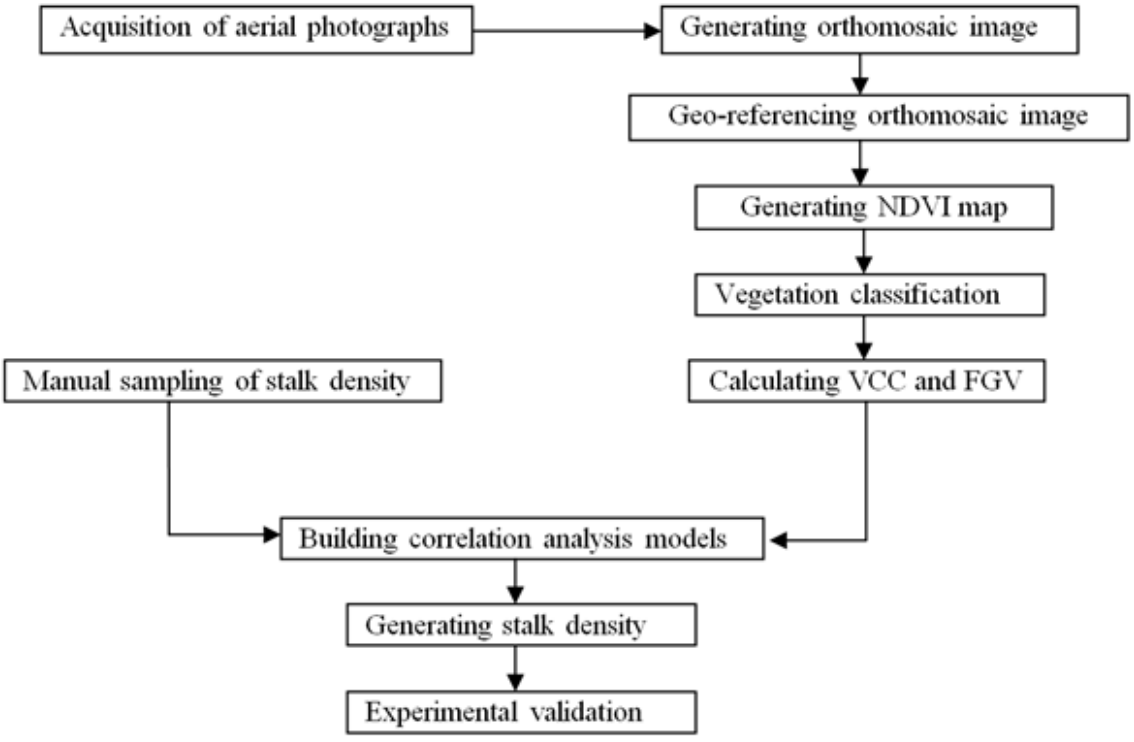

Fig.4. 2 Proposed approach of using UAV-camera system to estimate wheat stalk density

The overall approach of monitoring wheat canopy development and estimating stalk densities of wheat field from aerial photographs consists of three key steps: acquiring and post-processing aerial photographs with high spatial resolution using the low-altitude UAV-camera system; calculating Fractional Green Vegetation (FGV) and Vertical Canopy Coverage (VCC) out of the post-processed aerial image; and building regression models between samples of stalk density and the corresponding FGV and VCC values for the selection and validation of the most accurate estimation model, as shown in Fig.4. 2. This study adopted World Geodetic System 1984, or WGS84, as the coordinate system for geo-referenced images, maps, or any coordinates used in this paper if not particularly indicated.

4.2.1 Field Site and Experiment Description

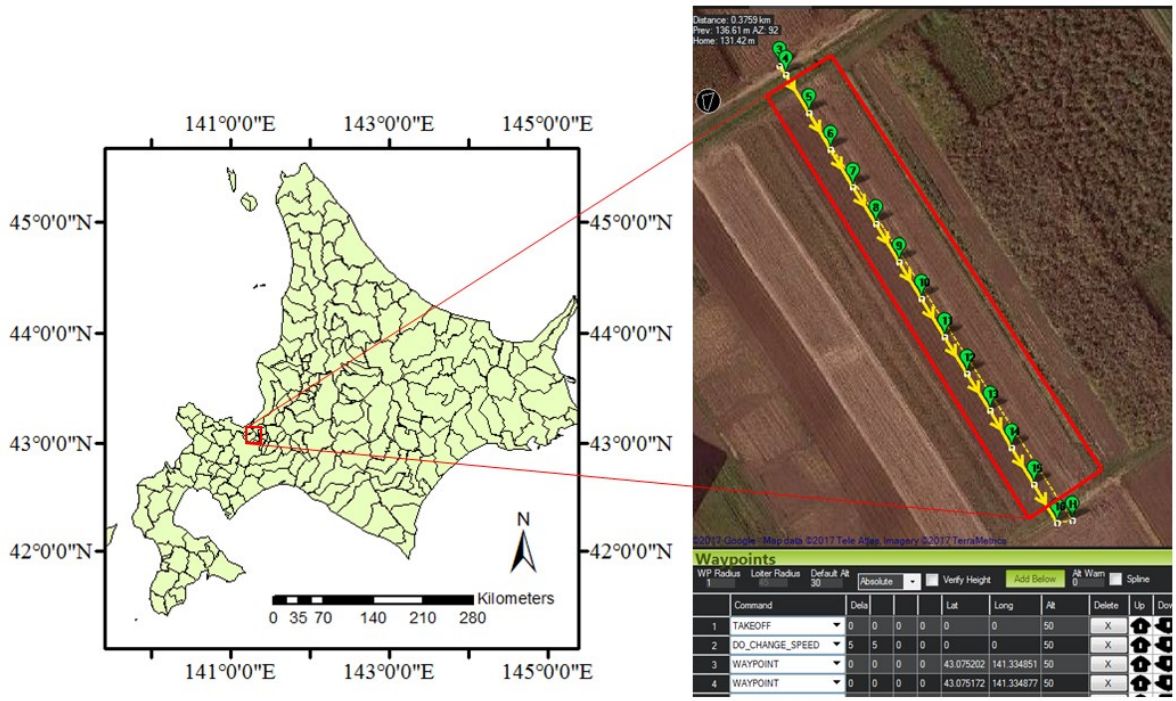

Fig.4. 3 Field site under study of estimating wheat stalk density

In this experiment, the same hexa-copter ZION CH940, described in Sec. 2.2.1, was used as the UAV-camera platform. A laptop installed with the GCS software was used to monitor and control the UAV's flight through telemetry radio. The experiment was established on 17 May 2016 on a winter wheat farmland of Hokkaido Univ., Sapporo, Japan over the vicinity of 43.075499°N and 141.334546°E, shown in Fig.4. 3 marked with red lines. The test field was approximately 0.25 ha, and a Japanese wheat variety of Kitahonami was planted on 24 September 2015, with the seeding rate of 60 kg/ha and uniform basal dressing of 500 kg/ha (BB082CR, a slow-release fertilizer). On 7 June, 15 June, and 21 June 2% foliar fertilizing of

urea solution was carried out since fertilization during these growth stages increases protein concentration in grain and further increases number of stalks on a single stem to maximize the yield. The regional annual precipitation is around 1100 mm, with average annual temperature of 8.9°C [77].

Digital camera uses either silicon-based charge-coupled detectors or complementary metal-oxide-semiconductors (CMOS) as the image sensors, both of which have high spectral sensitivity of visible and NIR portions of the spectrum ranging from about 350 nm to about 1100 nm wavelength [78]. By using a Bayer-pattern array of filters, most digital cameras obtain visible lights of red, green and blue bands for a digital image; however, since Bayer-pattern filters transmit significant amounts of NIR light through either blue, green or red channels, almost all commercial digital cameras have an internal filter blocking NIR light [79]. After removing NIR-blocking filter and conducting extensive post-calibration, it allows the raw digital camera image to be converted into a NIR false-color image to detect reflected NIR reflectance from vegetation.

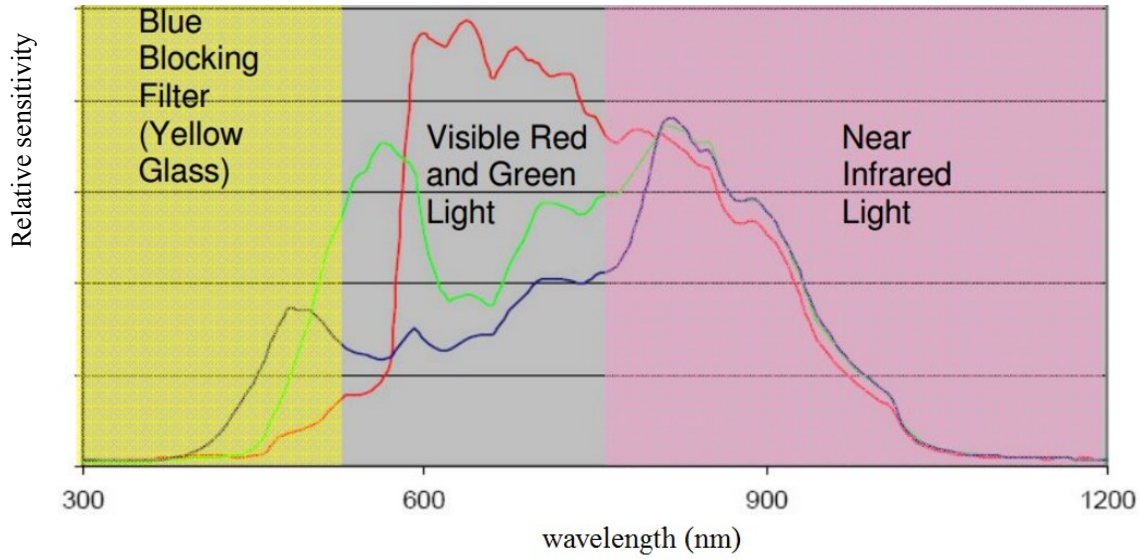

Fig.4. 4 ADC's spectral response

In this UAV-camera system, a Tetracam Inc. (Chatsworth, Canada) agricultural digital camera with an 8.5 mm lens was used for taking aerial pictures, which was set as continuous mode of every two seconds with fixed exposure. The ADC contains a single 3.2 megapixel CMOS image sensor (sensor dimensions: 6.55 * 4.92 mm) and is optimized for capturing visible light wavelengths longer than 520 nm and NIR light wavelengths up to 920 nm. By using a blue absorbing filter to eliminate the blue sensibility in a checkerboard pattern, the

ADC captures a separated red, green and NIR band of wavelengths, shown in Fig.4. 4. The ADC weighs about 640 g and was installed on a two-axis gimbal fixed downwards below the UAV platform to compensate for the vibration during the flight. When the picture was taken at the altitude of about 50 m above ground level in the vertical photographing fashion, each image covers 35 m horizontally and 25 m along the path with high spatial resolution of about 2 cm, shown in Fig.4. 5. From the image shown in false color manner we can clearly distinguish the vegetation (shown in red color) from the background of soil. The flight path was shown in Fig.4. 3 and totally 45 images were obtained covering the whole farmland. In consideration of the flight speed of 5 m/s, overlap rate among each image could be calculated as about 80%, which allows for conducting high precision image stitching in order to generate an ortho-mosaic image.

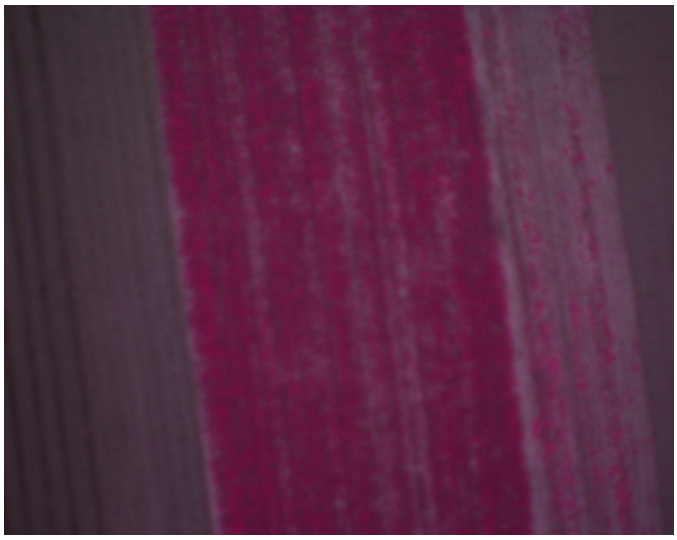

Fig.4. 5 Green-red-NIR false-color image of the field under study

4.2.2 Sampling of Stalk Density and Image Post-Processing

Table 4. 1 Sampled stalk density and the corresponding FGV and VCC

Sample ID	Latitude	Longitude	Stalk Density	FGV	VCC (Thresholding)	VCC (SVM)
1	43.07396	141.336014	690	0.52	0.99	0.74
2	43.07404	141.336031	400	0.43	0.97	0.46
3	43.07408	141.335921	660	0.52	0.99	0.74
4	43.07413	141.335869	620	0.52	1.00	0.67
5	43.07417	141.335898	490	0.47	0.98	0.53
6	43.07428	141.335735	850	0.58	1.00	0.80
7	43.07438	141.335647	800	0.54	1.00	0.78

8	43.07439	141.335719	560	0.49	1.00	0.56
9	43.07450	141.335636	290	0.45	0.96	0.39
10	43.07454	141.335496	710	0.53	0.97	0.69
11	43.07475	141.335321	570	0.53	0.99	0.66
12	43.07475	141.335407	680	0.52	1.00	0.78
13	43.07484	141.335250	660	0.53	0.99	0.74
14	43.07497	141.335123	720	0.51	1.00	0.79
15	43.07509	141.335155	200	0.39	0.91	0.32

In this study, experiment of calculating stalk density by manual sampling was conducted, so that the correlation of conventionally sampled stalk density values with the UAV remote sensing data could be studied and the actual spatial-varying information of wheat growth status could be obtained in a less time-consuming manner. Since row width in the experimental farmland was 50 cm, each stalk was counted within 80 cm along the row on which more than 3 leaves has already sprouted. By multiplying the number of counted stalks by 10 times and according to Eq. (4.1), each sample's stalk density per square meter can be calculated. Totally 15 samples distributed around the wheat field were taken as training data on 18 May 2016. These samples were selected after detailed visual inspection during field survey on the sampling day, in order to representatively choose 5 samples from most greenery areas and another 5 samples from sparse vegetated areas, whilst the rest 5 samples from normal developed areas. And the spatial distribution of these samples was shown in Fig.4. 7 as green dots. These samples' geo-spatial coordinates of latitude and longitude were measured by using the same RTK-GPS module described in Sec.3.2.2. The sampled stalk densities as well as the geo-spatial coordinates were listed in Table 4. 1.

There are generally two main image processing techniques for combining two or more individual images that are featured with a certain overlapping rate into a larger one: image stitching and ortho-mosaicking. Image stitching glues a small set of images together only under the circumstances of perfectly flat terrain by extracting a small number of key-points (feature points) out of the overlapped part of each individual image; whilst ortho-mosaicking is capable for all types of terrains and can handle a large set of overlapping images by ortho-rectifying the perspective distortions using an intermediary DSM, which needs a very large number of key-points. Recent advancements in aerial photogrammetry produced several image processing algorithms and software packages that are capable of generating ortho-mosaic images in a highly automated fashion. Structure from Motion (SfM) is one of the most widely used algorithms for ortho-mosaic image generation, which accurately estimates camera orientation as well internal parameters by tracking the locations of the detected key-

points from image to image. SfM typically utilizes scale invariant feature transform to detect and locate distinctive features as key-points using a difference-of-Gaussian function; and then it matches the key-points from different images based on the minimization of Euclidian distance, shown in Fig.4. 6; finally it produces a dense point cloud for the construction of a 3D representation of the scene.

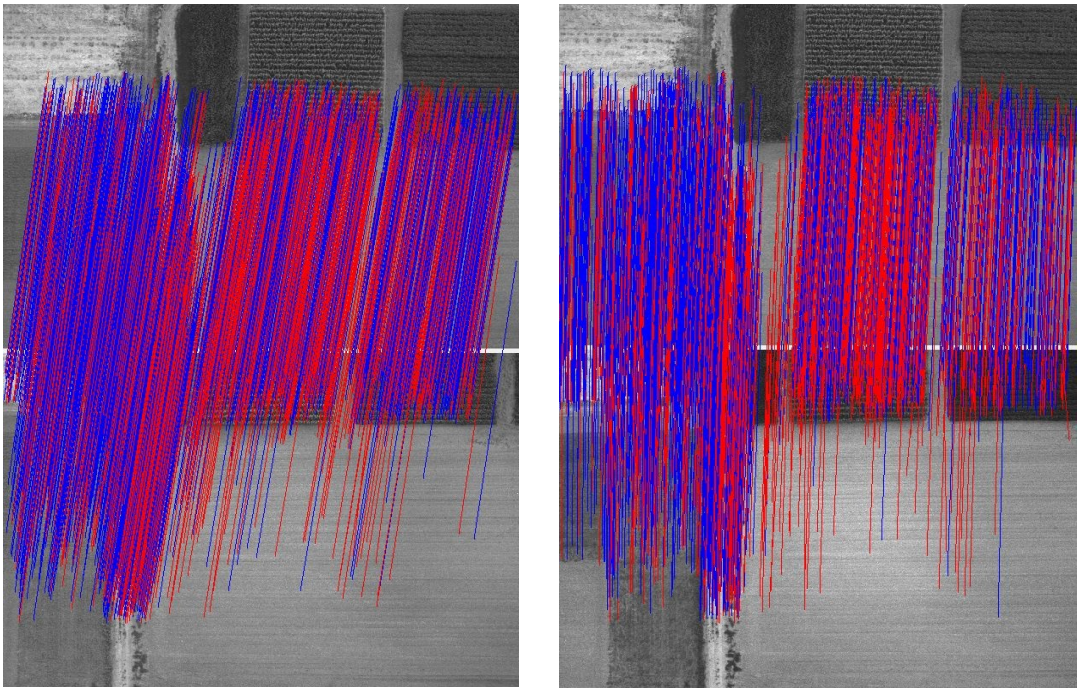

Fig.4. 6 Matching keypoins for generating an Ortho-mosaic image

45 individual aerial photographs were stitched together as one ortho-mosaic image by using Agisoft Photoscan software based on SfM algorithm and multi-view image processing techniques, which was shown in Fig.4. 7 in false-color manner. The ortho-mosaic image had 2387 * 8953 pixels in size, and the ground resolution reached up to 2 cm. Then geo-referencing was conducted, which is the process of assigning geographic coordinates to the dataset (usually an image file) that is spatial in nature but has no explicit geographic coordinates, for example aerial photographs. It is necessary to geo-reference such images and thereafter could be further studied in GIS applications. The geo-referencing process of the ortho-mosaic image was accomplished in ArcMap software, by using the 1st order polynomial transformation method and taking four wheat field corners as GCPs, listed in Table 4. 2. The transformation creates two least-square-fit equations by comparing the image space coordinates of the GCPs with the geographic coordinates and translates the image

coordinates of each pixel into geographic coordinates, which were measured by using Trimble SPS855 GNSS modular receiver in RTK-GPS mode, described in Sec.3.2.2.

Table 4. 2 GCPs' image space coordinates and geographic coordinates

GCP No.	Image space coordinates		Geographic coordinates	
	x	y	Latitude	Longitude
1	0.504395	11.925819	43.07517494	141.33511796
2	-1.081309	12.077644	43.07510077	141.33496042
3	-0.321990	-3.931718	43.07394452	141.33618863
4	-1.945205	-3.890796	43.07386295	141.33603152

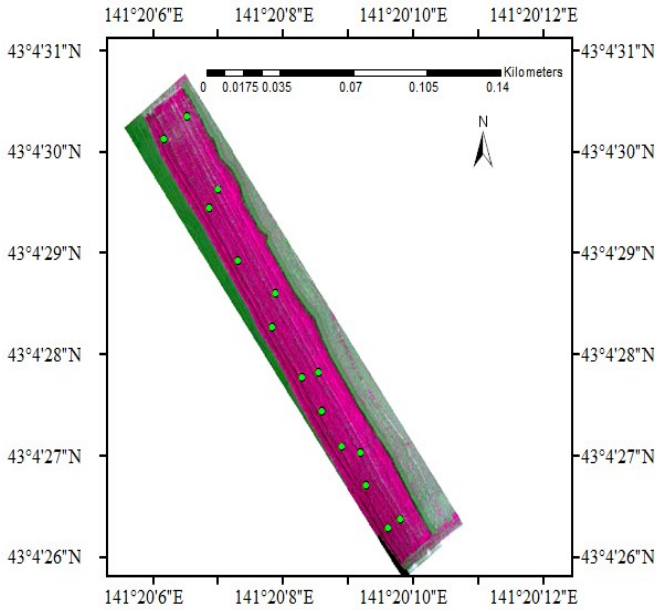

Fig.4. 7 Ortho-mosaic image of the wheat field shown in green-red-NIR false-color

Vegetation index map refers to as a scalar image, in which each pixel has only one single brightness value, and the pixel values are often calculated from reflectance or radiance of specific bands of remote sensing images. Normalized Difference Vegetation Index, known as NDVI, is one of the most popular indicators to quantitatively identify vegetated areas, estimate crop yields, and even to quantify the photosynthetic capacity of plant canopies since 1970s [80], [81]. NDVI is defined as the difference ratio between the spectral reflectance intensity of NIR waveband and red waveband acquired from various kinds of remote sensing data [82], described in Eq. (4.2). From the mathematical definition we may understand that the value of NDVI varies between negative 1.0 to positive 1.0. In general the NDVI of an area dominated by a dense vegetative canopy usually turns out to be positive values due to

plants' high-reflective and high-absorptive characteristics in NIR waveband and red waveband, respectively; whilst the NDVI of other targets such like standing water or clouds tends to be negative values, and cultivated soil is likely to display a low positive NDVI value. In this study, NDVI map was generated by using ENVI software (Exelis VIS, Inc., Colorado, US), in which the value of each pixel was determined from its existing multi-band pixel values of the geo-referenced ortho-mosaic image according to Eq. (4.2) by using band math functions, shown in Fig.4. 8.

$$NDVI = (\rho_{NIR} - \rho_{red})/(\rho_{NIR} + \rho_{red}) \tag{4.2}$$

where ρ_{NIR} and ρ_{red} denotes the spectral reflectance of NIR and red wavebands of the remote sensing data, respectively.

4.2.3 Calculating FGV and VCC

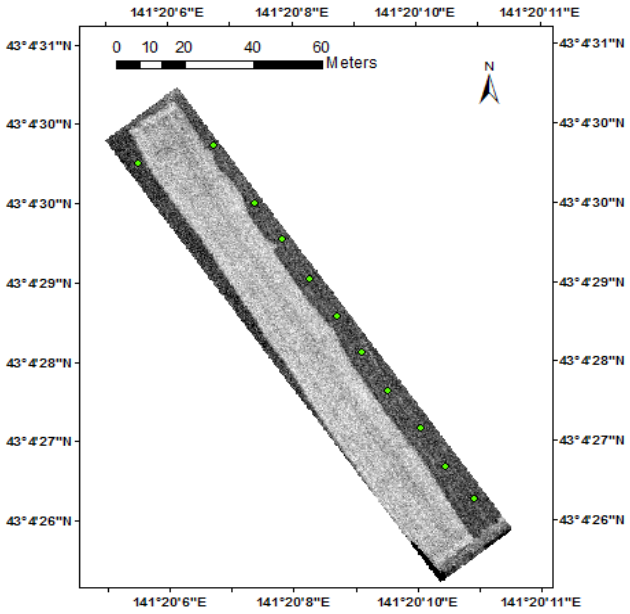

Fig.4. 8 NDVI map

In order to obtain accurate and comprehensive stalk density estimation of a wheat field by using UAV remote sensing images, it is necessary to correlate the post-processed aerial images with the manually sampled stalk densities. NDVI value is very sensitive to soil condition (moisture, organic contents, and etc.), shading effects caused by solar illumination and camera geometry; besides, NDVI is reported to be liable to saturate and is not suitable for distinguishing between different levels of vegetation coverage rate over high vegetation coverage areas. Thus, NDVI could not be directly related to the vegetation density by using

quantitative analysis model. In this study, we introduced two intermediate variables that are calculated out of the NDVI map shown in Fig.4. 8, for building correlation analysis models with the sampled wheat stalk density values.

One is the FGV, which represents the spatial density of live vegetation and calculated from the NDVI value of each pixel of interest, taking the NDVI values of bare soil and full vegetation as reference according to Eq. (4.3) [84]. In this study, $NDVI_s$ is determined by averaging the NDVI pixel values of ten bare soil samples that distributed along the field boundary, shown as bright green dots in Fig.4. 8. The sampled NDVI values of bare soil were listed in Table 4. 3, and $NDVI_s$ was accordingly calculated as 0.17. On the other hand, $NDVI_v$ is determined by extracting the maximum value of the NDVI map as 0.56. Subsequently, the FGV map was generated in ENVI software according to Eq. (4.3) by using band math functions. Finally a mean filter with the kernel size of 49 * 49 was created and applied to the FGV map, so that the averaged FGV value of the pixels within an area of about 1 square meter could be extracted according to the corresponding geographical coordinates of the manually sampled stalk densities, listed in Table 4. 1.

$$FGV = (NDVI - NDVI_s)/(NDVI_v - NDVI_s) \tag{4.3}$$

where $NDVI$, $NDVI_s$, and $NDVI_v$ is the NDVI value of each pixel of interest, the NDVI value of bare soil, and the NDVI value of full vegetation, respectively.

Table 4. 3 NDVI values of bare soil

Sample ID	Latitude	Longitude	NDVI Value
1	43.075005	141.334998	0.18
2	43.075052	141.335270	0.24
3	43.074785	141. 335512	0.16
4	43.074784	141.335512	0.18
5	43.074671	141.335612	0.16
6	43.074570	141.335709	0.12
7	43.074469	141.335790	0.16
8	43.074362	141.335887	0.15
9	43.074258	141.336005	0.22
10	43.074144	141.336099	0.17

The other one is the VCC, which is commonly acknowledged as an important indicator of crop vitality and expressed as the proportion of ground areas that are covered by vertical projection of crop canopies against total areas of interest, shown in Eq. (3.4) [85], [86]. In

order to calculate VCC out of a remote sensing image, image segmentation has to be conducted in the first place so that the vegetation pixels could be separated from the soil, or the background pixels. Image thresholding is the most straightforward and efficient method of segmenting bimodal grayscale images. If the pixel value is larger than the thresholding value, it would be assigned with one value (usually as 1); whilst if the pixel value is smaller than the thresholding value, it could be assigned with another value (usually as 0). However, if the bimodal characteristic of the grayscale image is not so obvious that a clear thresholding value could not be easily determined, the binarizing result could be very unsatisfactory.

The histogram of the NDVI map of the wheat field under study was shown in Fig.4. 9, and we may conclude that the first peak value of the NDVI map comes around 0.2, representing the pixel values of bare soil; whilst the second peak value is around 0.38, representing pixel values of vegetation. The thresholding pixel value between the soil class and the vegetation class seems to be extending from 0.26 to 0.3, and we assign the thresholding value as 0.28 for the image segmentation process from the interpretation of the NDVI map's histogram. The image segmentation result was shown in Fig.4. 10, from which we can visualize the differentiation between the bright white pixels (vegetation) and the black pixels (background), and thus calculate the proportion of vegetation pixels according to Eq. (4.4). A 1 m * 1 m grid was overlapped upon the resulting image segmentation map and the number of vegetation pixels was acquired through statistics of each grid of interest. The VCC values that share the same geographical coordinates with the corresponding manual stalk density samples were accordingly calculated and also listed in Table 4. 1.

$$VCC = N_v/N_t \tag{4.4}$$

where N_v denotes the number of pixels that are classified as vegetation, whilst N_t denotes the total number of pixels within a unit area (N_t=2500 in this study).

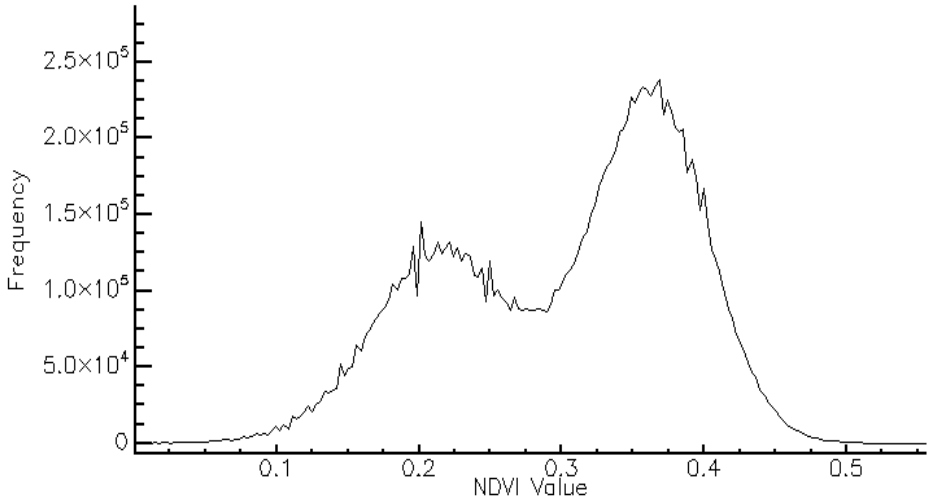

Fig.4. 9 Histogram of NDVI map

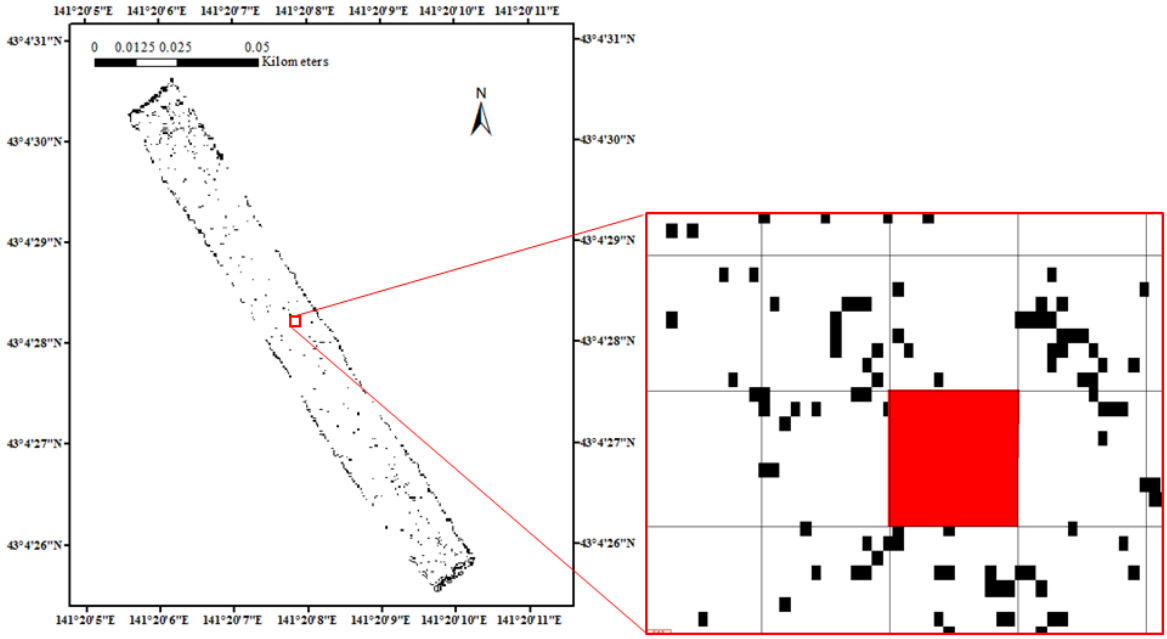

Fig.4. 10 Image segmentation result using thresholding method

In consideration that the spatial resolution of the aerial image reaches up to 2 cm and there might be plentiful vegetation-background fixed pixels among the pixels of vegetation and the pixels of soil, an indirect image segmentation method was also utilized to differentiate vegetation pixels from non-vegetation pixels. Support Vector Machine (SVM) classification is a supervised machine learning method among many others such as minimum distance, maximum likelihood, spectral angle mapper, and neural network, which is derived from statistical learning theory and used for building model of classification, regression, and

outlier detection by separating the classes with a decision surface that maximizes the margin between the classes [87].

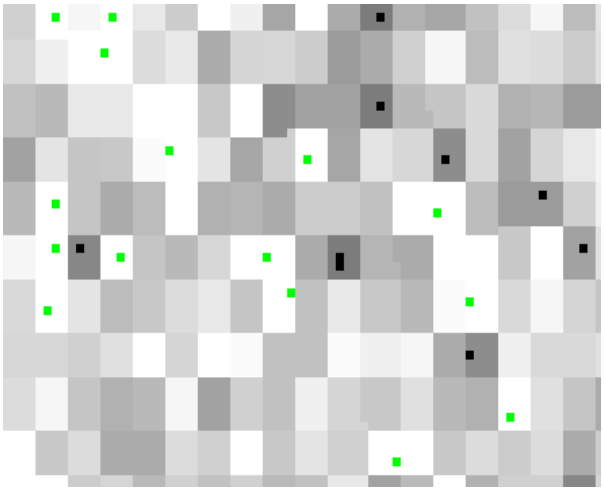

Fig.4. 11 Training dataset of SVM classification (in part)

The supervised classification based on SVM technique was conducted by using region of interest function in ENVI software, which was shown in Fig.4. 11. Training datasets of 200 pixels of vegetation (or highly vegetated pixels, marked with green color in Fig.4. 11) and 200 pixels of background (marked with black color in Fig.4. 11) were manually specified from the NDVI map, respectively. The training dataset spread all around the wheat field under study, and the pixels with values larger than 0.4 were assigned as vegetation class whilst the pixels with values smaller than 0.15 were assigned as non-vegetation class. Thus, each pixel of the NDVI map was classified either to the class of vegetation or to the class of non-vegetation according to the SVM classifier, as SVM algorithm separates the classes with a flexible decision surface from a local neighborhood point of view. The classification result was shown in Fig.4. 12, in which green pixel represents vegetation whilst the black pixel represent the background. Confusion matrix was used in ENVI software to validate accuracy of the classification result by comparing with ground truth of 100 vegetation pixels manually selected by visual inspection, and the accuracy of the classification result was up to 97.9%. Subsequently, a 1 m * 1 m grid was also overlapped upon the resulting classification map and the number of vegetation pixels was acquired through statistics of each grid of interest the same as how we have dealt with the classification map of thresholding method. The VCC values that share the same geographical coordinates with the corresponding manual stalk density samples were accordingly calculated and also listed in Table 4. 1.

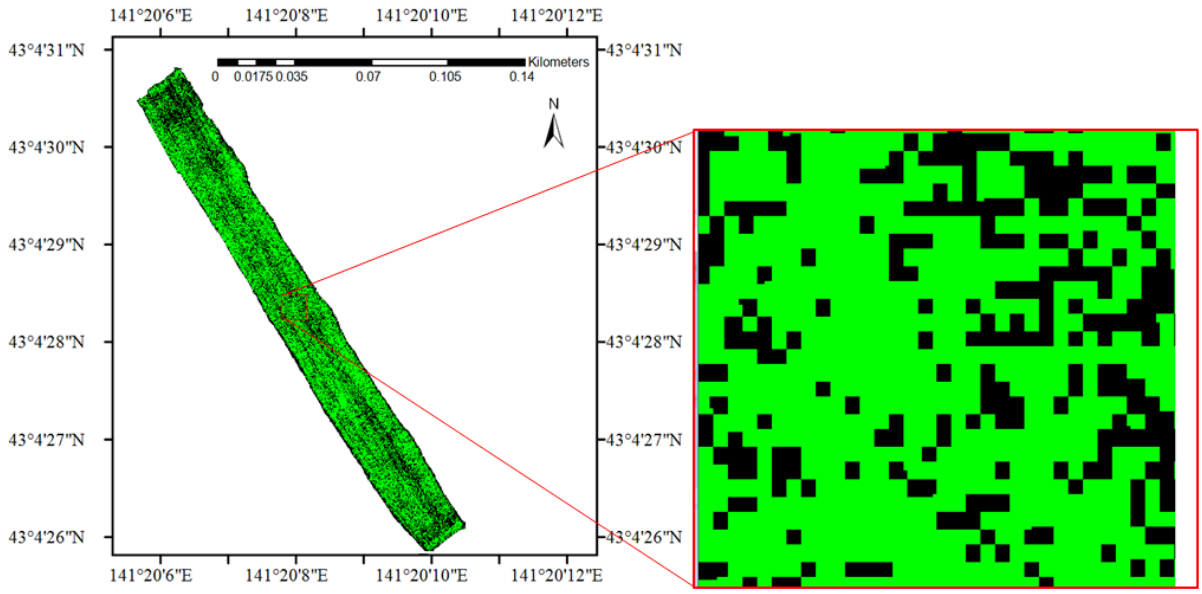

Fig.4. 12 Classification result using SVM method

4.3 Results and Discussion

4.3.1 Correlation Analysis between Sampled Stalk Density with FGV and VCC

From Table 4. 1 we may understand that VCC values based on the thresholding method vary from 0.91 to 1.00, which showed severe saturation due to high level of canopy coverage and is not suitable for building stalk density prediction model in this study. Thus, correlation analysis between 15 stalk densities sampled by manual counting with the corresponding FGV and VCC based on SVM method was performed, respectively, by building regression models in Excel 2010 software (Microsoft Corporation, USA). Fig.4. 13 and Fig.4. 14 showed different regression models (linear, second-order polynomial, exponential, and power regression model) between FGV as well as VCC and the sampled stalk densities.

From the figures we may conclude that the regression models between the sampled stalk densities and FGV values have good accuracy with the coefficient of determination around 0.88; however, the independent variable of FGV has a very limited data range from about 0.4 to about 0.6, indicating that the capacity of FGV of distinguishing different levels of canopy coverage is rather weak. On the other hand, the regression models between the sampled stalk densities and VCC values have better accuracy with the coefficient of determination around 0.93. Besides, the independent variable of VCC has a long data range from about 0.3 to about 0.9, indicating that the capacity of VCC of distinguishing different levels of canopy coverage is stronger when compared to the variable of FGV. And we may conclude that VCC values

based on the supervised classification method using the SVM classifier is the most suitable variable for building regression models to estimate wheat stalk densities from the UAV remote sensing images.

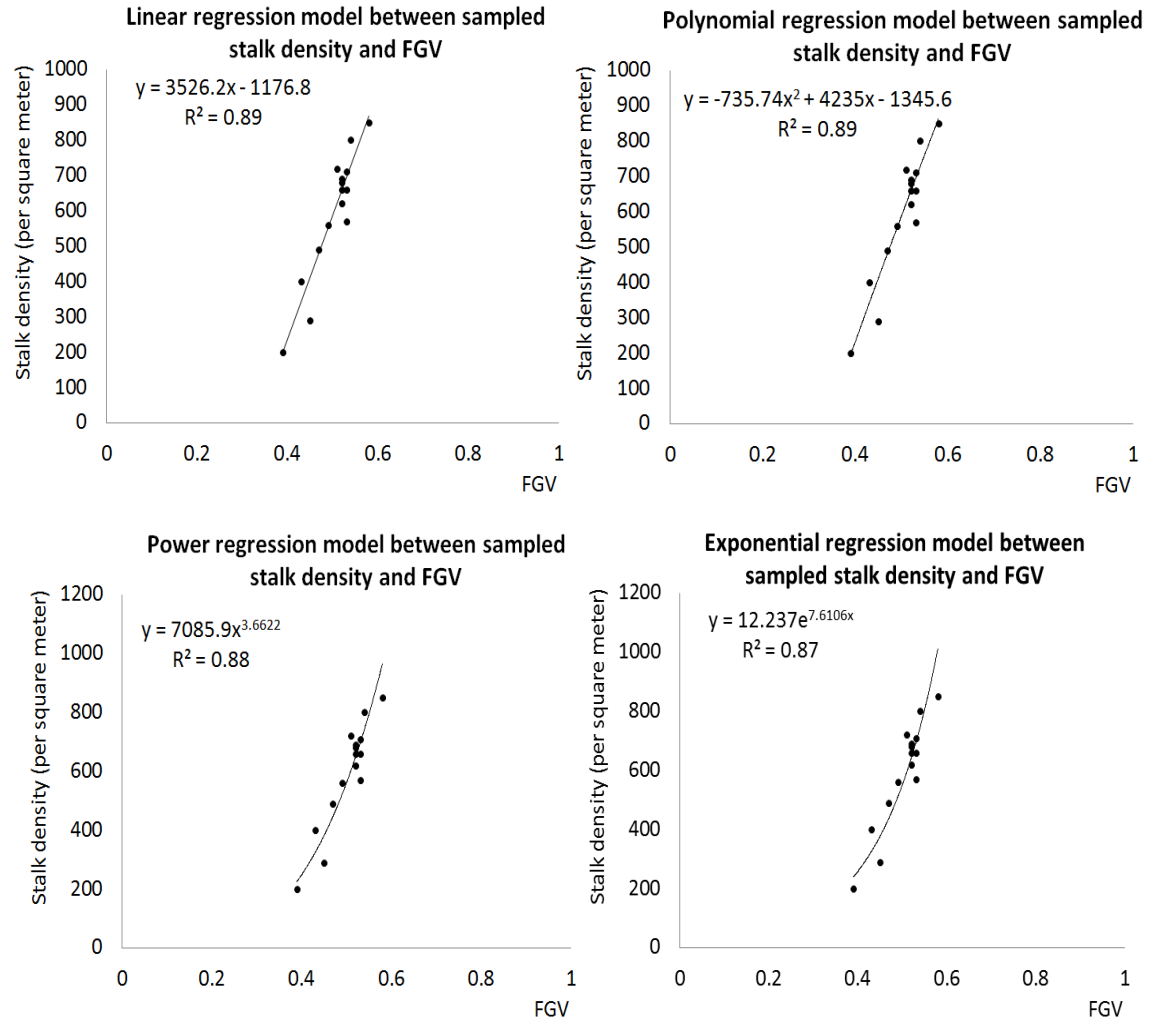

Fig.4. 13 Regression models between sampled stalk densities with FGV

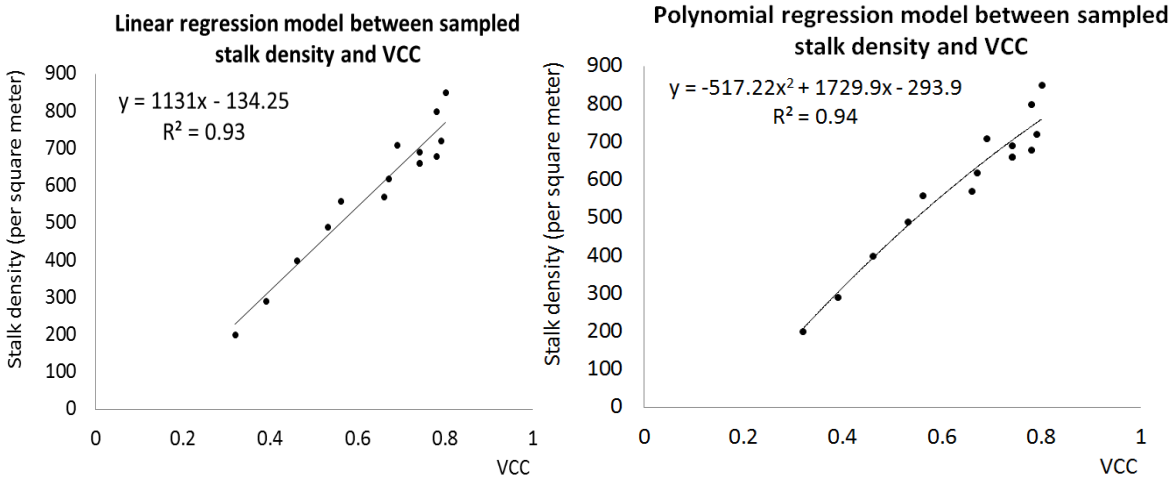

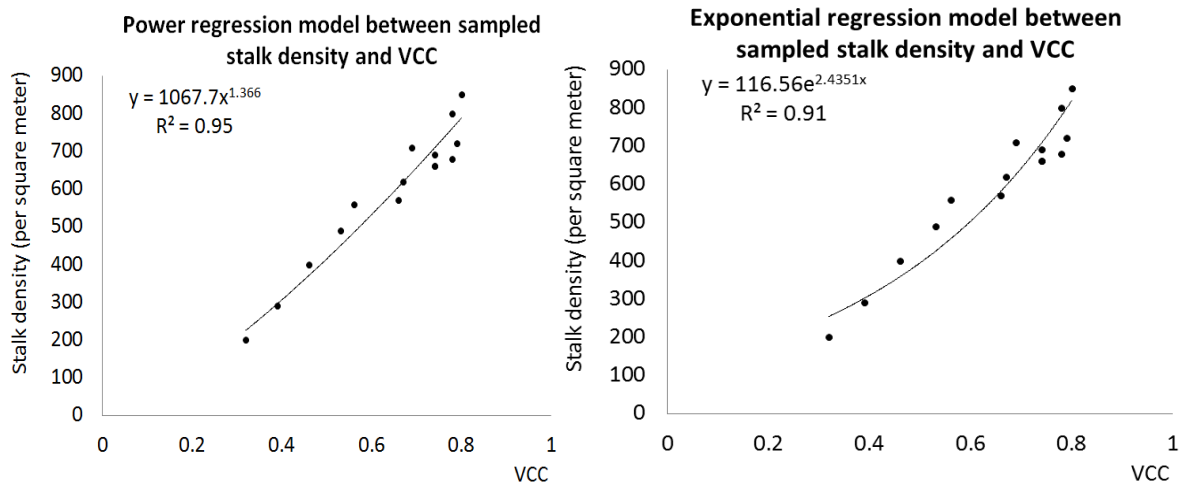

Fig.4. 14 Regression models between sampled stalk densities with VCC

By analyzing the coefficient of determination of four different kinds of regression models between VCC values and the sampled stalk densities, we may come to the conclusion that the response variable of stalk density related to the predicator variable of VCC with the highest coefficient of determination of 0.95 for power regression model, when compared with that of linear regression model, second-order polynomial regression model, and exponential regression model as 0.93, 0.94, and 0.91, respectively. And all of these four regression models have the same RMSE of 24, whilst the mean value of sampled stalk density was calculated as 593 from the 15 sampled stalk densities. Also, we concluded that around the VCC value of 0.8, stalk densities showed greater variation and more responsive to changes in VCC value.

Subsequently, leave-one-out cross-validation (LOOCV) [88] was also conducted by building 15 linear regression models, second-order polynomial regression models, exponential regression models, and power regression models, respectively, by using 14 set variables of sampled stalk densities and VCC as training data, whilst leaving one set of variables as test data for each regression model. Finally, root-mean-square error of prediction (RMSEP) [89] for linear regression model, second-order polynomial regression model, exponential regression model, and power regression model was calculated as 51, 54, 67, and 54, respectively. Taking both coefficient of determination of regression models and RMSEP of LOOCV models into consideration, power regression model was selected for estimating and mapping within-field spatial variations of stalk densities by using VCC values based on vegetation classification result of the UAV ortho-mosaic image.

4.3.2 Mapping within-Field Spatial Variations of Stalk Density

In order to obtain comprehensive information on overall wheat growth status and within-field spatial variations of stalk density for site-specific nitrogenous fertilizing, stalk density map of winter wheat was generating before nitrogenous topdressing operation at early growth stage. We originally validated a new approach of generating stalk density map by using green-red-NIR digital photographs from a low altitude UAV-camera system to extract VCC values and build regression models with sampled stalk densities, instead of conducting massive stalk counting manually, which is both time-consuming and apt to be affected by manual sampling error. In this study, 125 VCC values were randomly extracted out of the resulting vegetation classification map based on SVM classifier described in Sec.4.2.4, which spread all around the test field, shown in Fig.4. 15. According to the power regression model, estimated stalk densities for the 125 VCC samples were subsequently calculated.

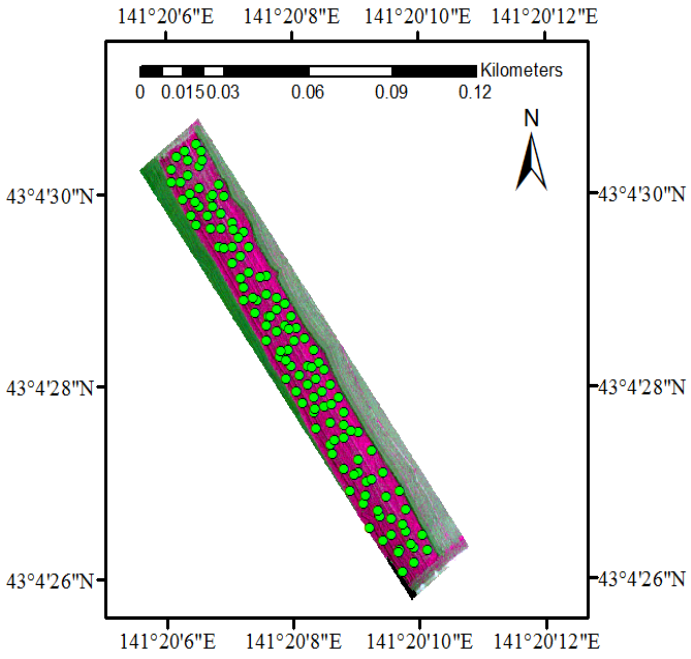

Fig.4. 15 VCC samples' spatial distribution used for generating stalk density map

Different stalk density maps for the wheat field under study were generated based on these calculated wheat stalk density samples by using TIN, IDW, Kriging, spline, and natural neighbor interpolation model, respectively. The interpolation models were explained in Sec.3.2.1, and the resulting stalk density maps were shown in Fig.4. 16. From the stalk density maps based on different interpolation methods we may conclude that stalk density maps based on the TIN, IDW, and natural neighbor interpolation method share the similar

general trend with the stalk density varying from about 40 to about 900 stalks per square meter, whilst stalk density maps based on the Kriging and spline interpolation model indicated unsuitable and inaccurate estimation of the within-field varying wheat stalk densities.

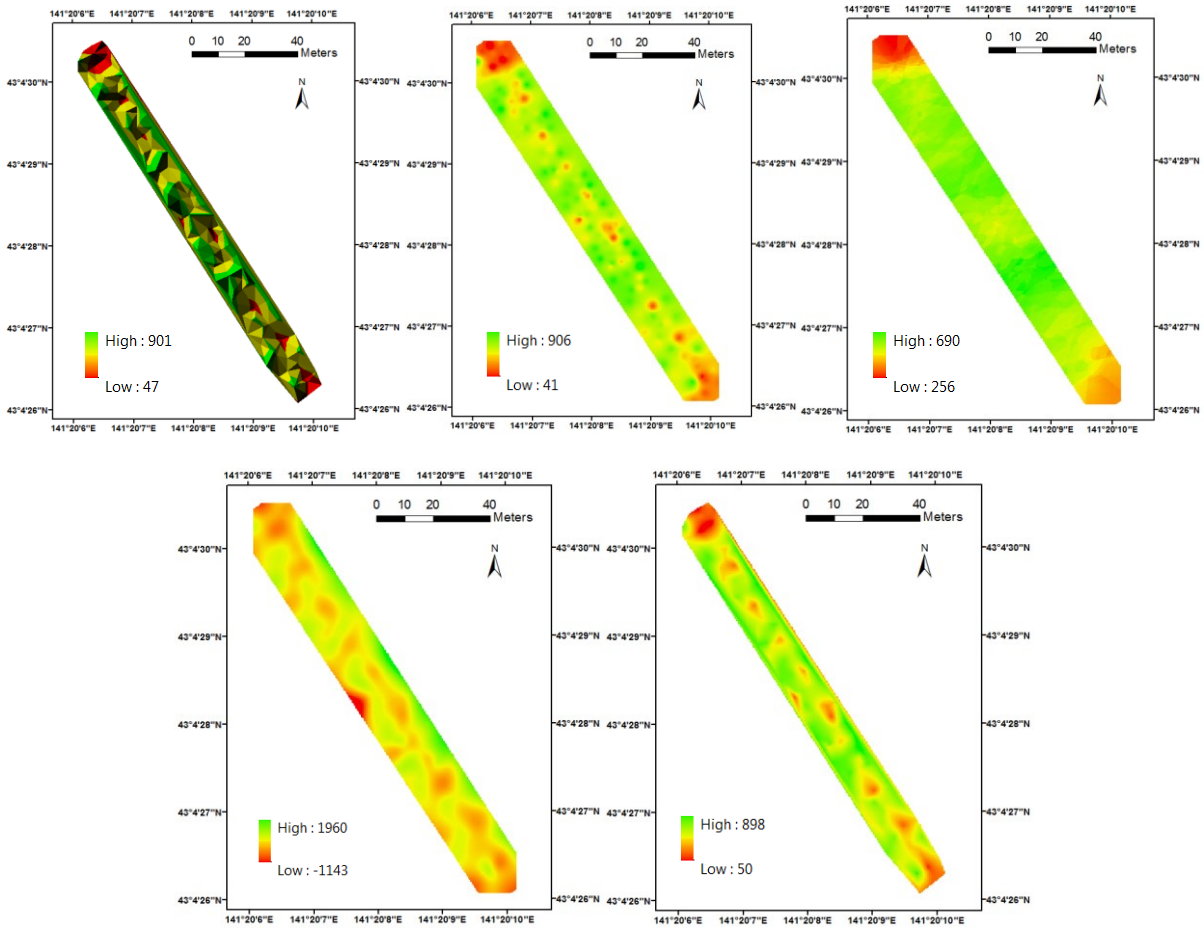

Fig.4. 16 Resulting stalk density maps based on TIN, IDW, Kriging (upper images from left to right), spline, and natural neighbor (bottom images from left to right) interpolation method

Table 4.4 Sampled stalk densities and estimated stalk densities based on different interpolation models

Sample ID	Latitude	Longitude	Sampled Stalk Density	Estimated Stalk Densities Based on Different Interpolation Models				
				TIN	IDW	Kriging	Spline	Natural Neighbor
1	43.07396	141.336014	690	693	711	416	686	693
2	43.07404	141.336031	400	377	369	463	364	370
3	43.07408	141.335921	660	702	696	524	679	660
4	43.07413	141.335869	620	605	616	567	618	605
5	43.07417	141.335898	490	439	451	539	439	454

6	43.07428	141.335735	850	735	780	655	777	754
7	43.07438	141.335647	800	573	729	652	721	652
8	43.07439	141.335719	560	504	486	652	476	496
9	43.07450	141.335636	290	318	303	539	282	295
10	43.07454	141.335496	710	634	636	538	637	617
11	43.07475	141.335321	570	592	604	584	592	595
12	43.07475	141.335407	680	722	770	584	768	756
13	43.07484	141.335250	660	674	705	575	707	697
14	43.07497	141.335123	720	760	757	577	775	765
15	43.07509	141.335155	200	233	222	280	241	241

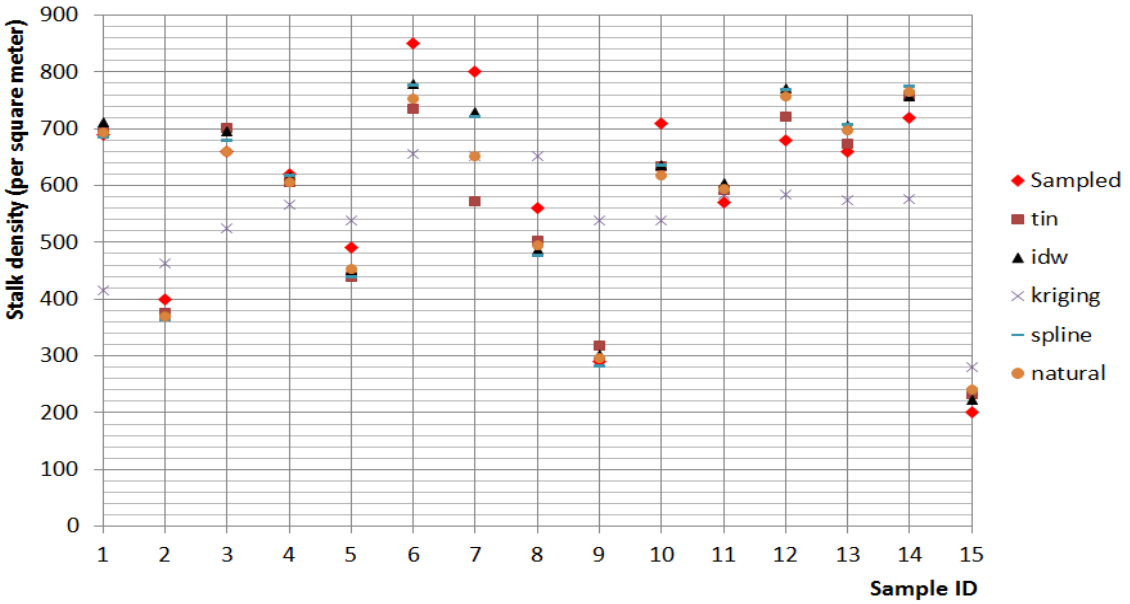

Fig.4. 17 Variation of estimated stalk densities based on different interpolation methods

Subsequently, estimated stalk density values were extracted from the resulting stalk density map based on different interpolation models according to the geographical coordinates of the manual samples. The accuracies were also confirmed by calculating RMSEs between the 15 manually sampled stalk density values and the corresponding estimated stalk density values extracted from each stalk density map based on TIN, IDW, and natural neighbor interpolation model, as 75, 51, and 62, respectively. For reference, the average value of the manually sampled stalk density was calculated as 593 stalks per square meter. By observing the variations of estimated stalk density based on different interpolation methods from Fig.4. 17, the stalk density map based on IDW interpolation model was selected to demonstrate the within-field spatial variation of wheat stalk density. From the IDW interpolation method based stalk density map we may conclude that the field under

study has a spatially varying stalk density ranging from 40 to 906 stalks per square meter. We can also understand that the headland of both sides has a relatively lower stalk density, and several low-stalk-density areas could also be spotted distributing all over the wheat field shown in red color.

$$RMSE_{stalkTIN} = \sqrt{\frac{\sum_{i=1}^{15}(S_{manuali} - S_{TINi})^2}{15}} \quad (4.5)$$

$$RMSE_{stalkIDW} = \sqrt{\frac{\sum_{i=1}^{15}(S_{manuali} - S_{IDWi})^2}{15}} \quad (4.6)$$

$$RMSE_{stalkNat} = \sqrt{\frac{\sum_{i=1}^{15}(S_{manuali} - S_{Nati})^2}{15}} \quad (4.7)$$

where $RMSE_{stalkTIN}$, $RMSE_{stalkIDW}$, and $RMSE_{stalkNat}$ is the root mean square error between the reference stalk density values by manual sampling and stalk density values extracted from the stalk density maps based on TIN interpolation model, IDW interpolation model, and natural neighbor interpolation model, respectively; whilst S_{manual}, S_{TIN}, S_{IDW}, and S_{Nat} the reference stalk density values by manual sampling and stalk density values extracted from the stalk density maps based on TIN interpolation model, IDW interpolation model, and natural neighbor interpolation model, respectively.

From the histogram of the stalk density map based on IDW interpolation method we obtained the information that the average value and standard deviation of the stalk density of the field was 554 and 136 stalks per square meter, respectively. About 12% acreages of the studied field have the stalk density ranging from 800 to 1000 stalks per square meter, which need low dose of nitrogenous topdressing such as 30 kg/10a ammonium sulfate; whilst about 22% acreages of the studied field have the stalk density ranging from 600 to 800 stalks per square meter, which need moderate dose of nitrogenous topdressing such as 40 kg/10a ammonium sulfate; and about 66% acreages of the field have the stalk density lower than 600 stalks per square meter, which desperately need high dose of nitrogenous topdressing such as 50 kg/10a or more ammonium sulfate for generating enough stalks before the end of tillering stage. There are no part of this field has the stalk density beyond 1500 stalks per square meter, indicating that there are no over-flourished canopies that would lead to the occurrence of lodging in later growth stage.

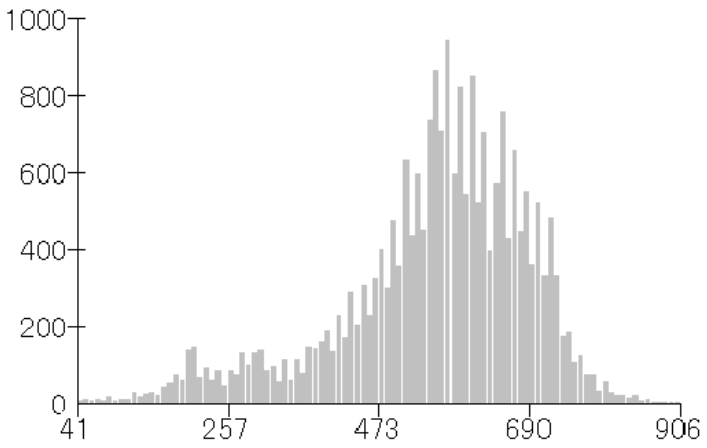

Fig.4. 18 Histogram of estimated stalk density map based on IDW interpolation method

4.4 Experimental Validation of the Stalk Density Estimation Model

Table 4. 5 Sampled stalk densities and the corresponding VCC values of validating experiment

Sample ID	Latitude	Longitude	Sampled Stalk Density	VCC (SVM)	Estimated Stalk Density
1	43.07486	141.334477	570	0.60	602
2	43.07482	141.334689	140	0.12	126
3	43.07468	141.334633	790	0.82	814
4	43.07459	141.334886	830	0.84	833
5	43.07449	141.334839	720	0.66	660
6	43.07444	141.334987	600	0.59	592
7	43.07435	141.334923	360	0.39	396
8	43.07437	141.335089	700	0.64	640
9	43.07421	141.335068	690	0.66	660
10	43.07426	141.335208	330	0.34	347
11	43.07409	141.335233	270	0.31	317
12	43.07414	141.335364	610	0.63	631
13	43.07393	141.335357	560	0.63	631
14	43.07391	141.335506	590	0.51	514
15	43.07381	141.335441	770	0.72	718

The validating experiment on the accuracy and repeatability of the stalk density estimation model was conducted for anther wheat field of the Hokkaido University on 20 May 2017. The test field was described in Sec.2.3.1 and shown in Fig.2. 9, where the topographic mapping experiment was conducted. The same wheat variety and seeding rate was applied with another wheat field of previous year that was described in Sec.4.2.1. 15 stalk densities were also manually sampled as ground truth and the geographical coordinates

of each sample was measured by using the same RTK-GPS module described in Sec.4.2.2. The spatial distribution of these stalk densities was shown in Fig.4. 19 as red dots, and the geographical coordinates as well as the stalk density values were listed in Table 4. 5. Similarly, each 200 vegetation pixels and background pixels were selected from the resulting NDVI map with the ground resolution of about 2 cm as training data through visual inspection, respectively; and by means of the supervised classification method of SVM classifier, the VCC map of the wheat field was generated for the validating experiment. The resulting VCC map was shown in Fig.4. 19, in which the green pixels represent vegetation class and the white pixels represent the background class. From the VCC map we may understand that the areas circled in red color have no sign of vegetation, as the wheat plants over there were drowned in the snowmelt water during the early April due to the relatively low ground elevation, also discussed in Sec.3.3.2.

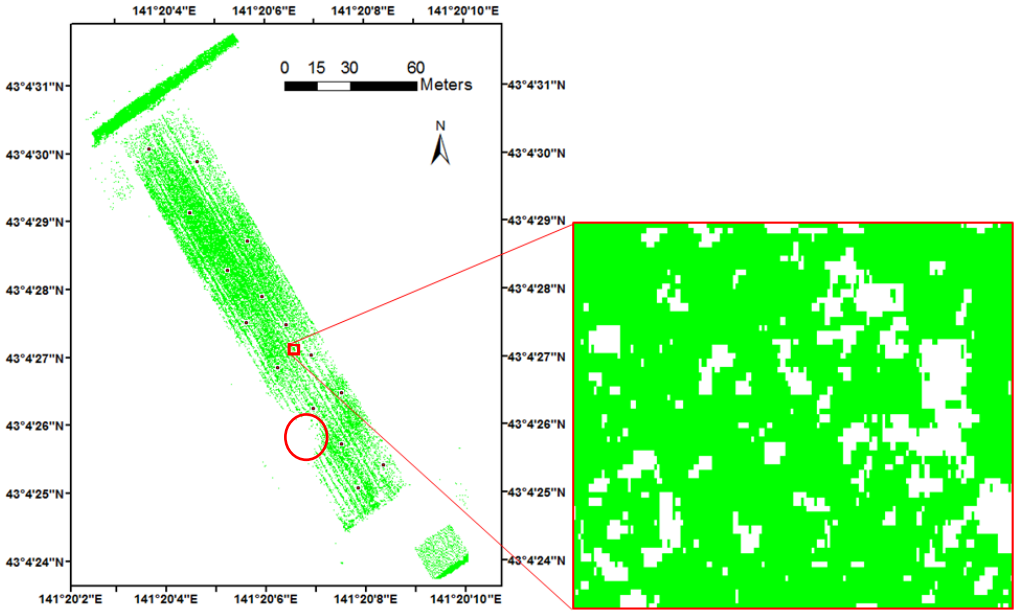

Fig.4. 19 Vegetation classification result of wheat field for validating experiment

VCC values of the areas that share the same geographical coordinates with each corresponding manually sampled stalk density were subsequently obtained and also listed in Table 4. 5. Different regression models between the manually sampled stalk density values with the corresponding VCC values were built, as shown in Fig.4. 20, from which we can come to the conclusion that power regression model with the coefficient of determination of

0.97 is still the most accurate one for estimating wheat stalk density by using the calculated VCC values.

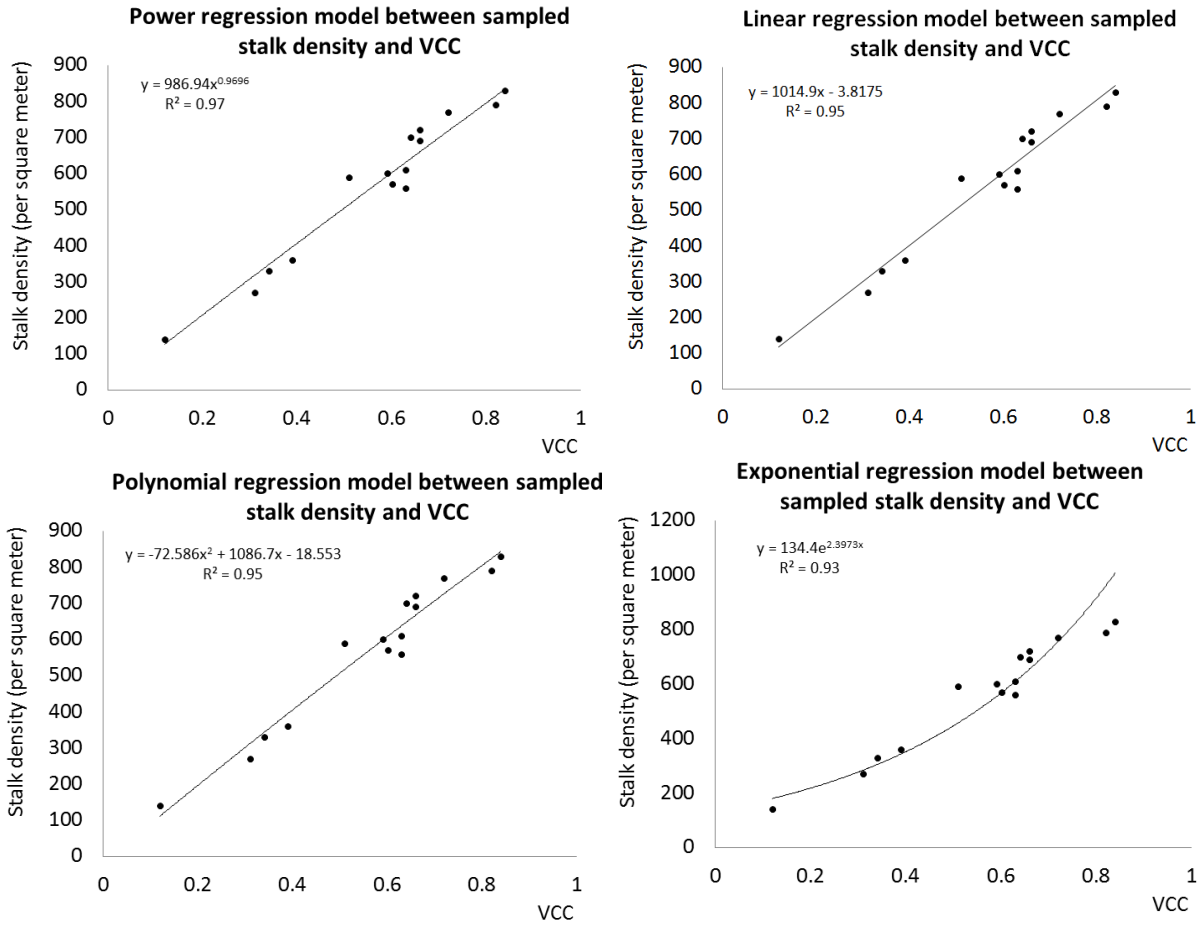

Fig.4. 20 Regression models between sampled stalk densities with VCC for validating experiment

Finally, 125 VCC values were extracted from Fig.4. 19 that randomly distributed all around the field under study; and the corresponding stalk densities were estimated from the power regression model; then, the stalk density map was generated by using these 125 estimated stalk density samples based on the IDW interpolation method, shown in Fig.4. 21. From Fig.4. 21 we can see that the south part of the field has a relatively lower stalk density, and in consideration of the topographic map shown in Fig.3. 16 we may conclude that plentiful and stagnant snowmelt water is harmful to the survival and development of wheat plant, which might led to the worst situation of total crop failure over the areas of relatively low ground elevation. The RMSE between the manually sampled stalk density values and each corresponding stalk density values that were extracted out of the resulting stalk density map based on the IDW interpolation model were calculated as 43 stalks per square meter,

which showed acceptable accuracy and practical feasibility in comparison with the average value of the manually sampled wheat stalk density of 569 stalks per square meter.

$$RMSE_{stalkVal} = \sqrt{\frac{\sum_{i=1}^{15}(S_{manualVali} - S_{Vali})^2}{15}} \quad (4.8)$$

where $RMSE_{stalkVal}$ is the root mean square error between the stalk density values by manual sampling and the stalk density values that were extracted out of the resulting stalk density map based on the IDW interpolation model; whilst $S_{manualVal}$, and S_{Val} is the reference stalk density values by manual sampling and the stalk density values that were extracted out of the resulting stalk density map based on the IDW interpolation model, respectively.

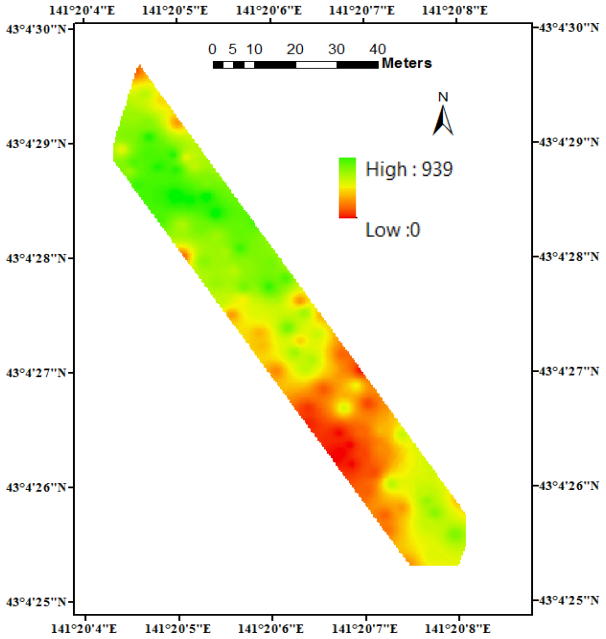

Fig.4. 21 Estimated stalk density map for validating experiment

From the histogram of the estimated stalk density map based on IDW interpolation method we obtained the information that the minimum and maximum stalk density value was 0 and 939 stalks per square meter, respectively, with the average value of 508 stalks per square meter. We may also understand that about 15% acreages of the studied field have the stalk density ranging from 800 to 1000 stalks per square meter, which need low dose of nitrogenous topdressing such as 30 kg/10a ammonium sulfate; whilst about 21% acreages of the studied field have the stalk density ranging from 600 to 800 stalks per square meter, which need moderate dose of nitrogenous topdressing such as 40 kg/10a ammonium sulfate;

and about 64% acreages of the field have the stalk density lower than 600 stalks per square meter, which desperately need high dose of nitrogenous topdressing such as 50 kg/10a or more ammonium sulfate for generating enough stalks before the end of tillering stage. There are no part of this field has the stalk density beyond 1500 stalks per square meter, indicating that there are no over-flourished canopies that would lead to the occurrence of lodging in later growth stage.

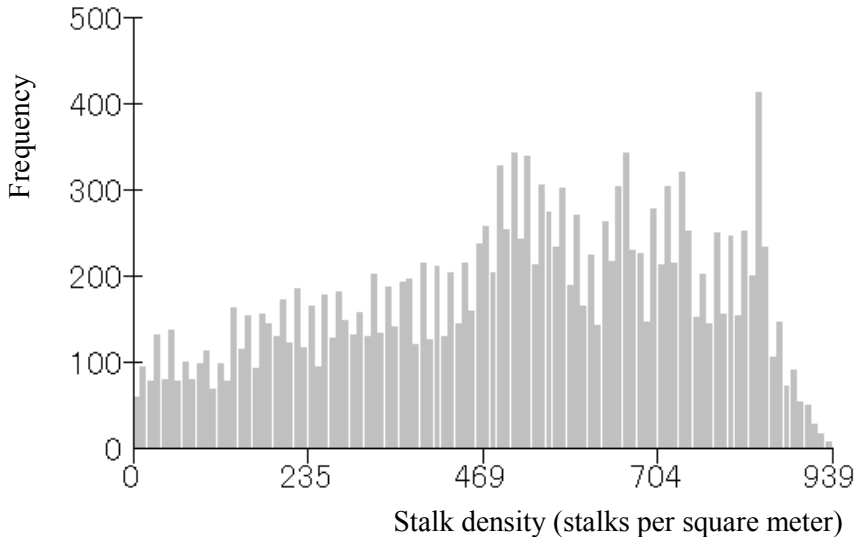

Fig.4. 22 Histogram of estimated stalk density map for validating experiment.

4.5 Conclusion

The novel approach of obtaining spatially-varied stalk density information of winter wheat at early growth stage by using UAV images and ground samples, which was described in this paper in detail, provides an accurate, time-and-cost efficient alternative of generating site-specific fertilizing prescription for precision agriculture. The aerial images were stitched as an ortho-mosaic image and further post-processed by geo-referencing. Subsequently map of normalized difference vegetation index (NDVI) was generated; then NDVI map was binarized as vegetation and background, and fractional green vegetation (FGV) as well as vertical canopy coverage (VCC) was calculated out of the binarization result. Finally regression models were built between the manually sampled stalk density values and the corresponding FGV and VCC values.

From the comparison of the extracted values of FGV, thresholding method based VCC, and support vector machine (SVM) classifier based VCC, we came to a conclusion that the

conventional thresholding method is the simplest image segmentation tool but not suitable for this study of estimating wheat stalk density from UAV remote sensing images, as the important thresholding value is usually not clear for segmenting the vegetation pixels from the non-vegetation pixels in aerial remote sensing images. The directly generated FGV values by determining NDVI value of the soil and the maximum NDVI value showed good correlation with the corresponding manually sampled stalk density values. Nevertheless, the FGV values concentrated to a very short range, indicating that the capability of distinguishing different levels of canopy coverage is limited. On the other hand, supervised classification based on SVM classifier needs massive human intervention by selecting training dataset from the NDVI map; however, VCC values extracted from the resulting classification map based on SVM classifier had a considerably wide range and the correlation with the corresponding manually sampled stalk density values is also very strong, due to the flexible decision surface of the SVM classifier that maximizes the margin between the vegetation class and the background class.

Based on the extracted FGV values as well as the SVM classifier based VCC values and the corresponding samples of stalk density acquired through manual counting, different kinds of regression models such as linear, second-order polynomial, exponential, and power regression models were built, respectively. And we may conclude that the regression models based on FGV values have good accuracy with the coefficient of determination around 0.89, and the regression models based on VCC values have better accuracy with the coefficient of determination around 0.94. Furthermore, we selected the power regression model between manually sampled stalk density values and the corresponding SVM classifier based VCC values for generating stalk density map for the wheat field under study, which has a high coefficient of determination of 0.95 and root-mean-square error of 24, in consideration that the average value of the manually sampled stalk density values was calculated as 593 stalks per square meter. The validating experiment on the other wheat field with the same seeding rate and similar field management treatment also confirmed that the power regression model is the most accurate and suitable model between the manually sampled stalk density values and the SVM classifier based VCC values. According to the power regression model between stalk density values and SVM classifier based VCC values, 125 stalk density values were calculated by extracting the corresponding VCC values from the resulting vegetation classification map based on SVM classification method. Subsequently, stalk density maps were generated out of the calculated stalk density values by using triangular irregular network,

inverse distance weight (IDW), spline, Kriging, and natural neighbor interpolation method, respectively. As the result, IDW interpolation method based stalk density map was selected to demonstrated stalk densities' within-field spatial variations and different rate of nitrogenous topdressing could be suggested accordingly.

In thus, we would like to conclude that the UAV-camera system used in this study could be used to obtain quantitative information for variable-rate topdressing in terms of site-specific or precision agriculture in an accurate and efficient manner. Also, the UAV-camera system presented here can be used for vegetation monitoring in various applications of determining plant cover or above-ground biomass estimation, and fulfil the need for remote sensing of high ground resolution imagery at low cost.

Chapter 5 Multi-temporal Monitoring of Wheat Growth Status and Mapping within-Field Variations of Wheat Yield

5.1 Introduction

In Chapter 4 we monitored wheat growth status during the early growth stage (tillering stage), and concluded that the low altitude UAV-camera system could be practically used as a powerful tool for quantitative analysis between wheat stalk density and remote sensing images. However, we cannot assert that the monitoring of wheat growth status is no longer needed after the tillering stage, as the field condition during the reproductive growth stages (booting stage, heading stage, flowering stage, dough development stage, and ripening stage) plays an even more important role in the yield formation, grain moisture content estimation, as well as the protein concentration. In order to optimize wheat yield and grain quality, especially in terms of protein content that varies significantly depending on different agricultural practices, wheat growers are expected to have a detailed understanding of wheat growth status during each specific development stage in wheat cultivation [90]. It implies that real-time monitoring of actual wheat growth status throughout the wheat growing season is of vital importance in helping wheat growers with management decision making. Meanwhile, it was frequently reported that reproductive growth of wheat after the flowering stage is closely related to grain yield, and many studies in recent years on wheat growth have indicated that accumulative vegetation index values of multi-temporal satellite remote sensing images after flowering stage have good relationship with crop yield [91]-[93]. Besides, Okuno studied on the wheat harvest support system by using satellite images during late-season of wheat growth stages in order to optimize harvest timing at regional scale, and generated a harvesting sequence map covering about 4000 ha [94]. And Han-ya and et al. investigated the correlation between the moisture content of wheat ear and the satellite and helicopter imagery, and accordingly reduced estimation error of moisture content [95].

Lodging, which usually occurs during wheat's ripening growth stage when ears fall over and rot on the ground, is another big concern especially for wheat growers in Hokkaido, Japan, as the storms and rainfalls usually coincide with the ripening process of winter wheat in the middle of July. Heavy nitrogenous fertilization makes wheat stalk grow taller and become more susceptible to this problem, and cautions are increasingly paid to the

application of nitrogenous fertilizers giving consideration to both desired wheat stalk density and the avoidance of heavy lodging situation. Adverse impacts of the occurrence of lodging in wheat field are tremendous. It not only affects the grain quality due to rot but also hinders the harvesting operation of combine harvester in the following aspects, as jam fault of combine harvester by the over-high humidity of the lodged wheat stalks is a typical failure. In the first place, the cutting process could be interrupted when the gap between moving blade and fixed blade is suffused by wheat stalks with high wetness. More likely, the threshing drum is apt to be entangled with the succulent wheat stalks; and as more and more wheat stalks stagnate upon the drum, it eventually gets stalled or even leads to the failure of the combine harvester's transmission system. Lastly, even if the wet wheat stalks successfully went through the cutting and threshing mechanisms of the combine harvester, it would inevitably "smuggle" plentiful grains by mixing and sheltering them from the sieves, which gives rise to extra yield loss [96], illustrated in Fig.5. 1. Since the "harvesting window" is usually very limited and we cannot afford wasting any moment in fixing or repairing the broken machine, the lodging situation of the wheat field is in desperate need before the harvesting operation so that drivers or the autonomous combine harvester could adjust working velocity accordingly.

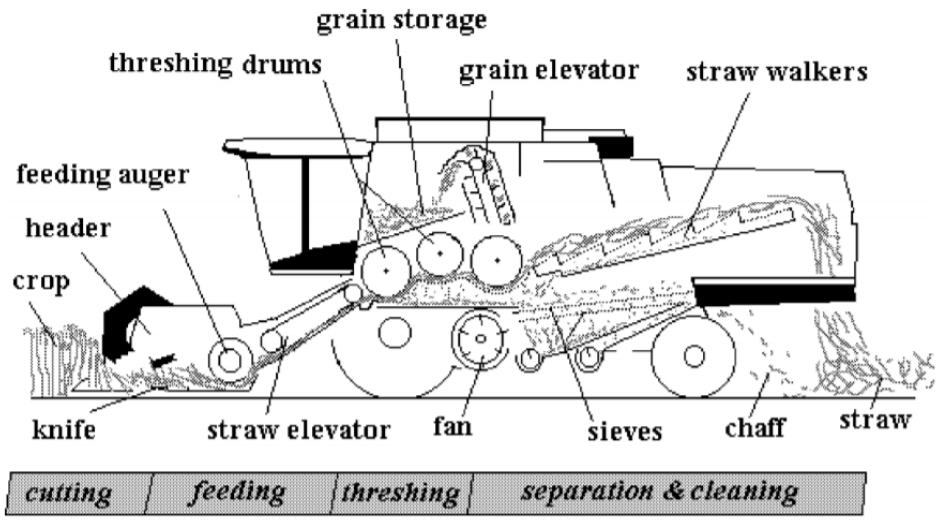

Fig.5. 1 Working principle of a combine harvester (Missotten, 1998)

As we have discussed in Sec.1.1.2 that satellite images can be regularly obtained at large scale, the ground resolution is yet inadequate for quantitative analysis that aims at demonstrating within-field variations. Besides, the minimum purchasing area of the satellite

images often starts from 2000 ha or so and it still increases if the ground resolution of the image gets more sparse. For example, the minimum purchasing area of WorldView satellite images with the ground resolution of about 50 cm is set as 2500 ha, whilst the minimum purchasing area of RapidEye satellite images with the ground resolution of about 5 m is set as 50 000 ha [97], [98]. For comparison, the average value of farmland area under cultivation per farmer was surveyed as 2.4 ha in the year of 2016 in Japan [99]. Using satellite images for multi-temporal monitoring of field condition and thus putting forward corresponding field management decisions seems neither particularly economical nor practical for both individual farmers and small farming-related organizations, not even to speak of the unavailability of a specific area due to cloud shadows, and etc.

In recent years, civilian applications of small UAVs have widespread from entertainment industry to professional photogrammetry, hazard survey, crop protection, and remote sensing, etc., as UAV image has increasing spatial resolution, may be acquired more cost-effectively and with excellent maneuverability as well as greater safety when compared with manned aircrafts [100]. Besides, agricultural application of UAV remote sensing by using commercial color cameras decreases high cost of remote sensing sharply and provides instantly researchers and farmers with actual and intuitive visualization of crop growth status, since color images accentuate particular vegetation greenness and have been suggested to be less sensitive to variations of illumination conditions [101]-[103]. Furthermore, several vegetation indices based on color images were proposed such as visible-band difference vegetation index (VDVI) [102], among other color vegetation indices of normalized green-red difference index (NGRDI) [104], normalized green-blue difference index (NGBDI) [105], and green-red ratio index (GRRI) [104], and excessive greenness (ExG) [105]. Woebbecke et al. tested several color indices derived by using chromatic coordinates and modified hue to distinguish vegetation from background such as bare soil and crop residues [105], among which ExG provides a near-binary intensity image outlining a plant region of interest has been widely cited. Wang and et al. [102] distinguished vegetative areas from non-vegetative areas by analyzing color images acquired from a UAV and found VDVI has the most precise capability of extracting vegetation areas in comparison with other vegetation indices of NGRDI, NGBDI, GRRI, and ExG. Rasmussen and et al. [76] investigated four different vegetation indices acquired from a color camera and a color-infrared camera by using both a fixed-wing and a rotary-wing UAV, and concluded that vegetation indices based on UAV's RGB image have the same ability to quantify crop responses with ground-based recordings.

Torres-Sánchez et al. mapped multi-temporal vegetation fraction in early-season wheat fields by using a UAV equipped with a commercial color camera and studied the influence of flight altitude and growing days after sowing on the classification accuracy, which showed that visible spectral vegetation indices derived from low-altitude UAV-camera system could be used as a suitable tool to discriminate vegetation in wheat fields in the early season [104]. Cui et al. evaluated the reliability of using color digital images to estimate above ground biomass at canopy level of winter wheat by taking pictures from one meter above the top of the wheat canopy [106]. In short, most past agricultural studies on color images focused on individual level of crop or weed, and the point-source samplings of which are usually inevitably both time-consuming and have to be conducted under poor working condition.

Therefore, in this study we monitored the time-varying canopy status of wheat through both the multispectral satellite images and also the UAV's RGB images. Subsequently, we investigated correlations between vegetation indices of UAV's RGB images and multispectral satellite images for future study of temporal complementation of these two different remote sensing systems. Correlation analysis between vegetation indices with sampled grain yield was also conducted, and the yield map that demonstrated the within-field spatial variations was generated accordingly.

5.2 Methodology

Four satellite images as well as eight UAV ortho-mosaic images during the late-season of wheat growth stages were utilized extending from the early June to the late July of 2015 for multi-temporally monitoring wheat growth status and mapping within-field variations of wheat yield. Firstly, UAV ortho-mosaic images were generated and geo-referenced to be aligned with satellite images; then different vegetation indices were extracted from each remote sensing images; subsequently, wheat growth status was monitored from both the multi-temporal remote sensing images and also the vegetation index maps; finally, within-field variations of yield was mapped according to the result of correlation analysis among the vegetation indices and ground samples of wheat yield.

5.2.1 Field Site and Remote Sensing Images

Experiments were established on two neighboring fields, which were planted with two different winter wheat varieties of Kitahonami and Yumechikara around 25 September 2014 and harvested on 27 July 2015. Fig.5. 2 showed the location of the investigated farmland in

Memuro, Hokkaido, Japan (around 42.902041°N–42.899607°N and 142.977953°E–142.981734°E). From weather data of 1981-2015 [106], regional annual precipitation, average annual temperature, and average accumulative annual duration of sunshine of this area is reported as 953.3 mm, 6.2°C, and 1939.6 h, respectively; whilst in 2015 annual precipitation, average annual temperature, and accumulative annual duration of sunshine of this area is reported as 828.5 mm, 7.0°C, and 2115.0 h, respectively. The lower left field No.1 (marked in black rectangle shown in Fig.5. 2) and upper right field No.2 (marked in red rectangle shown in Fig.5. 2) was planted with wheat variety of Kitahonami and Yumechikara, respectively. Each of these two fields occupies about 3.2 ha and 2 ha, of which the variety of Kitahonami is the most widely planted winter wheat variety in Japan and is reported to have taken up about 90% acreages of winter wheat in Hokkaido alone[108].

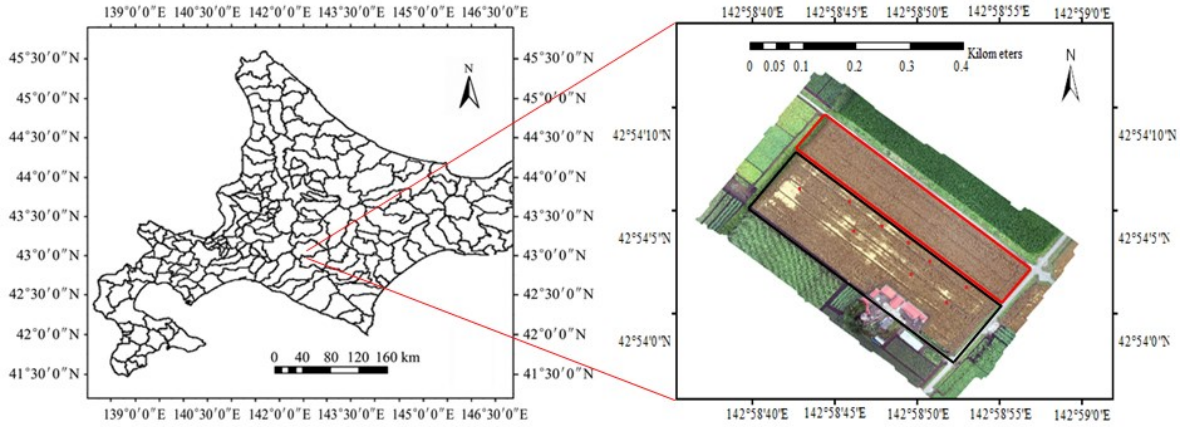

Fig.5. 2 Two neighboring wheat fields were studied planted with different winter wheat varieties

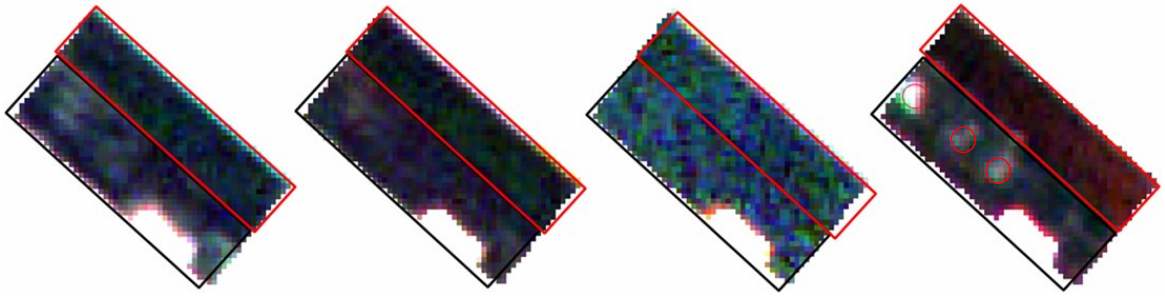

Fig.5. 3 Color change of wheat canopy shown by using satellite images in true color mode (Images taken on June 1, 7, 15, and July 17, 2015 were demonstrated in sequence from left to right)

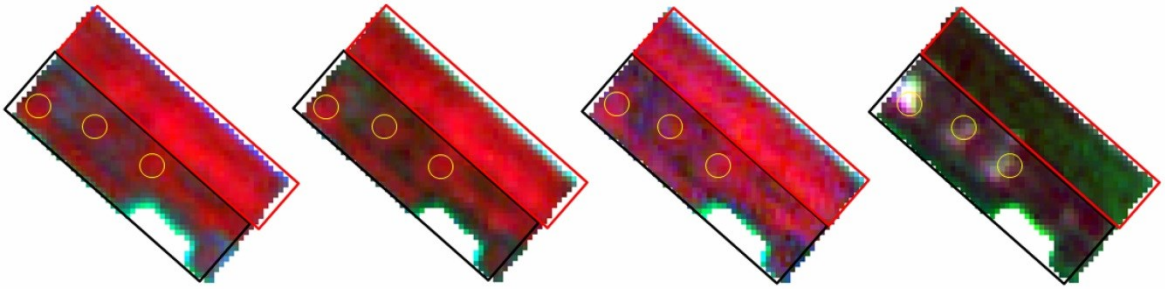

Fig.5. 4 Color change of wheat canopy was showed by using satellite images in standard false color mode (Images taken on June 1, 7, 15, and July 17, 2015 were demonstrated in sequence from left to right)

Four Rapideye satellite images taken on 1, 7, 15 June and 17 July 2015 were used in this study. Identical push-broom imaging sensors carried on each RapidEye satellite collect multispectral data of five spectral bands including blue (440-510 nm), green (520-590 nm), red (630-685 nm), red edge (690-730 nm), and near-infrared (760-850 nm) with 77 km swath width. During on-ground processing the remote sensing imagery is radiometrically calibrated and scaled to a 16 bit dynamic range, which converts the relative pixel digitalized number into values related with at sensor radiances by a radiometric scale factor of 0.01 [109]. High spatial resolution of 6.5 m of level 1B products and 5 m in terms of nadir ground sampling distance of the ortho-rectified ones is the another merit in consideration of the study on combination of satellite remote sensing images based vegetation indices with UAV's RGB images based vegetation indices.

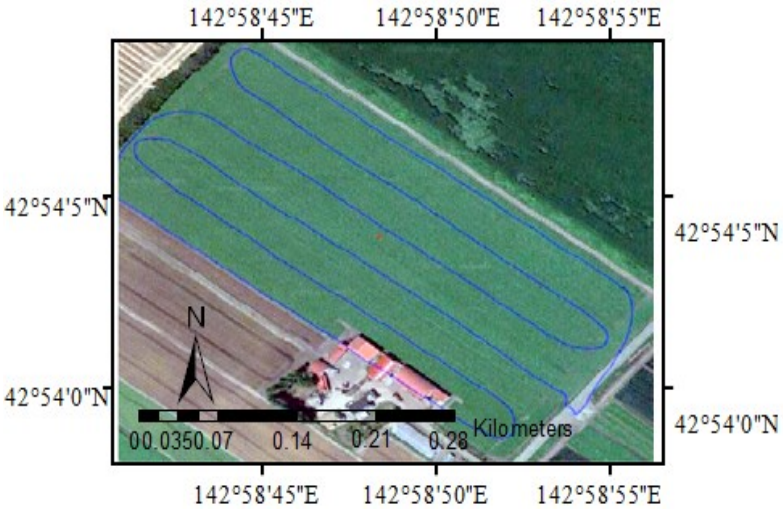

Fig.5. 5 UAV's flight path

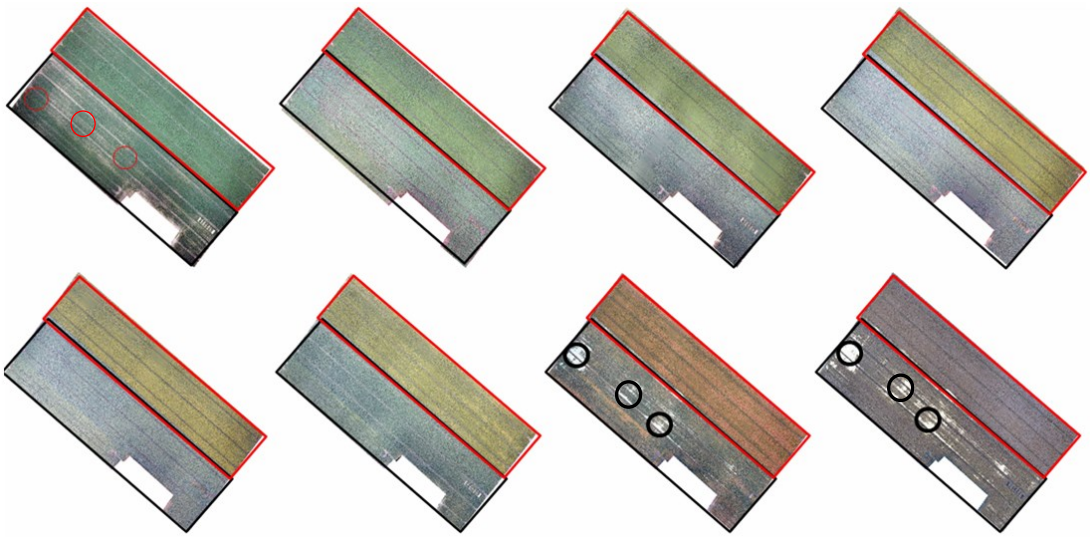

Fig.5. 6 UAV's RGB images from heading stage to harvesting (the upper four images from left to right were taken on June 2, 10, 19 and 25, and the lower four images from left to right were taken on July 2, 10, 16 and 24, 2015)

Since satellite remote sensing images' temporal frequencies and spatial resolution are not adequate to monitor rapidly changing wheat growth conditions, eight RGB images acquired from UAV were also taken from early June to the end of July 2015 covering two wheat fields at the interval of about one week. Autonomous flights were conducted eight times from winter wheat's heading stage to ripening stage, on 2, 10, 19, and 25 June, 2015, and 2, 10, 16, and 24 July 2015 (at about 11:00 local time), using the flight paths that were designed beforehand in the GCS software, shown in Fig.5. 5 as blue lines. A SONY ILCE-6000 commercial digital camera with the sensor size of 23.5 mm * 15.6 mm and the focal length of 16 mm was used to take pictures in continuous mode every two seconds (f/8, 1/500 sec, ISO 100). During each flight the camera was fixed on a two-axis gimbal, pointing vertically downwards and took about 120 photos covering two adjacent fields in order to get enough GCPs for geo-referencing. Every 120 individual photographs were stitched together as an Ortho-mosaic image by using Agisoft Photoscan software, which was shown in Fig.5. 6. Each of the Ortho-mosaic images has about 3600 * 2450 pixels in size, and the ground resolution reached up to about 12.5 cm after ortho-mosaicking. Geo-referencing of UAV ortho-mosaic images were accomplished using ArcMap software by using eight GCPs, which consist of headline corners, telegraph poles around the test field. First order polynomial transformation creates two least-square-fit equations by comparing the image space coordinates of the GCPs with the geographic coordinates (latitude and longitude) and translates image coordinates of each pixel into geographic coordinates. These GCPs' geo-

spatial coordinates were measured by using Trimble SPS855 GNSS modular receiver in RTK-GPS mode. And the result of UAV Ortho-mosaic image's geo-referencing was shown in Fig.5. 7 as geo-spatially overlaid upon a satellite image.

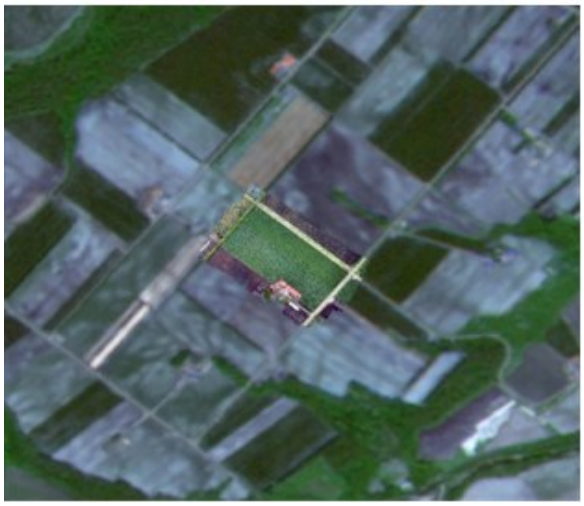

Fig.5. 7 Geo-referenced UAV's Ortho-mosaic image overlaid upon satellite image

5.2.2 Radiometric Normalization of Multi-temporal Remote Sensing Images

Due to variated atmospheric conditions, different illumination intensity, viewing angles, and etc., radiometric accuracy and consistency are difficult to maintain among multi-temporal remote sensing images. Different from absolute radiometric correction, which is usually based on radiative transfer models such as 6S [110], MODTRAN [111], and etc., relative radiometric correction or radiometric normalization was performed to adjust multi-temporal images to a set of reference data and compensate for the above effects. The reference data were generated by calculating the average values of each pseudo-invariant features' (PIF) pixel values, band by band, which refer to the ground objects of which the reflectance values are nearly constant over time during a certain period [112]. According to these PIFs' pixel values of each band and corresponding reference data, the radiometric normalization models of different dates' satellite images as well as UAV ortho-mosaic images, band by band, were obtained by building linear regression equations.

As to the satellite images, 38 crossroads and 2 flat grounds nearby construction sites, covering considerable large area around the experimental field, were selected as PIFs by visual inspection, marked as dark dots shown in Fig.5. 8. Forty PIFs' pixel values and the corresponding average values are listed in Table 5. 1, taking blue band as an example. 7

places along road as well as 5 places on roofs were chosen as PIFs in each UAV ortho-mosaic images, and around each PIF's location the average value of 6 pixels distributed within 1-meter-square were calculated so that the influence of abnormal values caused by foreign matters etc. could be decreased to the minimum. The spatial distribution of UAV Ortho-mosaic images' PIFs was also shown in Fig.5. 8.

Table 5. 1 PIFs' pixel values of satellite images (taking blue band as an example)

PIF ID	17 July	15 June	7 June	1 June	Average
1	8046	8827	8846	8775	8624
2	6161	7684	7229	7374	7112
3	6704	8107	7532	7477	7455
4	6478	7817	7035	7190	7130
5	7761	8605	7939	8083	8097
6	6726	7864	6685	7218	7123
7	5997	8042	6759	7606	7101
8	6613	8065	7328	7615	7405
9	6213	7927	7232	7191	7141
10	7288	8281	7694	8002	7816
11	6705	7998	7954	7636	7573
12	6624	8565	7128	6960	7319
13	6070	7720	6872	6914	6894
14	6766	8013	7288	7436	7376
15	6645	7937	7187	7497	7317
16	6466	8268	7561	7208	7376
17	7287	8070	7062	7773	7548
18	5889	7405	6327	6752	6593
19	6603	7869	7603	7946	7505
20	6950	7860	6739	7153	7176
21	6657	8023	7502	7040	7306
22	6991	8268	7957	7773	7747
23	6936	7948	7714	8023	7655
24	5561	7680	6668	7136	6761
25	6963	8212	7308	6926	7352
26	6326	7912	7509	7771	7380
27	5961	8014	6508	6863	6837
28	11228	9701	10003	11163	10524
29	6798	8116	7659	7940	7628
30	6720	8107	7937	7865	7657
31	6033	7551	6428	7059	6768
32	6214	7803	6605	7227	6962
33	6261	7855	6797	7574	7122
34	6997	8122	7267	7349	7434
35	12584	11324	12723	15994	13156
36	7938	8688	8278	8186	8273
37	6888	7979	7200	7651	7430
38	5933	7948	7271	7381	7133

39	6224	7996	6380	6791	6848
40	5801	7823	6446	7091	6790

Fig.5. 8 Spatial distribution PIFs in satellite image (left) and UAV Ortho-mosaic image (right)

Table 5. 2 Linear regression normalization models of satellites images

Image date	Band	Slope	Intercept	R-squared
1 June	Blue	0.72	1977.00	0.96
	Green	0.76	1419.83	0.98
	Red	0.81	830.67	0.97
	RE	0.80	917.50	0.98
	NIR	0.90	710.89	0.87
7 June	Blue	0.98	228.58	0.95
	Green	0.94	443.09	0.99
	Red	1.04	-306.32	0.96
	RE	1.00	-104.54	0.96
	NIR	0.83	1444.00	0.91
15 June	Blue	1.68	-6117.00	0.94
	Green	1.52	-3627.00	0.93
	Red	1.25	-993.83	0.89
	RE	1.24	-877.75	0.90
	NIR	0.98	-369.56	0.84
17 July	Blue	0.84	1817.00	0.95
	Green	0.90	962.98	0.94
	Red	0.83	1029.00	0.96
	RE	0.89	620.13	0.97
	NIR	0.80	169.00	0.86

Table 5.3 Linear regression normalization models of UAV images

Image date	Band	Slope	Intercept	R-squared
2 June	Blue	1.01	6.55	0.83
	Green	0.77	45.38	0.96
	Red	0.74	52.52	0.94
10 June	Blue	0.86	15.43	0.73
	Green	0.87	7.96	0.91
	Red	0.85	11.55	0.91
19 June	Blue	0.77	42.65	0.91
	Green	1.09	-15.09	0.94
	Red	1.10	-17.33	0.93
25 June	Blue	0.99	4.14	0.97
	Green	0.95	9.63	0.99
	Red	0.92	12.56	0.99
2 July	Blue	0.82	28.49	0.94
	Green	1.03	-13.48	0.98
	Red	1.03	-12.15	0.98
10 July	Blue	0.88	22.77	0.81
	Green	1.01	-2.42	0.94
	Red	1.06	-10.30	0.93
16 July	Blue	0.79	47.09	0.97
	Green	1.16	-15.27	0.98
	Red	1.16	-16.84	0.97
24 July	Blue	0.94	12.01	0.80
	Green	0.89	17.61	0.97
	Red	0.90	16.28	0.97

According to these PIFs' pixel values, radiometric normalization models of different dates' satellite images as well as UAV ortho-mosaic images, band by band, were built and shown in Table 5. 2 and Table 5.3, respectively. From the results of R-squared values we can see that the deviation of the satellite image on 15 June from the reference data is most significant, which means the atmospheric effects such as weather condition comparatively differ from other days. When considered from the viewpoint of the performances of each band, NIR band of the satellite images expressed worst correlation, and the other bands seemed to be correspondingly correlated better among these images, due to different spectral responsive characteristics. As to UAV ortho-mosaic images, conclusion could be drawn that the variation of blue band is most significant, whilst green band and red band expressed consistently higher relevance and less variation, indicating that blue band is more susceptible to influences of different photographing environment. And we can also conclude that the image of 10 June was taken under the most deviated photographing condition when

compared to other UAV ortho-mosaic images. And based on these linear regression models, each band of all images was radiometrically normalized to the reference data and the effects caused by the deviation of atmosphere condition could be compensated, so that we can ignore the disturbance of atmosphere and extract the real changes of crops in multi-temporal analysis.

5.2.3 Vegetation Indices of Remote Sensing Images

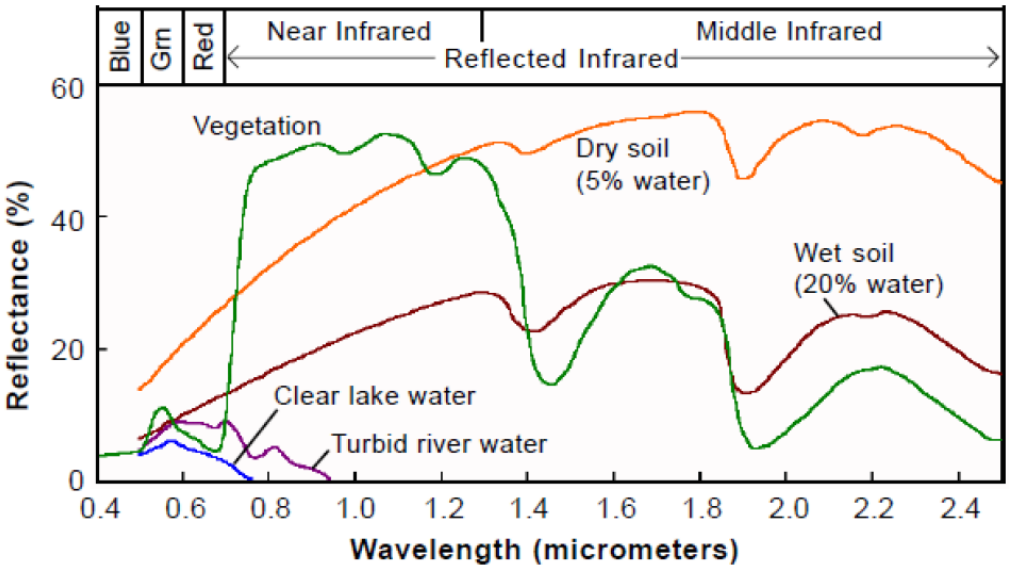

Fig.5. 9 Typical spectral signature of different features (Saba Daneshgar)

NDVI is the most well-known and widely used vegetation index to detect live plant canopies due to the high spectral reflectance of plants in the spectrum of NIR region. In recent years several vegetation indices that are different from the NDVI associated with NIR band were proposed based on high-resolution color remote sensing images, in order to identify vegetative features from background such as VDVI, NGRDI, NGBDI, GRRI, and ExG mentioned above in Sec.5.1, according to the typical spectral signature of different features shown in Fig.5. 9.

$$NDVI = (NIR - R_{sate})/(NIR + R_{sate}) \tag{5.1}$$

$$VDVI_{sate} = (2G_{sate} - R_{sate} - B_{sate})/(2G_{sate} + R_{sate} + B_{sate}) \tag{5.2}$$

$$VDVI = (2G_{UAV} - R_{UAV} - B_{UAV})/(2G_{UAV} + R_{UAV} + B_{UAV}) \tag{5.3}$$

$$NGRDI = (G_{UAV} - R_{UAV})/(G_{UAV} + R_{UAV}) \tag{5.4}$$

$$NGBDI = (G_{UAV} - B_{UAV})/(G_{UAV} + B_{UAV}) \quad (5.5)$$

$$GRRI = G_{UAV}/R_{UAV} \quad (5.6)$$

$$ExG = 2G_{UAV} - R_{UAV} - B_{UAV} \quad (5.7)$$

where NIR, R_{sate}, G_{sate} and B_{sate} is the radiometrically normalized pixel value of NIR band, red band, green band and blue band of satellite images, respectively; whilst G_{UAV}, R_{UAV}, and B_{UAV} is the radiometrically normalized pixel values of green band, red band and blue band of UAV's ortho-mosaic images, respectively.

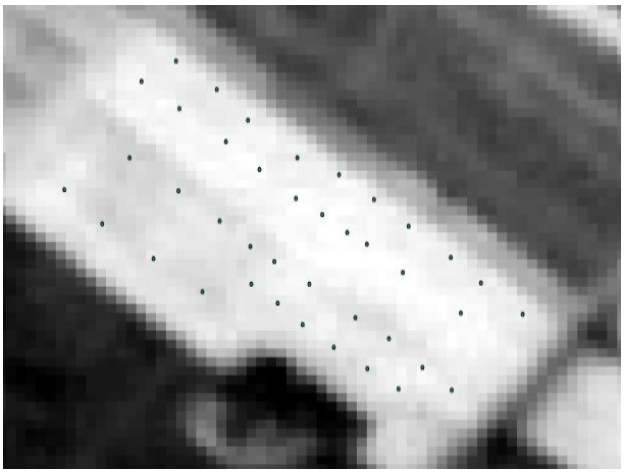

Fig.5. 10 Spatial distribution of vegetation indices

In this study, forty vegetation indices' samples (each twenty samples for field Kitahonami and Yumechikara, respectively) of NDVI as well as $VDVI_{sate}$ out of each satellite images were extracted respectively, listed in Table 5. 4. At the same sampling positions forty samples of VDVI were correspondingly extracted out of UAV's ortho-mosaic images for multi-temporal monitoring of wheat growth status as well as correlation analysis between vegetation indices based on these two different sources of remote sensing images, listed in Table 5.5. Mean filter of 39 * 39 kernels was applied to UAV's Ortho-mosaic image based VDVI maps so that noise signal of bare soil could be largely reduced and spatial resolution of UAV's ortho-mosaic images based VDVI map could be coordinated with satellite images based NDVI map as well as satellite images based VDVI map. Spatial distribution of forty vegetation indices samples is described in a NDVI map based on satellite image taken on June 15 2015 in Fig.5. 10.

Table 5. 4 Satellite images based vegetation indices

ID	Coordinates		NDVI				$VDVI_{sate}$			
	Latitude	Longitude	1 June	7 June	15 June	17 July	1 June	7 June	15 June	17 July
1	42.90233	142.9792	0.54	0.72	0.58	0.20	0.02	0.05	-0.01	-0.01
2	42.90219	142.9789	0.56	0.76	0.60	0.20	0.02	0.06	0.01	-0.02
3	42.90214	142.9795	0.52	0.72	0.57	0.18	0.02	0.06	0.00	0.00
4	42.90202	142.9792	0.56	0.76	0.59	0.22	0.02	0.07	0.01	0.01
5	42.90194	142.9798	0.55	0.75	0.57	0.18	0.03	0.06	-0.02	-0.02
6	42.9018	142.9796	0.58	0.77	0.60	0.17	0.03	0.09	0.01	0.00
7	42.90169	142.9788	0.44	0.62	0.52	0.21	0.02	0.04	0.00	0.01
8	42.90169	142.9802	0.55	0.73	0.58	0.18	0.02	0.07	0.03	-0.01
9	42.90162	142.9799	0.57	0.73	0.57	0.18	0.03	0.06	-0.03	-0.01
10	42.90158	142.9805	0.58	0.77	0.61	0.18	0.03	0.07	0.00	0.01
11	42.90148	142.9783	0.55	0.72	0.56	0.34	0.03	0.05	0.01	0.09
12	42.90148	142.9792	0.49	0.66	0.53	0.22	0.02	0.03	-0.02	0.02
13	42.90143	142.9802	0.57	0.74	0.57	0.16	0.02	0.07	-0.03	-0.01
14	42.90142	142.9808	0.60	0.78	0.61	0.16	0.04	0.09	0.00	0.00
15	42.90132	142.9804	0.61	0.79	0.61	0.17	0.04	0.07	-0.02	-0.01
16	42.90128	142.9796	0.47	0.64	0.52	0.20	0.01	0.03	0.01	0.02
17	42.90126	142.9786	0.56	0.73	0.60	0.16	0.02	0.06	-0.01	-0.01
18	42.90124	142.9811	0.51	0.69	0.56	0.24	0.02	0.04	0.00	-0.01
19	42.9012	142.9806	0.60	0.78	0.61	0.15	0.03	0.08	0.00	-0.03
20	42.90112	142.9807	0.59	0.76	0.61	0.14	0.03	0.08	-0.01	-0.01
21	42.90111	142.9798	0.47	0.68	0.54	0.20	0.02	0.05	-0.03	0.00
22	42.90104	142.9814	0.50	0.66	0.55	0.18	0.02	0.05	0.00	0.00
23	42.90103	142.979	0.53	0.72	0.59	0.23	0.02	0.04	-0.04	0.01
24	42.90101	142.98	0.55	0.74	0.58	0.13	0.02	0.05	-0.03	-0.02
25	42.90094	142.981	0.59	0.78	0.61	0.14	0.03	0.08	-0.03	-0.01
26	42.90087	142.9816	0.55	0.73	0.58	0.10	0.02	0.06	0.01	-0.02
27	42.90086	142.9803	0.52	0.70	0.56	0.22	0.03	0.05	-0.03	0.03
28	42.90086	142.9798	0.55	0.74	0.58	0.21	0.02	0.05	-0.04	0.01
29	42.90081	142.9794	0.46	0.62	0.51	0.16	0.01	0.03	-0.03	0.01
30	42.90074	142.98	0.51	0.73	0.56	0.26	0.01	0.07	-0.01	0.02
31	42.90067	142.9815	0.58	0.77	0.61	0.12	0.02	0.08	0.01	-0.02
32	42.90067	142.982	0.53	0.73	0.58	0.11	0.01	0.05	-0.03	-0.02
33	42.90064	142.9806	0.51	0.70	0.56	0.22	0.02	0.04	-0.06	-0.01
34	42.9006	142.9802	0.52	0.70	0.54	0.23	0.03	0.05	-0.03	0.02
35	42.9005	142.9809	0.53	0.71	0.56	0.24	0.03	0.05	-0.01	0.03
36	42.90045	142.9805	0.48	0.68	0.56	0.20	0.02	0.04	-0.05	0.02
37	42.90031	142.9812	0.49	0.67	0.54	0.22	0.02	0.05	-0.06	-0.01
38	42.90031	142.9807	0.56	0.74	0.60	0.25	0.02	0.07	-0.01	0.02
39	42.90017	142.981	0.53	0.71	0.56	0.26	0.02	0.05	0.01	0.03
40	42.90017	142.9814	0.48	0.67	0.54	0.18	0.02	0.04	-0.04	0.02

Table 5. 5 UAV ortho-mosaic images based VDVI

	Coordinates		Date							
ID	Latitude	Longitude	2 Jun.	10 Jun.	19 Jun.	25 Jun.	2 Jul.	10 Jul.	16 Jul.	24 Jul.
1	42.90233	142.9792	0.11	0.16	0.09	0.16	0.11	0.11	0.07	0.01
2	42.90219	142.9789	0.14	0.17	0.11	0.17	0.12	0.12	0.07	0.02
3	42.90214	142.9795	0.11	0.16	0.09	0.15	0.11	0.10	0.07	0.02
4	42.90202	142.9792	0.13	0.17	0.11	0.16	0.12	0.12	0.07	0.02
5	42.90194	142.9798	0.12	0.16	0.10	0.16	0.12	0.11	0.06	0.02
6	42.9018	142.9796	0.13	0.17	0.11	0.16	0.12	0.12	0.07	0.01
7	42.90169	142.9788	0.08	0.12	0.05	0.10	0.07	0.08	0.06	0.02
8	42.90169	142.9802	0.13	0.17	0.10	0.16	0.12	0.11	0.06	0.01
9	42.90162	142.9799	0.13	0.17	0.11	0.17	0.13	0.12	0.07	0.01
10	42.90158	142.9805	0.13	0.16	0.10	0.16	0.12	0.11	0.06	0.01
11	42.90148	142.9783	0.15	0.14	0.06	0.12	0.08	0.10	0.06	0.02
12	42.90148	142.9792	0.10	0.12	0.06	0.10	0.07	0.08	0.06	0.02
13	42.90143	142.9802	0.13	0.17	0.11	0.16	0.13	0.12	0.06	0.01
14	42.90142	142.9808	0.14	0.17	0.10	0.16	0.12	0.12	0.06	0.01
15	42.90132	142.9804	0.13	0.18	0.12	0.17	0.13	0.12	0.07	0.01
16	42.90128	142.9796	0.11	0.13	0.06	0.11	0.07	0.09	0.06	0.03
17	42.90126	142.9786	0.11	0.13	0.06	0.11	0.07	0.08	0.06	0.02
18	42.90124	142.9811	0.13	0.17	0.10	0.16	0.12	0.11	0.06	0.01
19	42.9012	142.9806	0.13	0.17	0.11	0.17	0.13	0.12	0.06	0.01
20	42.90112	142.9807	0.13	0.17	0.11	0.16	0.13	0.12	0.06	0.01
21	42.90111	142.9798	0.10	0.12	0.06	0.11	0.07	0.09	0.07	0.03
22	42.90104	142.9814	0.13	0.16	0.10	0.16	0.12	0.11	0.05	0.01
23	42.90103	142.979	0.12	0.13	0.06	0.11	0.08	0.09	0.06	0.02
24	42.90101	142.98	0.12	0.14	0.06	0.11	0.08	0.09	0.06	0.03
25	42.90094	142.981	0.14	0.17	0.11	0.17	0.13	0.12	0.06	0.01
26	42.90087	142.9816	0.13	0.17	0.10	0.16	0.12	0.12	0.05	0.01
27	42.90086	142.9803	0.13	0.14	0.06	0.12	0.08	0.09	0.06	0.02
28	42.90086	142.9798	0.12	0.13	0.05	0.11	0.07	0.09	0.06	0.03
29	42.90081	142.9794	0.09	0.12	0.05	0.11	0.07	0.09	0.06	0.02
30	42.90074	142.98	0.12	0.13	0.05	0.12	0.07	0.09	0.06	0.03
31	42.90067	142.9815	0.14	0.17	0.11	0.17	0.12	0.12	0.04	0.01
32	42.90067	142.982	0.14	0.16	0.09	0.16	0.11	0.11	0.03	0.01
33	42.90064	142.9806	0.13	0.14	0.05	0.12	0.08	0.09	0.06	0.02
34	42.9006	142.9802	0.12	0.14	0.05	0.12	0.07	0.09	0.05	0.03
35	42.9005	142.9809	0.13	0.14	0.05	0.12	0.08	0.09	0.06	0.02
36	42.90045	142.9805	0.12	0.13	0.04	0.12	0.07	0.09	0.05	0.03
37	42.90031	142.9812	0.14	0.14	0.06	0.12	0.08	0.10	0.06	0.02
38	42.90031	142.9807	0.13	0.13	0.05	0.12	0.07	0.09	0.05	0.03
39	42.90017	142.981	0.13	0.13	0.05	0.12	0.07	0.09	0.06	0.02
40	42.90017	142.9814	0.14	0.14	0.06	0.12	0.08	0.09	0.06	0.02

5.2.4 Sampling of Wheat Yield and Corresponding Vegetation Indices

Table 5. 6 Samples of wheat yield

ID	Coordinates		Grain Weight	Accumulative values of vegetation index				
	Latitude	Longitude		VDVI	NGRDI	NGBDI	GRRI	ExG
1	42.901657	142.978642	1.01	0.71	1.00	0.50	10.40	333.17
2	42.901097	142.979570	0.86	0.65	1.16	0.29	10.86	264.30
3	42.900532	142.980497	0.84	0.62	1.04	0.29	10.49	286.08
4	42.900180	142.981070	0.91	0.64	1.11	0.27	10.70	296.75
5	42.900360	142.981302	0.85	0.67	1.10	0.33	10.65	301.90
6	42.900694	142.980759	0.79	0.62	1.12	0.24	10.70	276.56
7	42.900972	142.980286	0.82	0.62	1.19	0.18	11.00	259.11
8	42.901202	142.979924	0.80	0.63	1.16	0.25	10.81	244.95
9	42.901476	142.979472	0.83	0.62	1.19	0.18	10.96	259.36

As we have discussed in Sec.5.1 that high-resolution color images could be used as a suitable tool for distinguishing vegetation from the background; besides, the theory on harvest index indicates that the grain yield of a certain variety has a directly proportional relationship with the above ground biomass. Therefore, in this study we are to validate the correlation between the accumulative vegetation indices based on UAV ortho-mosaic images and the sampled grain yields. 9 samples of grain yield were taken by using a 1 m * 1 m square frame to separate samples of wheat canopies in the winter wheat field of Kitahonami. Grain samples' position was selected after detailed visual inspection on the UAV ortho-mosaic images and field survey on the sampling day in order to representatively choose 3 samples of or nearby lodging area and six samples out of normal areas, of which the most flourished areas and sparse areas were both taken into consideration. Spatial distribution of the grain yield samples was shown in Fig.5. 2 as red dots. The sampling operation was conducted at 24 July 2015, three days ahead of harvesting, by collecting wheat ears within the specified 1-square-meter section. These samples' geo-coordinates were acquired by using Trimble SPS855 GNSS modular receiver in RTK-GPS mode. Grain weight of each sample was calculated and converted to 12.5% moisture after threshing, which was listed in Table 5. 6.

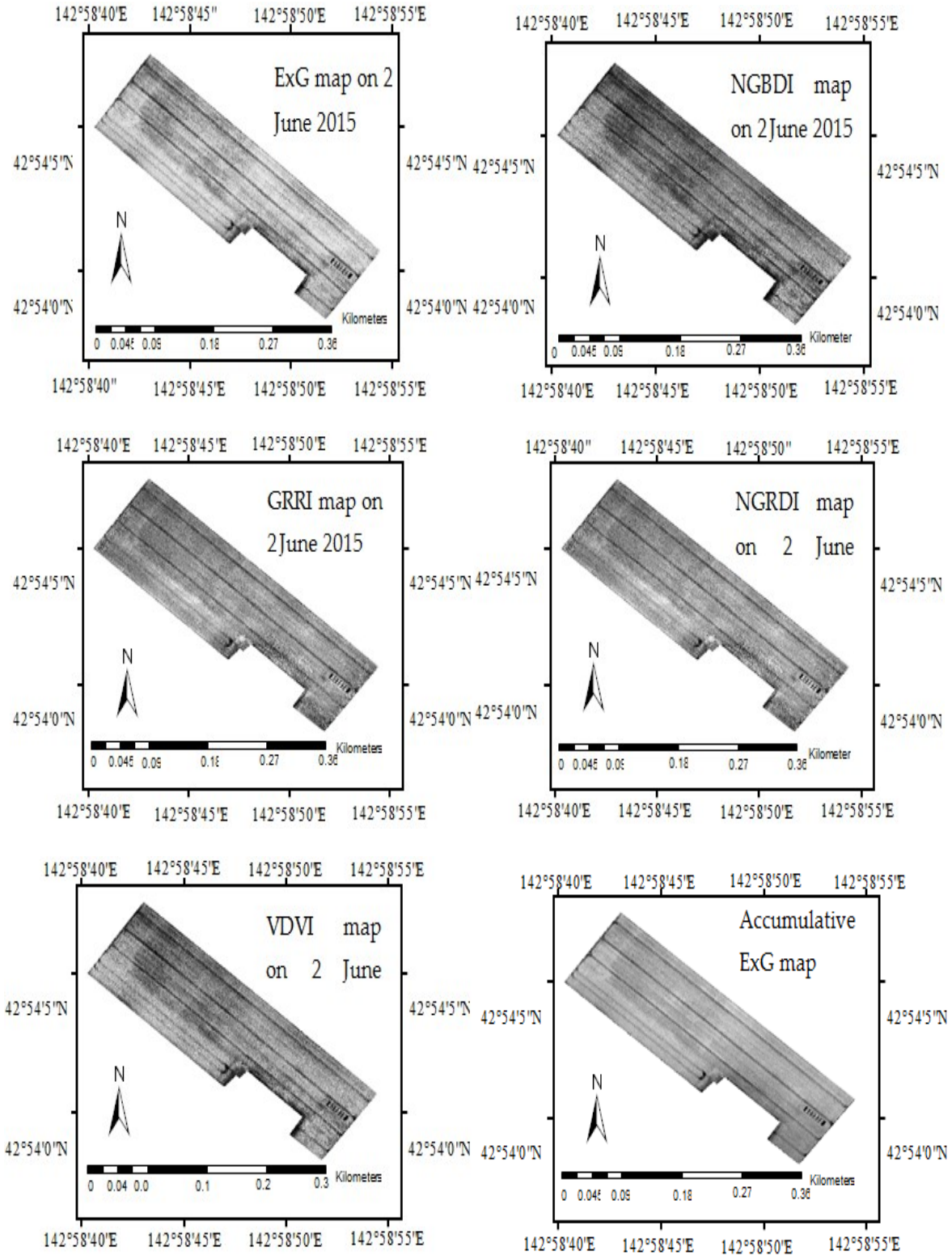

Fig.5. 11 Vegetation index maps based on UAV Ortho-mosaic images

Subsequently, UAV ortho-mosaic images taken on eight dates were all used to generate color vegetation index maps of ExG, NGBDI, GRRI, NGRDI, and VDVI by using ENVI

software. Each pixel value was determined from the radiometrically normalized pixel values and using band math functions according to Eq. (5.3) to Eq. (5.7). Five vegetation index maps of ExG, NGBDI, GRRI, NGRDI, and VDVI based on the UAV ortho-mosaic image taken on 2 June 2015 was shown in Fig.5. 11, respectively; and each vegetation index map based on the UAV ortho-mosaic images taken on other dates was also generated in the same way and omitted here due to limited space. Then the accumulative vegetation index maps for each vegetation index were generated, respectively, by overlapping the corresponding vegetation index maps and adding up pixel values of these scalar maps on different dates. The accumulative ExG map was also shown in Fig.5. 11 as an example. After applying a mean filter of 7 × 7 pixels (which covers about 1-square-meter area) upon each accumulative vegetation index maps of ExG, NGBDI, GRRI, NGRDI, and VDVI, pixel values that share the same geo-spatial coordinates with the nine wheat samples were extracted, also listed in Table 5. 6.

5.3 Results and Discussion

5.3.1 Multi-temporal Monitoring of Wheat Growth Status

From multi-temporal satellite images, shown in Fig.5. 3 in true color mode and Fig.5. 4 in standard false color mode which is combined of NIR band, red band, and green band, we could get general understanding of color change of wheat canopy. We may conclude that in true color mode the greenness of these two wheat fields of different varieties do not differ so much from each other; besides, the greenness of these two wheat fields keeps increasing to the date of June 15 and then begins to decrease since then due to ripening process. Within-field spatial variations of canopy density as well as greenness could not be clearly observed due to sparse spatial resolution of satellite images; however, abrupt brightness only occurred in the field of Kitahonami in the last image taken on July 17 (spotted in red circle), which roughly revealed the lodged wheat canopy's position. On the other hand, within-field spatial variations of canopy color could be clearly observed and the occurrence of lodging was spotted around over-flourished areas (marked in yellow circle) in the field of Kitahonami. For comparison, the other field of Yumechika showed homogeneous characteristics of canopy development, and no lodging happened throughout the field. Conclusion could also be reached that until June 15 both the two fields showed vigorous vegetative growth conditions, and since then no more bright-red areas were found in both two fields in the last image taken

about 10 days prior to harvesting on July 17, which indicated the dying-out process of wheat canopies.

From UAV's ortho-mosaic images straightforward visualization of wheat growth status could be acquired. Within-field variations of wheat canopy density are so obvious that existence of bare soil could even be noticed from the image taken on June 2. In terms of time-domain, canopy greenness of both two wheat varieties reached peak value on June 10 2015, and there is no significant difference of canopy greenness between these two different wheat varieties in early growth stages; however, from June 10 2015 it became very distinctive that field No.2 (marked in red box) showed heavier canopy greenness compared with the other one. In image taken on June 2 2015 of field No.1 (marked in black box) such areas marked in circles had relatively higher level of stalk densities, and compounded with other environmental influences such as rainfall, wind, and etc., it eventually led to the occurrence of lodging at growth stage of grain-filling when the over-luxuriant canopies failed to support heavy wheat ears, marked in image of July 16 and 24 2015. Fig.5. 12 showed a close-shot photograph of the lodging spot in field No.1, taken on July 16 2015. It suggested that UAV's ortho-mosaic image taken from about one week ahead of harvesting could be practically served as navigation references which guide either drivers of combine harvesters, or autonomous harvesting vehicles, to adjust operation speed according to the specific lodging situations for less loss rate of harvesting, as occurrence of lodging in wheat field has been generally considered as the most influencing and direct factor which impairs the working performance of combine harvester.

Fig.5. 12 Close-shot photograph of the lodging spot in test wheat field

Table 5. 7 Time-varying NDVI and VDVI values calculated from satellite images

	Date	Average	Standard deviation
Satellite NDVI	June 1	0.54	0.04
	June 7	0.72	0.04
	June 15	0.57	0.03
	July 17	0.19	0.05
Satellite VDVI	June 1	0.02	0.001
	June 7	0.06	0.01
	June 15	-0.01	0.02
	July 17	0.003	0.02

Table 5. 8 Time-varying VDVI values calculated from UAV's Ortho-mosaic images

	Date	Average	Standard deviation
UAV VDVI	June 2	0.12	0.01
	June 10	0.15	0.02
	June 19	0.08	0.03
	June 25	0.14	0.02
	July 2	0.10	0.02
	July 10	0.10	0.01
	July 16	0.06	0.01
	July 24	0.02	0.01

In order to further analyze time-varying canopy color changes, the average values and standard deviations of NDVI as well as VDVI samples derived out of each satellite image were listed in Table 5. 7; and the average values and standard deviations of the corresponding of VDVI samples based on each UAV ortho-mosaic image were listed Table 5. *8*. The increasing trend of satellite image based NDVI values was very clear at early growth stages, and then NDVI values began to decrease stage by stage to minimum value around 0.19, which was also showed in Fig.5. 13. On the other hand, VDVI values calculated from satellite images suggested the same tendency with the NDVI counterpart that VDVI reached maximum values on June 7 and then began to decrease as wheat changed from vegetative growth into reproductive process. Besides, heavy variation of VDVI values derived from satellite images around wheat ripening stage may be a big issue when used for quantitative inversion with ground variables, showed in Fig.5. 13, as satellite image based VDVI is not as reliable as NDVI when crops are in the process of ripening or yellowing and VDVI values diverge around the threshold value of 0. Data on June 15 and July 17 indicated that most of VDVI values were found to be negative numbers due to the interference of soil pixels

compounding with other reasons such as lodging, as the sparse resolution of satellite images reaches up to about 5 m.

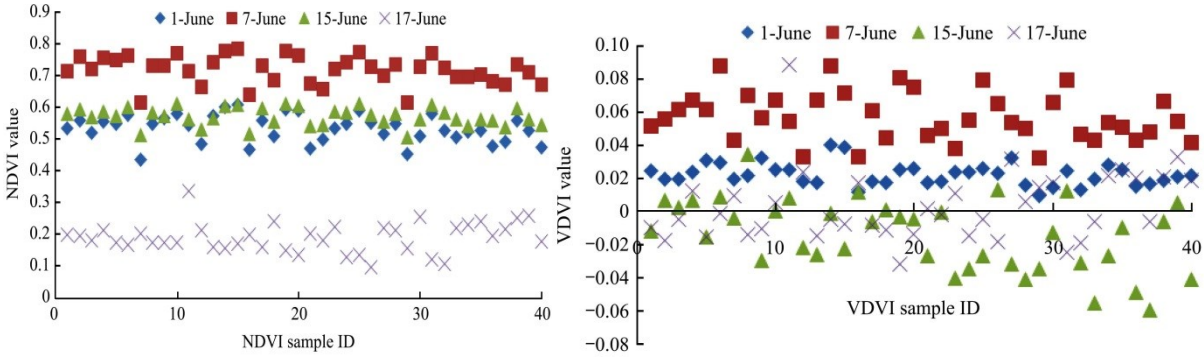

Fig.5. 13 Satellite image based vegetation indices

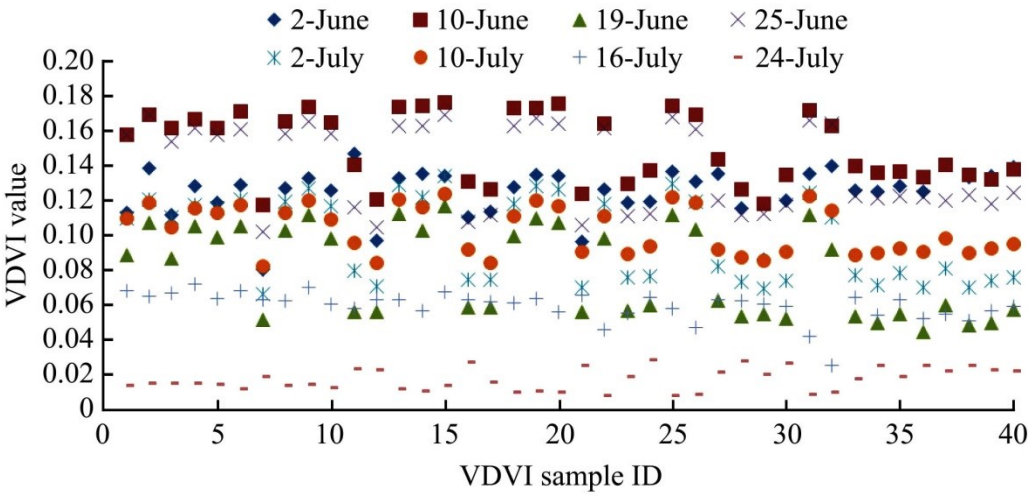

Fig.5. 14 UAV Ortho-mosaic image based VDVI

However, from the VDVI data based on UAV ortho-mosaic images, shown in Fig.5. 14, we may conclude that the time-varying trend of VDVI based on the UAV ortho-mosaic image is very alike with the one we made by observing multi-temporal changes of satellite image based NDVI as well as satellite image based VDVI. Firstly VDVI values increased until June 10 and then began to decrease stage by stage to the minimum value around 0.02. The difference of UAV's ortho-mosaic image based VDVI from satellite image based VDVI is that the VDVI values of the former remote sensing source were found to be positive values even until July 24, 2 day prior to harvesting, which once again confirmed VDVI's capability

to differentiate vegetative areas from non-vegetative areas. The reason could be that decimeter-level ground resolution of UAV's ortho-mosaic images eliminated soil and other background features' interference. Nevertheless, the existence of abnormal value on 19 June also indicated that the individual VDVI values based on a specific color image could be deceptive, as it is not as reliable as the NDVI value due to the lack of NIR band.

Furthermore, correlation analysis of vegetation indices based on satellite images and UAV's ortho-mosaic images was performed for temporal complementation. All of four satellite images and four out of eight UAV's ortho-mosaic images that were taken temporally around the dates of satellite images were used, from which vegetation indices were extracted, respectively, as has been described in Sec. 5.2.3. Regression analysis showed that second-order polynomial models fitted best between UAV's Ortho-mosaic image based VDVI and satellite image based VDVI as well as satellite image based NDVI, when compared with other regression models such as linear, exponential, and power. Coefficient of determination and RMSE were calculated as 0.62 and 0.019 for second-order polynomial regression model between UAV's ortho-mosaic image based VDVI and satellite image based VDVI. On the other hand, coefficient of determination and RMSE were calculated as 0.58 and 0.127 for second-order polynomial regression model between UAV's ortho-mosaic image based VDVI and satellite image based NDVI, respectively. Therefore, we may conclude that it is feasible to temporally complement satellite remote sensing by using UAV's ortho-mosaic images by both visual interpretation and also quantitative analysis to monitor wheat growth status.

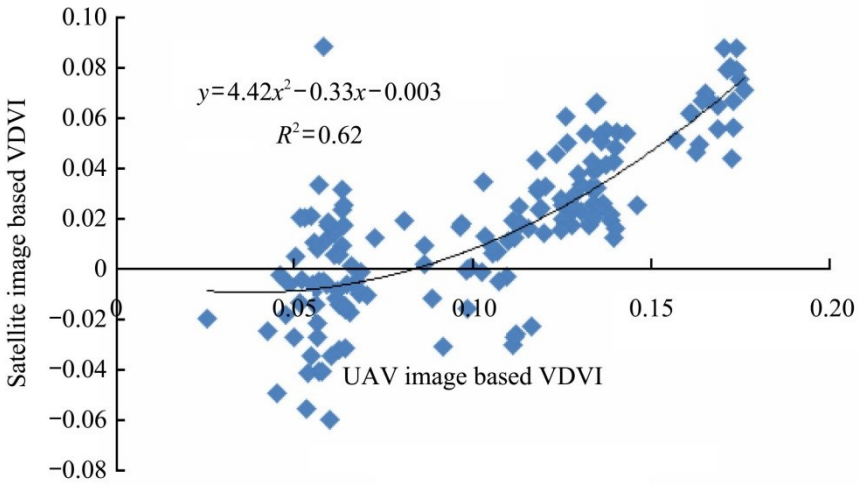

Fig.5. 15 Regression model between UAV images' VDVI and satellite images' VDVI

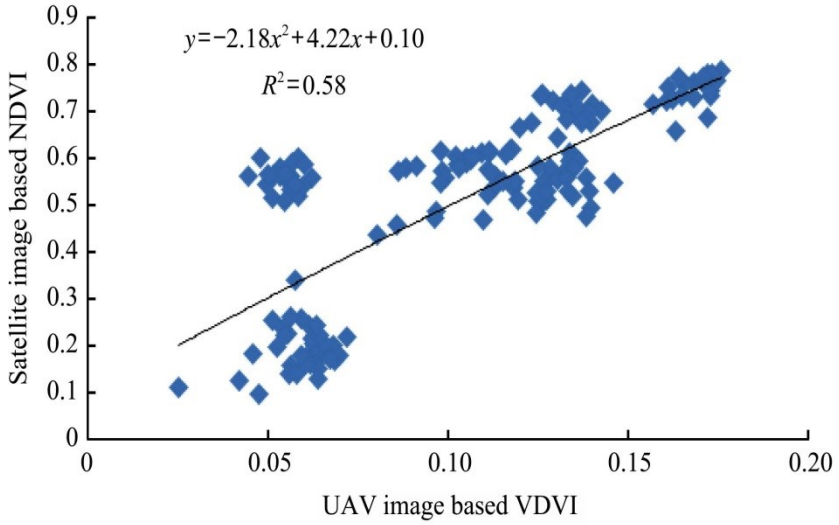

Fig.5. 16 Regression model between UAV images' VDVI and satellite images' NDVI

5.3.2 Mapping within-Field Variations of Wheat Yield

As mentioned in Sec.5.1, it was reported that accumulative vegetation indices values of multi-temporal remote sensing images after flowering stage have good relationship with crop yield. Besides, we have also understood from Sec.5.3.1 that vegetation index values from an individual remote sensing image taken on a specific date could be inaccurate and deceptive due to weather condition and etc. Therefore, in this study we conducted stepwise regression analysis of sampled wheat yield with five different accumulative vegetation indices, which were extracted from eight UAV's ortho-mosaic images that covered a winter wheat field from heading stage to ripening stage, as described in Sec.5.2.4. By using stepwise method, a regression analysis was performed in MATLAB R2013a (The MathWorks, Inc.,Natick, MA, USA) among the response variable of sampled wheat yield and five predictive variables of accumulative vegetation indices of ExG, NGBDI, GRRI, NGRDI, and VDVI, listed in Table 5. 6.

The result of stepwise regression analysis showed that the variable of NGRDI was removed from the stepwise regression model due to insignificant correlation with the responsive variable of wheat yield, whilst the rest variable of VDVI, NGBDI, GRRI, and ExG were included to fit the regression model expressed as Eq. (5.8), with coefficient of determination as 0.94 and RMSE = 0.02. For comparison, the average value of sampled grain yield was calculated as 0.86 kg per square meter. Subsequently, LOOCV was also conducted

by building nine linear regression models that uses eight set variables of sampled wheat yield and values of VDVI, NGBDI, GRRI, and ExG as training data, whilst leaves one set of variables as test data. RMSEP for the LOOCV was calculated as 0.06.

$$Y = -6.19 - 6.78 \times X1 + 3.45 \times X3 + 0.88 \times X4 + 0.003 \times X5 \quad (5.8)$$

where Y, X1, X3, X4, and X5 denotes estimated wheat yield, accumulative VDVI, NGBDI, GRRI, and ExG, respectively.

Based on the regression model expressed as Eq. (5.8), wheat yield was calculated by using VDVI, NGBDI, GRRI, and ExG maps, and finally map of wheat yield was generated accordingly in ENVI software. Wheat yield's within-field spatial variations could be observed from the yield map shown in Fig.5. 17 that non-uniformity of wheat yield of this field is quite obvious and the occurrence of lodging coincide with the high-yield areas. By observing the histogram of the wheat yield map we could also obtain the information that about 25.8% areas in the studied field had grain weight per square meter below 0.5 kg, which still has much room for improvement by implementing variable-rate fertilization, precise land leveling, and etc.; whilst grain weight per square meter of most areas reached between 0.5–1.5 kg, occupying about 50.4% acreages; and the average value of grain weight per square meter was calculated as 0.72 kg, which indicated the estimated average yield of the studied field as 7.2 t/ha. (The yield of Kitahonami planted in Hokkaido is reported from 6.0 to 8.5 t/ha year by year.)

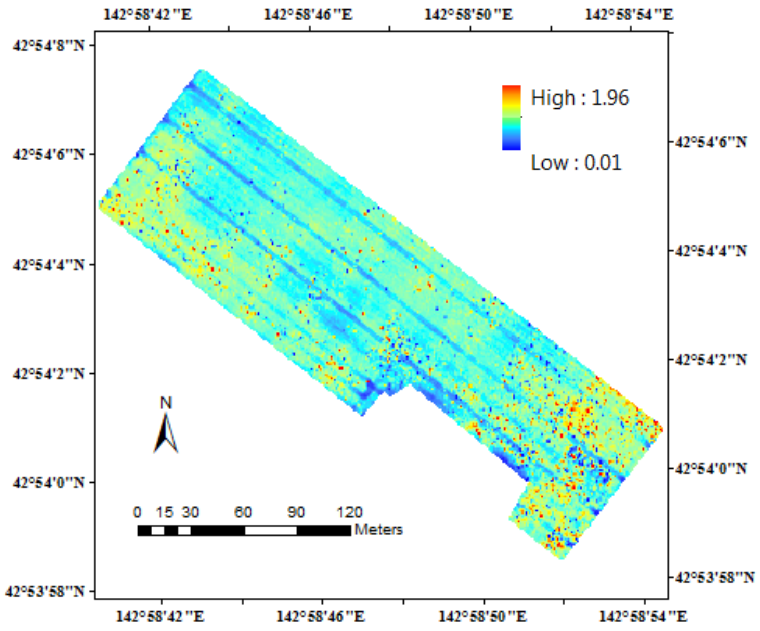

Fig.5. 17 Map of wheat yield (expressed as grain weight per square meter).

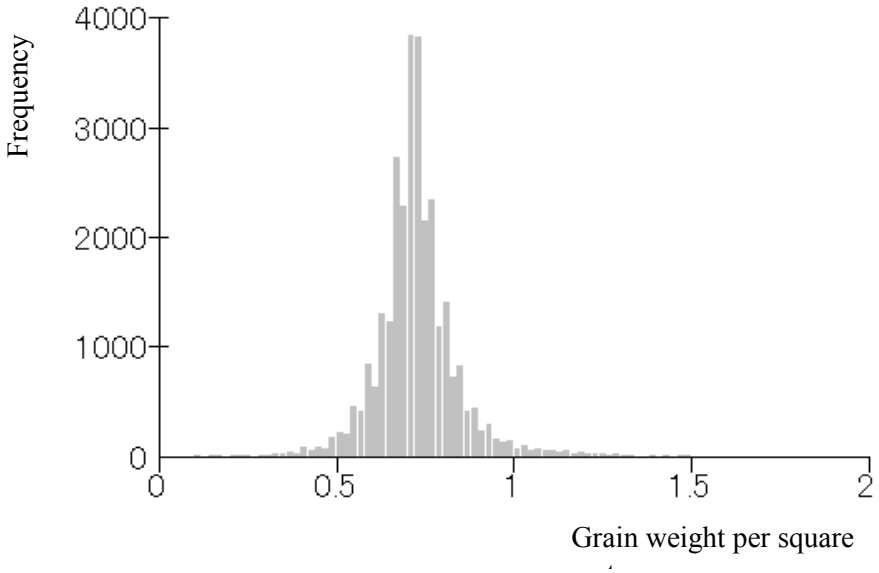

Fig.5. 18 Histogram of wheat yield map

5.3 Conclusion

Based on the multi-temporal satellite remote sensing images and UAV's ortho-mosaic images, we monitored the time-varying canopy color change through image interpretation and spotted the occurrence of wheat lodging from UAV ortho-mosaic images take from about 10 days prior to harvesting. It indicated that the high-resolution UAV ortho-mosaic image could be used to guide drivers or autonomous harvesting vehicles to adjust operation speed for less harvesting loss. Through monitoring changes of both satellite image based NDVI as well as VDVI values and UAV's ortho-mosaic image based VDVI values, conclusion was reached that all of these three vegetation indices have the same and synchronized trend of increasing at first, reaching up to peak values around June 7 or 10 2015 before wheat's reproductive growth begins, and starting to decrease since then. By observing the time-varying values of vegetation indices, we concluded that UAV's ortho-mosaic images with high spatial resolution demonstrated good performance because pixel values are less affected by background interference when compared with satellite images. We may also suggest that it could be feasible of using commercial camera which is mounted upon small UAVs to conduct both qualitative and quantitative study on crop monitoring.

We also analyzed the correlations among satellite remote sensing images based vegetation indices and UAV's ortho-mosaic image based vegetation index, to discuss the

feasibility of utilizing UAV remote sensing images to temporarily complement satellite remote sensing in case that satellite images were not available or cost-efficient over specific areas. The correlation analysis of satellite image based NDVI as well as VDVI with UAV ortho-mosaic image based VDVI showed good consistency at the early stage of wheat growing season. However, at the late stage of wheat growing season VDVI based on satellite images showed unreliable characteristics due to satellite image's sparse spatial resolution; on the other hand, VDVI based on UAV ortho-mosaic images fell rapidly to the values around 0.05 at the late growth stage and also showed very limited capability to differentiate wheat growing status when compared with NDVI, due to the absence of the NIR band information. Therefore, in order to remedy the confine of the direct use of UAV's ortho-mosaic images, image processing techniques such as image segmentation are considered to integrate UAV ortho-mosaic images with satellite images in future work.

Through stepwise regression analysis of the response variable of sampled grain weight per square meter and the predictive variables of accumulative color vegetation indices, we can conclude that only the variable of normalized green-red difference index was removed from the stepwise regression model due to insignificant p-value, whilst the rest variables of visible-band difference vegetation index (the normalized green-blue difference index, green-red ratio index, and excess green vegetation index) were included to fit the regression model, with coefficient of determination and RMSE as 0.94 and 0.02, respectively. The averaged value of sampled grain weight per square meter was calculated as 0.86 kg. The regression model was also validated by using leave-one-out cross validation method, which showed that the root-mean-square error of predication of the regression model was 0.06. Based on the stepwise regression model, a map of estimated grain weight per square meter (yield map) was generated and within-field spatial variations of wheat yield could be understood. The yield map could be seen as the comprehensive presentation of the spatial variations of soil fertility, tiller density, effective water potential, canopy aeration condition, and etc., which could be used as reference for variable-rate fertilization and precise land-leveling in order to further improve the overall yield.

Chapter 6 Summary

Agricultural remote sensing is a vital component of precision agriculture, which collects and manifests the spatial variations of farmland condition and crop growth status for site-specific treatments. Civilian applications of UAVs witnessed rapid development during these two decades from recreational aerial photography to security monitoring, agricultural spraying, remote sensing, and etc., due to advantages such like low cost, high efficiency, good maneuverability, and safety. In this dissertation, we explored the feasibility of introducing a low-altitude UAV as the platform into three agricultural remote sensing projects including: (a). to generate topographic maps of farmland for precision land levelling operation by integrating multiple sensors onboard the UAV platform; (b). to generate wheat stalk density maps during the early growth stage for variable-rate topdressing by segmenting UAV remote sensing images; and (c). to conduct correlation analysis between vegetation indices based on UAV ortho-mosaic images and satellite remote sensing images, as well as to map within-field spatial variations of wheat yield according to multi-temporal UAV remote sensing images.

(a). A one-dimensional LiDAR distance measurement device was installed upon the UAV platform, which is set to measure the distance between the ground surface to the UAV-LiDAR system at the frequency of 10 Hz. The LiDAR distance measurements were amended according to the UAV-LiDAR system's attitude information, which were calculated from the multiple MEMS IMU sensors incorporated inside the UAV's flight controller. A PPK-GPS module with small size and light weight features was also attached to the UAV-LiDAR system, so that each LiDAR distance measurement could be geo-referenced and accordingly the ground elevation of each surveying point could be calculated to acquire 3D coordinates (latitude, longitude, and altitude). The static accuracies of LiDAR distance measurements and the PPK-GPS positioning coordinates were validated by extracting 6000 sets of measuring data, which indicated that the accuracy of LiDAR distance measurements is as high as 1cm, whilst the horizontal and vertical accuracy of PPK-GPS is 1cm and about 2 cm, respectively. The overall accuracy of the UAV-LiDAR system based topographic surveying approach was also validated by using a RTK-GPS module to take 35 samples that uniformly spread throughout the field under study and overlapped with the UAV-LiDAR system's trajectory.

The RMSE between the ground elevation data of the UAV-LiDAR system and the validating RTK-GPS altitude was calculated as 3.5 cm, which demonstrated high-accuracy and feasibility of conducting topographic survey by using our proposed UAV-LiDAR system. Visual inspection of the UAV-LiDAR system based topographic survey was also implemented by manually building bumps and hollows inside the experimental field, and the UAV-LiDAR system was found to be capable of clearly recognizing and demonstrating these artificial features. Subsequently, different interpolation methods that were used to generate farmland topographic maps based on the UAV-LiDAR system's topographic surveying data were investigated to select the most accurate interpolation model. As the result, TIN interpolation model was found to be the most accurate one, and RMSE between the sampled reference altitude values of RTK-GPS data and the corresponding ground elevation values of the resulting topographic map based on TIN interpolation model was calculated as 13.7 cm. Finally aerial photogrammetric DSM was integrated with the UAV-LiDAR system's topographic surveying data for an improved topographic map, as the former topographic data has the advantage of large coverage but is also known for its unreliable accuracy, whist the accuracy of the UAV-LiDAR system based topographic data is proved to be very high but the spatial coverage is very poor. The RSME between the validating RTK-GPS altitude data and the corresponding ground elevation values of the improved topographic map based on TIN interpolation model was calculated as 5.9 cm, which showed great accuracy and practicability of our proposed topographic mapping method.

(b). A multispectral camera (Green-Ren-NIR) was installed upon the UAV platform for acquiring high-resolution images of wheat field during early growth stages. After ortho-mosaicking and geo-referencing, the multispectral UAV images were transformed into a NDVI map. Wheat stalk densities of the field under study were manually counted as ground truth, of which the geographical coordinates were measured by using a RTK-GPS module. The NDVI map was used to calculate FGV value, which is an indicator of the vegetation coverage. Besides, the NDVI map was further binarized into vegetation class and background class based on the conventional thresholding method as well as the SVM classifier method, respectively; and VCC was calculated out of the classification result. Subsequently, different regression models (linear, second-order polynomial, exponential, and power regression) were built between the ground truth and the corresponding FGV and VCC, respectively. As the result, we concluded that the regression models based on FGV have good accuracies with the coefficient of determination around 0.89, whilst the regression models based on VCC have

better accuracies with the coefficient of determination around 0.94. Furthermore, we selected the power regression model, which has the highest coefficient of determination of 0.95 and root-mean-square error of 24, in consideration that the average value of the sampled stalk densities was calculated as 593 stalks per square meter. The validating experiment on the other wheat field with the same seeding rate and similar field management treatment also confirmed that the power regression model is the most accurate and suitable model between the sampled stalk density values and the SVM classifier based VCC values. Finally, according to the power regression model 125 stalk density values were calculated by extracting the corresponding VCC values from the resulting vegetation classification map based on SVM classification method, and stalk density maps were generated by using different interpolation methods. In thus, we would like to conclude that the UAV-camera system could be used to obtain quantitative information for variable-rate topdressing in an accurate and efficient manner.

(c). Agricultural application of UAV remote sensing by using commercial RGB cameras decreases high cost of remote sensing sharply and provides instantly researchers and farmers with actual and intuitive visualization of crop growth status, since color images accentuate particular vegetation greenness and have been suggested to be less sensitive to variations of illumination conditions. We installed a SONY ILCE-6000 commercial digital camera upon the UAV platform and acquired 8 sets of RGB images over a wheat farmland, which were further processed by generating and geo-referencing eight ortho-mosaic images. Based on the multi-temporal (from early June to late July 2015) satellite remote sensing images on four different dates and UAV's ortho-mosaic images on eight different dates, we monitored the time-varying canopy color change through image interpretation and spotted the occurrence of wheat lodging from UAV ortho-mosaic images taken from about 10 days prior to harvesting. It indicated that the high-resolution UAV ortho-mosaic image could be used to guide drivers or autonomous harvesting vehicles to adjust operation speed for less harvesting loss according to the specific lodging situations. We also analyzed the correlations among satellite remote sensing images based vegetation indices and UAV's ortho-mosaic image based vegetation index, and the correlation analysis of satellite image based NDVI as well as VDVI with UAV image based VDVI showed good consistency at the early stage of wheat growing season. Through stepwise regression analysis of the response variable of sampled grain weight per square meter and the predictive variables of accumulative color vegetation indices, we can conclude that only the variable of normalized green-red difference index was

removed from the stepwise regression model due to insignificant p-value, whilst the rest variables of visible-band difference vegetation index, the normalized green-blue difference index, green-red ratio index, and excess green vegetation index were included to fit the regression model, with coefficient of determination and RMSE as 0.94 and 0.02, respectively. The averaged value of sampled grain weight per square meter was calculated as 0.86 kg. The regression model was also validated by using leave-one-out cross validation method, which showed that the RMSE of predication of the regression model was 0.06. Based on the stepwise regression model, a map of estimated grain weight per square meter (yield map) was generated and within-field spatial variations of wheat yield could be understood. The yield map could be seen as the comprehensive presentation of the spatial variations of soil fertility, tiller density, effective water potential, canopy aeration condition, and etc., which could be used as reference for variable-rate fertilization and precise land-leveling in order to further improve the overall yield.

In short, the UAV platform based agricultural remote sensing showed high accuracy and efficiency in terms of the acquisition of field information, which is paramount for filling yield gaps through site-specific farming techniques.

References

[1] United Nations News Centre – UN declares famine in another three areas of Somalia. https://www.un.org/apps/news/story.asp?NewsID=39225&Cr=Somalia&Cr1=#.Wc2uyN9Nxyx. Retrieved 2017-09-20.

[2] Hershey D. Misconceptions about Helmont's willow experiment. Plant Science Bulletin. 2003; 49(3):78-84.

[3] Schell J. Stephen Hales and the cohesion theory.. Trends Plant Sci. 1999; 4(6):209.

[4] Brock, William H. Justus von Liebig: the chemical gatekeeper (1st ed.). 1997; Cambridge, U.K.: Cambridge University Press. ISBN 9780521562249.

[5] McKeown, Thomas. The Modern Rise of Population. 1976; London, UK: Edward Arnold. ISBN 9780713159868.

[6] Smil, Vaclav. Enriching the Earth: Fritz Haber, Carl Bosch, and the Transformation of World Food Production. 2004; Cambridge, MA: MIT Press. ISBN 9780262693134.

[7] Hope from hybrid rice. http://www.chinadaily.com.cn/opinion/2011-09/21/content_13745849.htm. Retrieved 2017-09-30.

[8] Population Division World Population Prospects 2017. https://esa.un.org/unpd/wpp/. Retrieved 2017-09-30.

[9] Pimentel D, McLaughlin L, Zepp A, Lakitan B, Kraus T, Kleinman P, Vancini F, Roach WJ, Graap E, Keeton WS, Selig G. Environmental and economic effects of reducing pesticide use. BioScience. 1991 Jun 1;41(6):402-9.

[10] Digital agriculture: helping to feed a growing world. http://performance.ey.com/wp-content/uploads/downloads/2017/02/EY-Performance-digital-agriculture.pdf. Retrieved 2017-09-30.

[11] Shibusawa, S., Anom, W.S., Sato, H., Sasao, A. On-line real-time soil spectrophotometer. Proceedings of Fifth International Conference on Precision Agriculture (CD), July 16 - 19, 2000. Bloomington, MN, USA.

[12] McBratney A, Whelan B, Ancev T, Bouma J. Future directions of precision agriculture. Precision agriculture. 2005 Feb 1;6(1):7-23.

[13] Doerge T. Defining management zones for precision farming. Crop Insights. 1999;8(21):1-5.

[14] TECHNOLOGY ON THE FARM. https://www.arvigbusiness.com/technology-on-the-farm/. Retrieved 2017-10-01.

[15] Stafford JV. Implementing precision agriculture in the 21st century. Journal of Agricultural Engineering Research. 2000 Jul 1;76(3):267-75..

[16] Whelan BM, McBratney AB, Boydell BC. The impact of precision agriculture. proceedings of the ABARE outlook conference. The Future of Cropping in NW NSW, Moree, UK. 1997 Jul:5.

[17] John E. Sawyer. Making every fertilizer dollar pay. Presented at the 11th annual Integrated Crop Nutrient Management Conference, p. 63-78. Dec. 1-2, 1999. Iowa State University, Ames, IA.

[18] Wagner LE, Schrock MD. Yield determination using a pivoted auger flow sensor. Transactions of the ASAE. 1989;32(2):409-0413..

[19] Yule IJ, Kohnen G, Nowak M. A tractor performance monitor with DGPS capability. Computers and Electronics in Agriculture. 1999 Aug 31;23(2):155-74.

[20] Tian L, Reid JF, Hummel JW. Development of a precision sprayer for site-specific weed management. Transactions of the ASAE. 1999;42(4):893.

[21] Hummel JW, Sudduth KA, Hollinger SE. Soil moisture and organic matter prediction of surface and subsurface soils using an NIR soil sensor. Computers and electronics in agriculture. 2001 Aug 31;32(2):149-65.

[22] Noguchi N, Reid JF, Zhang Q, Will JD, Ishii K. Development of robot tractor based on RTK-GPS and gyroscope. In2001 ASAE Annual Meeting 1998 (p. 1). American Society of Agricultural and Biological Engineers.

[23] Misra P, Enge P. Global Positioning System: signals, measurements and performance second edition. Massachusetts: Ganga-Jamuna Press. 2006.

[24] Chang, K. T. Introduction to Geographical Information Systems. New York: McGraw Hill. 2008.

[25] Panigrahi N. Computing in geographic information systems. CRC Press; 2014 Jul 10.

[26] Lillesand T, Kiefer RW, Chipman J. Remote sensing and image interpretation. John Wiley & Sons; 2014 Dec 31.

[27] Mulla DJ. Twenty five years of remote sensing in precision agriculture: Key advances and remaining knowledge gaps. Biosystems engineering. 2013 Apr 30;114(4):358-71.

[28] Colwell R. Determining the prevalence of certain cereal crop diseases by means of aerial photography. California Agriculture. 1956 Nov 1;26(5):223-86.

[29] Eisenbeiss H. A mini unmanned aerial vehicle (UAV): system overview and image acquisition. International Archives of Photogrammetry. Remote Sensing and Spatial Information Sciences. 2004 Nov 18;36(5/W1):1-7.

[30] K J Stout; L Blunt. Three Dimensional Surface Topography, 2nd ed.; Penton Press: London, England, 2000; pp. 3-7.

[31] Geographical Information System. Available online: http://www.michigan.gov/cgi/0,1607,7-158-14767-318 93--F,00.html (accessed on 8 September 2017).

[32] Levidow L, Zaccaria D, Maia R, Vivas E, Todorovic M, Scardigno A. Improving water-efficient irrigation: Prospects and difficulties of innovative practices. Agricultural Water Management. 2014 Dec 31;146:84-94..

[33] Hu Lian, Luo Xiwen, et al. Development of 1PJ-4. 0 Laser Leveler Installed on a Wheeled Tractor for Paddy Field. Transactions of the Chinese Society for Agricultural Machinery, 2014, 45, 146-151. (in Chinese)

[34] Rickman, J.F., 2002. Manual for laser land levelling, Rice-Wheat Consortium Technical Bulletin Series 5. New Delhi-110 012, India: Rice-Wheat Consortium for the Indo-Gangetic Plains. pp. 24.

[35] Hamid Raeisi-Vanani, Mohammad Shayannejad, et al. A Simple Method for Land Grading Computations and its Comparison with Genetic Algorithm (GA) Method. International Journal of Research Studies in Agricultural Sciences, 2017, 3, 8, pp 26-38.

[36] Agricultural Land Levelling. Available online: http://www.optisurface.com/agricultural-land-levelling/.

[37] Jat ML, Chandna P, Gupta R, Sharma SK, Gill MA. Laser land leveling: a precursor technology for resource conservation. Rice-Wheat consortium technical bulletin series. 2006;7:48.

[38] Yongjian L, Zuoxi Z. Design of Attitude Measurement System for Flat Shovel of Laser-controlled Land Leveler for Paddy Field [J]. Journal of Agricultural Mechanization Research. 2012;2:69-75..

[39] Zimmerman, Kurt R., et al. System and method for land-levelling. U.S. Patent No 6,880,643, 2005.

[40] Johnson KM, Ouimet WB. Rediscovering the lost archaeological landscape of southern New England using airborne light detection and ranging (LiDAR). Journal of Archaeological Science. 2014 Mar 31;43:9-20.

[41] Bosse M, Zlot R, Flick P. Zebedee: Design of a spring-mounted 3-d range sensor with application to mobile mapping. IEEE Transactions on Robotics. 2012 Oct;28(5):1104-19.

[42] Remondino F. Heritage recording and 3D modeling with photogrammetry and 3D scanning. Remote Sensing. 2011 May 30;3(6):1104-38..

[43] Moskal LM, Zheng G. Retrieving forest inventory variables with terrestrial laser scanning (TLS) in urban heterogeneous forest. Remote Sensing. 2011 Dec 23;4(1):1-20.

[44] Zhang S, Wang C, Yang Z, Chen Y, Li J. Automatic railway power line extraction using mobile laser scanning data. Proceedings of the International Archives of the Photogrammetry, Remote Sensing and Spatial Information Sciences, Prague, Czech Republic. 2016 Jul 12;5:615-9.

[45] Guo Zong-he, Zheng Jin-feng, Cui Yun-chuan. Surveying and Setting-out Based on Two-point Reference Line with Total Station. Bulletin of Surveying and Mapping, 2004, 8: 022.

[46] Resop JP, Hession WC. Terrestrial laser scanning for monitoring streambank retreat: Comparison with traditional surveying techniques. Journal of Hydraulic Engineering. 2010 Mar 27;136(10):794-8.

[47] Corsini A, Castagnetti C, Bertacchini E, Rivola R, Ronchetti F, Capra A. Integrating airborne and multi- temporal long- range terrestrial laser scanning with total station measurements for mapping and monitoring a compound slow moving rock slide. Earth surface processes and landforms. 2013 Sep 15;38(11):1330-8.

[48] Rodríguez-Gonzálvez P, Jiménez Fernández-Palacios B, Muñoz-Nieto ÁL, Arias-Sanchez P, Gonzalez-Aguilera D. Mobile LiDAR System: New Possibilities for the Documentation and Dissemination of Large Cultural Heritage Sites. Remote Sensing. 2017 Feb 23;9(3):189.

[49] Hirano A, Welch R, Lang H. Mapping from ASTER stereo image data: DEM validation and accuracy assessment. ISPRS Journal of Photogrammetry and Remote Sensing. 2003 Apr 30;57(5):356-70.

[50] Harwin S, Lucieer A. Assessing the accuracy of georeferenced point clouds produced via multi-view stereopsis from unmanned aerial vehicle (UAV) imagery. Remote Sensing. 2012 May 30;4(6):1573-99.

[51] Lovitt J, Rahman MM, McDermid GJ. Assessing the Value of UAV Photogrammetry for Characterizing Terrain in Complex Peatlands. Remote Sensing. 2017 Jul 12;9(7):715.

[52] Goyer GG, Watson R. The laser and its application to meteorology. Bulletin of the American Meteorological Society. 1963 Sep;44(9):564-75.

[53] Artale V, Milazzo CL, Ricciardello A. Mathematical modeling of hexacopter. Appl. Math. Sci. 2013;7(97):4805-11..

[54] Huang YP. Triangular irregular network generation and topographical modeling. Computers in industry. 1989 Jul 1;12(3):203-13.

[55] Peucker TK, Fowler RJ, Little JJ, Mark DM. The triangulated irregular network. InAmer. Soc. Photogrammetry Proc. Digital Terrain Models Symposium 1978 May 9 (Vol. 516, p. 532).

[56] Tsai VJ. Delaunay triangulations in TIN creation: an overview and a linear-time algorithm. International Journal of Geographical Information Science. 1993 Nov 1;7(6):501-24.

[57] Philip, G. M., and D. F. Watson. A Precise Method for Determining Contoured Surfaces. Australian Petroleum Exploration Association Journal 22: 205–212. 1982.

[58] Watson, D. F., and G. M. Philip. A Refinement of Inverse Distance Weighted Interpolation. Geoprocessing 2:315–327. 1985.

[59] Franke R. Smooth interpolation of scattered data by local thin plate splines. Computers & Mathematics with Applications. 1982 Jan 1;8(4):273-81.

[60] Mitáš L, Mitášová H. General variational approach to the interpolation problem. Computers & Mathematics with Applications. 1988 Jan 1;16(12):983-92.

[61] Aurenhammer F. Voronoi diagrams—a survey of a fundamental geometric data structure. ACM Computing Surveys (CSUR). 1991 Sep 1;23(3):345-405.

[62] Sibson, R. A Brief Description of Natural Neighbor Interpolation, chapter 2 in Interpolating Multivariate Data. New York: John Wiley & Sons, 1981. 21–36.

[63] LI, Zhilin; ZHU, Christopher; GOLD, Chris. Digital terrain modeling: principles and methodology. CRC press, 2004.

[64] Global wheat production from 1990/1991 to 2016/2017 (in million metric tons). https://www.statista.com/statistics/267268/production-of-wheat-worldwide-since-1990/. Retrieved October 20, 2016.

[65] Shewry PR, Hey SJ. The contribution of wheat to human diet and health. Food and Energy Security. 2015, 4 (3): 178–202.

[66] CURTIS, Byrd C., et al. Bread wheat: improvement and production. Food and Agriculture Organization of the United Nations (FAO), 2002.

[67] Zadoks J C., Chang T T., Konzak C F. A decimal code for the growth stages of cereals. Weed Res. 1974, 14, 415-21.

[68] Nick Poole. Cereal growth stages. Grains research & development corporation, New Zealand, 2005; pp. 4-40.

[69] Small Grain Production Guide Revised March 2013, http://www.smallgrains.ncsu.edu/production-guide.html (accessed 2015.05.01).

[70] Clement Atzberger. Advances in Remote Sensing of Agriculture: Context Description, Existing Operational Monitoring Systems and Major Information Needs. Remote Sens. 2013, 5, 949-981.

[71] Irene Aicardi, Francesco Nex, Markus Gerke and Andrea Maria Lingua. An Image-Based Approach for the Co-Registration of Multi-Temporal UAV Image Datasets. Remote Sens. 2016, 8, 779.

[72] Colewell, R.N. Determining the prevalence of certain cereal crop diseases by means of aerial photography. Hilgardia 1956, 26, 223-286.

[73] Huang Y, Thomson S J, Brand H J, Reddy K N. Development of low-altitude remote sensing systems for crop production management. Int J Agric & Biol Eng. 2016, 9(4): 1-11.

[74] Lu B, He Y. Species classification using Unmanned Aerial Vehicle (UAV)-acquired high spatial resolution imagery in a heterogeneous grassland. ISPRS Journal of Photogrammetry and Remote Sensing. 2017 Jun 30;128:73-85.

[75] Wang Xiaoqin, Wang Miaomiao, Wang Shaoqiang, Wu yundong. Extraction of vegetation information from visible unmanned aerial vehicle images. Transactions of Chinese Society of Agriculture Engineering 2015, 31(5):152-159.

[76] Rasmussen, J.; Ntakos, G.; Nielsen, J.; Svensgaard, J.; Poulsen, R. N.; Christensen, S. Are vegetation indices derived from consumer-grade cameras mounted on UAVs sufficiently reliable for assessing experimental plots? European Journal of Agronomy 2016, 74, 75–92.

[77] City of Sapporo. http://www.city.sapporo.jp/city/aramashi/ (Retrieved October 25, 2016).

[78] LebourgeoisV., BéguéA., LabbéS., MallavanB., PrévotL., Roux B., 2008. Can commercial digital cameras be used as multispectral sensors? A crop monitoring test. Sensors, 7300-7322.

[79] Bobbe, T.; McKean, J.; Zigadlo, J.P. An evaluation of natural color and color infrared digital cameras as a remote sensing tool for natural resource management. Airborne Reconnaissance XIX; Bellingham, WA, USA, 1995; Volume 2555, pp. 151-157.

[80] Rouse, J. W., R. H. Haas, J. A. Schell, and D. W. Deering, 1973. Monitoring vegetation systems in the Great Plains with ERTS, Third ERTS Symposium, NASA SP-351 I, 309-317.

[81] Kriegler, F.J., Malila, W.A., Nalepka, R.F., and Richardson, W. (1969) 'Preprocessing transformations and their effects on multispectral recognition.' Proceedings of the Sixth International Symposium on Remote Sensing of Environment, p. 97-131.

[82] Crippen, R.E. (1990) 'Calculating the vegetation index faster,' Remote Sensing of Environment, 34, 71-73.

[83] Li X, Zhang J. Derivation of the green vegetation fraction of the whole China from 2000 to 2010 from MODIS data. Earth Interactions. 2016 Mar;20(8):1-6.

[84] Song W, Mu X, Ruan G, Gao Z, Li L, Yan G. Estimating fractional vegetation cover and the vegetation index of bare soil and highly dense vegetation with a physically based method. International Journal of Applied Earth Observation and Geoinformation. 2017 Jun 30;58:168-76.

[85] Purcell LC. Soybean canopy coverage and light interception measurements using digital imagery. Crop Science. 2000 May 1;40(3):834-7.

[86] Korhonen, L., Korpela, I., Heiskanen, J. and Maltamo, M., 2011. Airborne discrete-return LIDAR data in the estimation of vertical canopy cover, angular canopy closure and leaf area index. Remote Sensing of Environment, 115(4), pp.1065-1080.

[87] Iosif VOROVENCII, Mihaela Denisa MUNTEAN. Evaluation of Supervised Classification Algorithms for Landsat 5 TM Images, RevCAD. 2013, 14, 197-206.

[88] KEARNS, Michael; RON, Dana. Algorithmic stability and sanity-check bounds for leave-one-out cross-validation. Neural computation, 1999, 11.6: 1427-1453.

[89] FENG Qisheng, GAO Xinhua. Application of Excel in the Experiment Teaching of Leave-One-Out Cross Validation. Experiment Science and Technology, 2015, 13.2: 49-51.

[90] Wu, Q.; Wang, C.; Fang, J.J.; Ji, J.W. Field monitoring of wheat seedling stage with hyperspectral imaging. Int. J. Agric. Biol. Eng. 2016, 9, 143–148.

[91] Zhang, F.; Wu, B.; Luo, Z. Winter wheat yield predicting for America using remote sensing data. J. Remote Sens. 2004, 8, 611–617.

[92] Roberto, B.; Paolo, R. On the use of NDVI profiles as a tool for agricultural statistics: The case study of wheat yield estimate and forecast in Emilia Romagna. Remote Sens. Environ. 1993, 45, 311–326, doi:10.1016/0034-4257(93)90113-C.

[93] Du X, Wu B, Li Q, Meng J, Jia K. A method to estimated winter wheat yield with the MERIS data. InProgress in Electromagnetics Research Symposium (PIERS) Proceedings. Beijing, China. March 23Á27 2009 Mar 23.

[94] Okuno R. Wheat Harvest Support System to Optimize Harvest Timing with Satellite Remote-sensing. JOURNAL of the JAPANESE SOCIETY of AGRICULTURAL MACHINERY. 2005 Sep 1;67(5):17-9.

[95] Han-ya I, Ishii K, Noguchi N. Estimation of moisture content of wheat ear using satellite and helicopter imagery. Pap. Environ. Inf. Sci. 2009;23:155-60.

[96] Reyns P, Missotten B, Ramon H, De Baerdemaeker J. A review of combine sensors for precision farming. Precision Agriculture. 2002 Jun 1;3(2):169-82.

[97] Space engineering development Co., Ltd., WorldView-2. http://www.sed.co.jp/sug/contents/satellite/satellite_worldview2.html. Accessed on 2016-12-05.

[98] Satellite image corporation, RapidEye Satellite Sensor. http://www.satimagingcorp.com/satellite-sensors/other-satellite-sensors/rapideye/. Accessed on 2016-12-05.

[99] Ministry of Agriculture, Forestry and Fisheries, Statistics on farmland. http://www.maff.go.jp/j/tokei/sihyo/data/10.html. Accessed on 2017-11-25.

[100] Du M M, Noguchi N. Monitoring of wheat growth status and mapping of wheat yield's within-field spatial variations using color images acquired from UAV-camera system. Remote Sensing, 2017; 9(3): 289.

[101] Campbell J B, Wynne R H. Introduction to remote sensing. 5th edition. The Guilford Press, New York, USA, 2011; pp.72–102.

[102] Wang X Q, Wang M M, Wang S Q, Wu Y D. Extraction of vegetation information from visible unmanned aerial vehicle images. Transactions of the CSAE, 2015; 31(5): 152–159.

[103] Hunt E R, Hively J W D, Fujikawa S J, Linden D S, Daughtry C S T, McCarty G W. Acquisition of NIR-green-blue digital photographs from unmanned aircraft for crop monitoring. Remote Sens, 2010; 2: 290–305.

[104] Torres-Sánchez J, López-Granados F, De Castro A I, Peña-Barragán J M. Configuration and specifications of an unmanned aerial vehicle (UAV) for early site specific weed management. PLoS One, 2013; 8(3): e58210.

[105] Woebbecke D M, Meyer G E, Von Bargen K, Mortensen D A. Color indices for weed identification under various soil, residue and lighting conditions. Transactions of the ASAE 1995; 38(1): 259–269.

[106] Cui, R.X.; Liu, Y.D.; Fu, J.D. Estimation of winter wheat biomass using visible spectral and BP based artificial neural networks. Spectrosc. Spectr. Anal. 2015, 35, 2596–2601.

[107] http://www.data.jma.go.jp/obd/stats/etrn/view/annually_a.php?prec_no=20&block_no=0115&year=2015&month=&day=&view=p1. Accessed on 2017-05-20.

[108] MAFF. http://www.maff.go.jp/. Accessed on 2016-11-10.

[109] Chander G, Haque M O, Sampath A, Brunn A, Trosset G, Hoffmann D, et al. Radiometric and geometric assessment of data from the RapidEye constellation of satellites, International Journal of Remote Sensing, 2013; 34(16): 5905–5925.

[110] Vermote, E. F., Tanre, D., Deuze, J. L., Herman, M., and Morcrette, J.-J, 1997. Second Simulation of the Satellite Signal in the Solar Spectrum, 6S: an overview, IEEE T. Geosci. Remote, 35, 675–686.

[111] Berk, A., Bernstein, L., and Robertson, D, 1989. MODTRAN: a moderate resolution model for LOWTRAN7, Tech. Rep. GL-TR-89-0122, Air Force Geophysics Lab, Hanscom AFB, Massachusetts, USA.

[112] de Carvalho OA, Guimarães RF, Silva NC, Gillespie AR, Gomes RA, Silva CR, de Carvalho AP. Radiometric normalization of temporal images combining automatic detection of pseudo-invariant features from the distance and similarity spectral measures, density scatterplot analysis, and robust regression. Remote Sensing. 2013 May 30;5(6):2763-94..

List of Publications

Journal Paper

1. Du M, Noguchi N, Okamoto H, Kobayashi N. Topographic Mapping of Farmland by Integration of Multiple Sensors on Board Low-Altitude Unmanned Aerial System. World Academy of Science, Engineering and Technology, International Journal of Computer and Systems Engineering. 2017 Nov 13;4(11).
2. Du M, Noguchi N. Monitoring of Wheat Growth Status and Mapping of Wheat Yield's within-Field Spatial Variations Using Color Images Acquired from UAV-camera System. Remote Sensing. 2017 Mar 21;9(3):289.
3. Du M, Noguchi N, Atsushi I, Yukinori S. Multi-temporal monitoring of wheat growth by using images from satellite and unmanned aerial vehicle. International Journal of Agricultural and Biological Engineering. 2017 Sep 30;10(5):1-3.

Proceeding of Conference

1. Du M, Noguchi N. Multi-temporal Monitoring of Wheat Growth through Correlation Analysis of Satellite Images, Unmanned Aerial Vehicle Images with Ground Variable. IFAC-PapersOnLine. 2016 Dec 31;49(16):5-9.